Department of Precision and Microsystems Engineering

# Tuning dynamics and dissipation dilution in 2D material resonators by MEMS-induced tension

**M.P.F. (Michiel) Wopereis**


| | | |
|---|---|---|
| Report no | : | 2024.004 |
| Coach | : | Dr. G.J. (Gerard) Verbiest & Dr. F. (Farbod) Alijani |
| Professor | : | Prof. dr. P.G. (Peter) Steeneken |
| Specialisation | : | DMN & MSD |
| Type of report | : | MSc. Thesis |
| Date | : | 24 December 2023 |


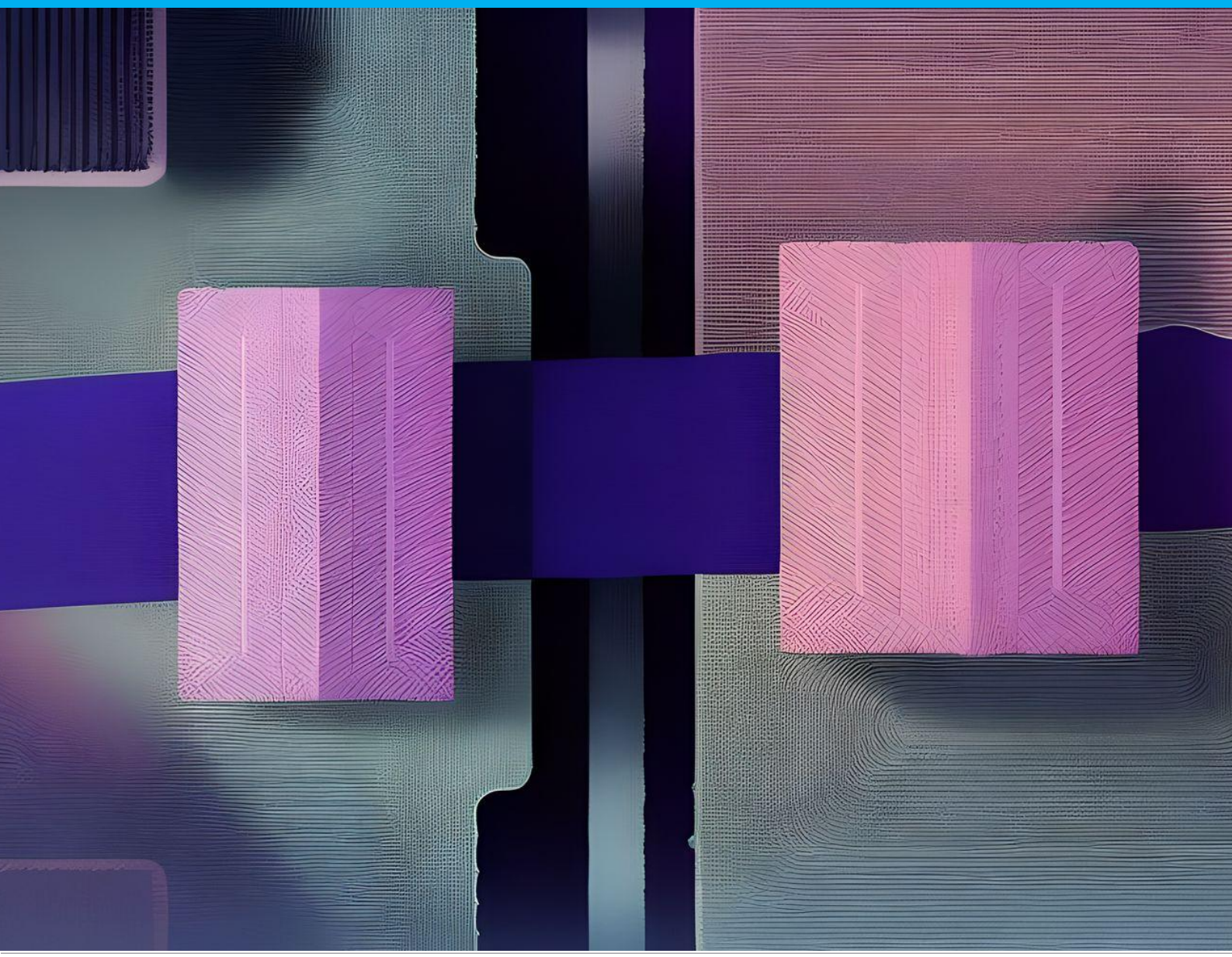

TU Delft Delft University of Technology

Challenge the future

# Tuning dynamics and dissipation dilution in 2D material resonators by MEMS-induced tension

by


## Michiel Wopereis


To obtain the degree of Master of Science in Mechanical Engineering at the Department of Precision and Microsystems Engineering, Delft University of Technology, Delft, The Netherlands.

To be defended on Thursday, January 11, 2024, at 10:00.

Thesis committee: Prof. dr. P.G. (Peter) Steeneken
Dr. G.J. (Gerard) Verbiest
Dr. F. (Farbod) Alijani
Prof. dr. U. (Urs) Staufer
Dr. S. (Sten) Vollebregt


An electronic version of this thesis is available at `http://repository.tudelft.nl/`.


TU Delft

# Preface

The cover image is an AI modification of an SEM image that shows a MEMS device for tensioning clamped graphene membranes. It metaphorically represents that micro-scale innovations can have a profound impact on the macroscopic landscape. Imagine two farmhouses (pink), symbolizing the macro world, standing apart in a silicon meadow, connected by a graphene suspension bridge (blue) spanning a daunting cliff—a representation of connecting the micro and macro world.

This story is not just about technology; it's about expanding the horizons and pushing the boundaries. It shows how micro-scale innovations advance technology and significantly impact the larger world.

*Michiel Wopereis*
*Delft, January 2024*

# Contents

# Chapter 1

# Tunable 2D material resonators

*This chapter introduces the reader to tunable 2D material resonators. It provides an overview of potential sensing applications and examines the state-of-the-art of driving and straining 2D materials. Additionally, it addresses challenges in clamping 2D materials when straining membranes and delves into the linear and nonlinear dynamics of 2D material resonators. Finally, the section emphasizes the motivation behind the thesis as well as its objectives and research questions, which are then followed by an outline of the thesis.*

## 1.1. State-of-the-art

The field of novel sensors is constantly evolving, and 2D materials have shown immense potential due to their exceptional properties. This chapter explores the unique properties of 2D materials and their use in novel applications. In addition, this chapter delves into the current state-of-the-art of controlling the motion of 2D material resonators. The literature review presents a comprehensive analysis of the existing principles of driving and straining, focusing on comparing different actuation methods. The review aims to identify the advantages and disadvantages of each actuation method and any knowledge gaps and potential research opportunities that could be explored in this field.

### Exceptional properties of 2D materials

2D materials like graphene consist of a single-atom-thick layer of carbon atoms tightly arranged in a honeycomb lattice. The atomic structure of 2D materials gives them remarkable properties. First, graphene has excellent mechanical robustness when exposed to repeated bend-relax cycles across a range of bend radii [1]. Additionally, graphene provides high stretchability of up to 20% [2]. This stretchability opens novel opportunities in various fields, such as the use of graphene as an active and reversible hydrogen storage medium [3, 4], engineering band gaps [2] for nanoelectronics [5], and optical devices [6]. Also, graphene has a Young's modulus of 1 TPa [7] and an intrinsic strength of 130GPa [7].

Second, the exceptionally low mass increases the resonance frequency ($f_0 \propto \sqrt{k/m}$). This enhances their sensitivity, making them excellent probes in sensor applications [8]. For example, in mass and force sensing [9–12] and thermal sensing applications [13, 14].

Third, the single-atomic layer, in combination with the high aspect ratio, makes 2D materials extremely flexible out-of-plane. However, they remain very stiff in-plane due to the high Young's modulus [7]. This high flexibility and low stiffness make 2D materials highly sensitive to external forces [10]. When this low stiffness is combined with the high resonance frequency due to the small mass, it can be used in wide-band microphones to detect small sound pressures [15]. Furthermore, the high surface-to-volume ratio makes these resonators very sensitive to thermal fluctuations [14], pressures, and gasses from the environment. Therefore, applications such as pressure sensors [16, 17] and gas sensors [18–20] utilize this property.

Finally, some 2D materials also have remarkable electrical and chemical properties. This makes them compelling for various electrochemical biosensor applications [18, 21], such as graphene-based enzyme biosensors, immunosensors, and DNA biosensors [22]. Moreover, these materials can be transparent, which is beneficial in photovoltaic applications that use a transparent conducting layer for improved efficiency [23].

### Driving and straining of 2D material resonators

Different actuation methods have been developed to control the motion of 2D materials to take advantage of their remarkable properties and create novel sensors. The most common ways of actuating 2D membranes will be discussed: electrostatic actuation, optothermal and electrothermal actuation, base actuation, and actuation by microelectromechanical systems (MEMS).

#### Electrostatic actuation

Electrostatic actuation is frequently used to induce strain in suspended graphene membranes [8, 10, 13, 15, 24–27]. This method requires an electrostatic gate electrode and a conducting membrane such as graphene [24]. A voltage difference is applied between the membrane and the gate electrode to actuate the membrane, generating an electrostatic force. This force deflects the membrane to the electrode and thus induces strain [24]. An illustration and application of electrostatic actuation can be seen in Figure 1.1.

There are some challenges associated with electrostatic actuation. First of all, the membrane pressure created by the electrostatic actuation is dependent on the membrane position [8]. This induces nonlinear effects. To eliminate those effects, the gap size between the electrode and the membrane should be small compared to the membrane size. Also, the membrane displacements should be much smaller than the gap size. In this case, the electric field lines parallel the z-axis, and the parallel-plate estimation holds [8]. Second, the membrane's work-function differences or trapped charges can influence the induced

forces [28]. In particular, when the trapped charges are not uniform, it is not entirely possible to mitigate those effects by an offset voltage [29]. Third, Casimir forces generate downforce on the membrane; this limits the minimum gap distance before the membrane collapses [30]. In addition, the geometry of the electrode can affect the electric field lines near the edges of the membrane, lowering the effective electrostatic force [31]. Also, although electrostatic actuation can easily be implemented in cryogenic environments, it is only limited to conductive materials [24]. Finally, the effects of quantum capacitance can decrease the actuation efficiency [32].

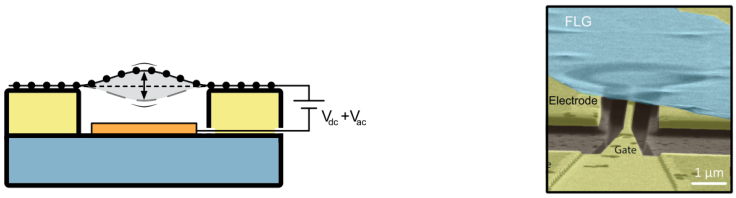


(a) (b)

**Figure 1.1:** (a) Illustration of electrostatic actuation. Adapted from [8] (b) Electrostatically actuated few-layer graphene drum. Adapted from [24]

### Optothermal and electrothermal

The outstanding thermal properties of 2D materials, such as low heat capacitance and high thermal conductivity, can also be used for actuating. This can be utilized to heat membranes very rapidly and efficiently [8]. The most frequently used method for high-frequency actuation is optothermal actuation by using a laser [10, 14, 17, 33]. This is illustrated in Figure 1.2a. Inducing strain was also performed electrothermally by resistive Joule heating of the membrane itself [34] or by a heater platform [35]. When heated, a membrane thermally expands and moves out-of-plane (assuming a positive expansion coefficient). This can be seen in Figure 1.2b.

Using this type of actuation has some drawbacks. For example, it was discovered that the magnitude and direction of the expansion force depend on the membrane properties and geometrical imperfections [36]. As a result, the thermal expansion coefficient can only be estimated experimentally. Furthermore, for optothermal actuation, the optical field intensity and absorption are position-dependent. This can lead to feedback forces influencing the damping and resonance frequency [8]. Moreover, when the light spot radius is too small, there can be a non-uniform spread of temperatures, influencing the resonance frequency [37]. Additionally, optothermal actuation is mainly limited to room temperature, as it is challenging to implement in cryogenic environments [24]. Finally, the membrane can be burned out when the laser power is too high, limiting the maximum driving power.

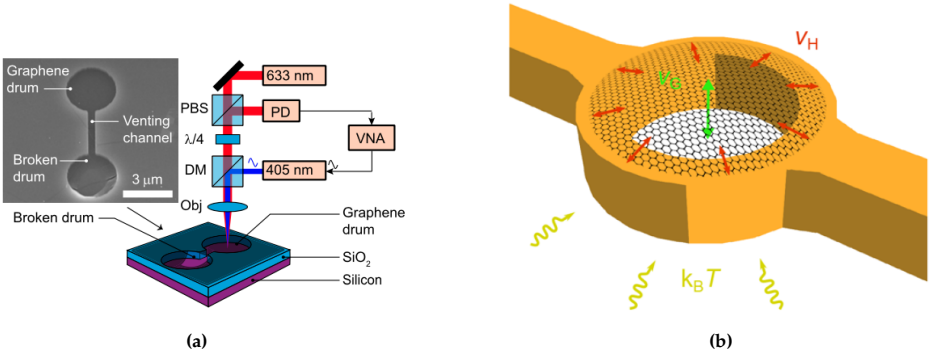


(a) (b)

**Figure 1.2:** (a) Optothermal actuation of a graphene drum. Adapted from [36] (b) Heater platform for electrothermal actuation. Adapted from [35]

### Base actuation

Base actuation involves placing a piezoelectric resonator or a different type of shaker to actuate the substrate. The resonator or shaker generates periodic vibrations that stimulate the substrate with the 2D material. Acoustic waves propagate through the entire substrate and excite the membrane on its edges

[8]. This can be seen in Figure 1.3a. This has been demonstrated by periodically heating a substrate of SiNx with integrated graphene drums using a laser [38]. As a result, the vibrations of the substrate were transferred to the graphene. In another work, a piezoelectric element was used to shake the substrate to resonance frequencies of 4.5MHz [39], see Figure 1.3b.

For base actuation, it should be noted that both the resonances of the membrane and from the actuator will be visible in the motion. Furthermore, in case the mass and stiffness of the base are not orders of magnitude larger than the graphene membrane, coupled equations of motion should be used for analysis [38, 40].

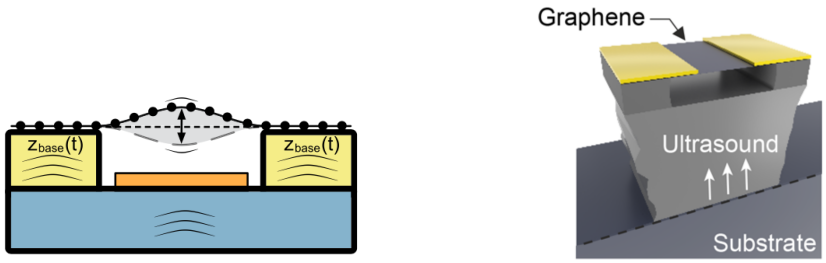


(a) (b)

**Figure 1.3:** (a) Illustration of base actuation. Adapted from [8] (b) Base actuation of suspended graphene using ultrasound. Adapted from [39]

### Actuation with MEMS

Another way of actuating is by using microelectromechanical systems (MEMS). The MEMS is most commonly used to exhibit strain on the membrane to tune the resonator in situ. These hybrid devices are highly suitable in various mechanical, chemical, and optical applications due to their outstanding electrical, mechanical, and optical properties [41]. One study even reported that a graphene-MEMS hybrid device could detect a single hydrogen atom [42].

Moreover, it has been demonstrated that MEMS devices can apply in-plane strain. In a study by Pérez-Garza, the graphene membrane was attached to a suspended shuttle, which could be actuated using a thermomechanical in-plane microactuator (TIM). This made it possible to strain the graphene up to 14% in a controlled, reversible, and non-destructive way [43]. In other studies, in-plane tension was induced with an electrostatic comb-drive actuator [25, 27, 44–46]. Figure 1.4 shows two applications of in-plane straining with MEMS. Although straining by MEMS is promising, it has been observed that when the tensile force is greater than the van der Waals adhesion, the graphene membrane slips [47]. Thus, the membrane should be properly clamped when high strain values are required. The advantage of this method is that it is possible to apply uniaxial strain without influencing the thermal and electrical properties of the membrane.

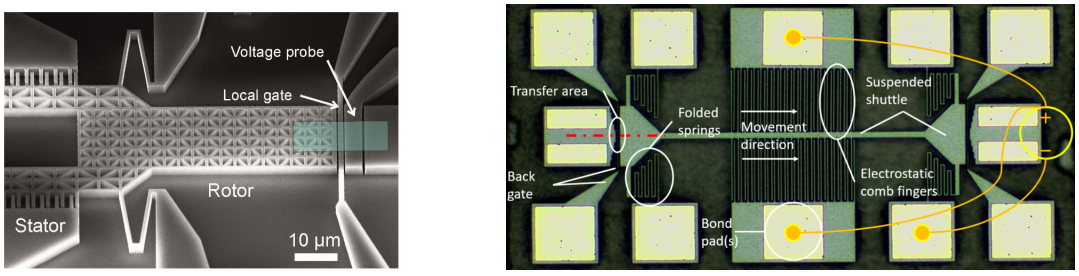


(a) (b)

**Figure 1.4:** (a) MEMS with comb-drive actuator for in-plane tensioning. Adapted from [48] (b) MEMS for applying in-plane tension to a suspended membrane. Adapted from [49]

## Overview

A wide range of driving and straining approaches exist to actuate a 2D resonator. To identify any knowledge gaps and discover the most widely used approaches, a comprehensive literature review

from 2007 to 2023 was conducted to get an overview of the current state-of-the-art. This overview of driving versus straining can be found in Table 1.1. Notably, the overview reveals extensive research into electrostatic actuation, likely due to its independence from external actuators, compatibility with cryogenic conditions, and ease of miniaturization. However, its applicability is limited to conductive materials, and trapped charges can impact the displacements. Additionally, electrostatic actuation deforms the membrane out-of-plane and encounters dissipation losses due to Joule heating. In contrast, straining through MEMS occurs in-plane and can overcome electrostatic dissipation. The upcoming sections will explore the challenges related to MEMS straining and the dynamics of 2D material resonators.

| Driving: \ Straining: | Bending substrate | Electrostatic | Electrothermal | MEMS | Pressure | No straining |
|---|---|---|---|---|---|---|
| **Base** | | [38, 39] | | | | |
| **Electrostatic** | [50] | [10, 13, 27, 31, 33, 35, 48, 51–64] | [34] | [27, 48] | | |
| **Electrothermal** | | [35, 51, 65] | [35] | | | |
| **Optothermal** | [66] | [59, 67] | | [44, 49] | [47] | [14, 36, 68–71] |
| **Parametric resonance using electrostatic driving** | | [26] | | | | |
| **Parametric resonance using optothermal driving** | | | | | | [71–74] |
| **Piezo** | | | [75] | | | |
| **MEMS** | | | | | | |
| **Parametric resonance using MEMS** | | | | | | |
| **No driving** | | [46] | | [25, 45, 46, 76] | [77] | |

**Table 1.1:** Comparison of the available research of straining type (x-axis) vs. driving type (y-axis). Base driving includes ultra-soon and photothermal actuation of the substrate. Electrothermal straining includes laser radiation or Joule heating of the membrane and thermal expansion of the substrate. MEMS straining includes comb-drive and TIM actuators. Pressure straining includes gas blisters.

## 1.2. Tuning 2D material resonators though MEMS-induced tension

MEMS devices can produce in-plane motion and are commonly actuated using electrostatic comb drives and thermal in-plane microactuators. Electrostatic actuation using a comb drive involves applying a voltage potential between two conductive parallel plates, which generates an electrostatic force that pulls the plates together. The distance between the plates can be adjusted by controlling the potential difference. Comb drive actuation is commonly found in the literature to apply in-plane strain [25, 27, 44–46, 48, 49]. On the other hand, thermal actuation operates by thermally expanding the material and cooling it to the environment. This method can generate large forces but is generally slower than electrostatic actuation, making electrostatic actuation more suitable for high-frequency applications [43, 76]. An illustration of electrostatic and thermal actuation can be found in Figures 1.5a and 1.5b, respectively.

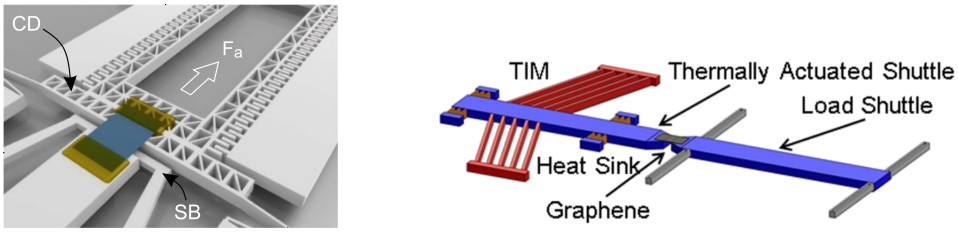


(a) (b)

**Figure 1.5:** Illustration of in-plane actuation methods for straining graphene (a) Electrostatic comb-drive actuator. Adapted from [27]. (b) Thermal in-plane microactuator. Adapted from [43].

## Enhancing the Q-factor

It has been observed that subjecting a 2D membrane to in-plane tensile stress improves its Q factor [44, 66, 78, 79]. This is advantageous for obtaining accurate measurements with minimal noise [8, 41, 79]. For example, force sensors are commonly used to detect signals below resonance. In this case, Equation 1.1 is often used for determining the thermal displacement noise [79], where $Q$ is the mechanical quality factor, $k$ is the lumped stiffness, $k_B$ is the Boltzmann's constant, $\omega_0$ is the resonance frequency and $T$ the resonator temperature. It can be seen that a larger Q-factor leads to less noise away from resonance. Likewise, the thermomechanical noise force can be calculated by Equation 1.2 and also reduces with a higher Q. Finally, a higher mechanical quality factor results in a higher signal-to-noise ratio (SNR). This can be seen in Equation 1.3 [79], where $\alpha$ is the sensor-specific scaling factor, and $S$ is the minimum signal. This motivates the efforts to improve the Q-factor to enhance the performance of devices.

$$X\left(\omega \ll \omega_0\right) = \sqrt{\frac{4k_BT}{k\omega_0 Q}} \tag{1.1}$$

$$F_{th} = \sqrt{4k_BT\frac{m\omega_0}{Q}} \tag{1.2}$$

$$SNR = \alpha S\sqrt{\frac{Q}{4k_BT}} \tag{1.3}$$

## Tuning resonators

The dynamical response to strain for a clamped-clamped membrane resonator primarily depends on its thickness. If the membrane is relatively thick, the membrane behaves like a suspended plate, and the classical plate theory applies [80]. However, in the case of mono-layer graphene, the thickness $t$ approaches zero, corresponding with a negligible bending stiffness [77]. This is the so-called membrane limit where the pretension in the material becomes dominant [41, 44]. To assess whether graphene operates within the membrane limit, Xie conducted a comparative analysis of the experimental mode ratios, specifically $f_2/f_1$ and $f_3/f_1$, against the ratios predicted by a membrane model using finite element method (FEM) simulations in COMSOL Multiphysics and ratios of a doubly-clamped plate according to Equation 1.4, where $L$ is the plate length, $E$ is the Young's modulus, $I$ is the moment of inertia, $\rho$ is the mass density, and $A$ is the cross-section area. The ratio of the doubly-clamped plate was much greater, confirming that graphene was in membrane limit [44].

$$f_n = \frac{k_n^2}{2\pi L^2}\sqrt{\frac{EI}{\rho A}} \tag{1.4}$$

Where $k_n$ is the mode-dependent parameter which should hold[81]:

$$\cosh\left(k_n\right)\cos k_n - 1 = 0, \tag{1.5}$$

Some of the $k_n$ found are $k_1$=4.730, $k_2$=7.5832, $k_3$=10.996, $k_n \approx (n\pi + \pi/2)$ for n>3. In the membrane limit, the fundamental mode frequency can be calculated according to Equation 1.6, where $L$ is the membrane length, $\gamma$ is the 2D tension, $E$ is the Young's modulus, $\rho$ is the mass density and $\varepsilon$ the strain. When there is not an external force, the initial pretension $\gamma_0$ should be calculated with Equation 1.7 [44], where $f_0$ is the resonant frequency without external force, $W$ is the width and $m_{\text{eff}}$ is the effective mass. That formula confirms that the resonance frequency increases proportionally to the square root of the pretension.

$$f = \frac{1}{2L}\sqrt{\frac{\gamma}{\rho t}} = \frac{1}{2L}\sqrt{\frac{E\varepsilon}{\rho}} \tag{1.6}$$

$$\gamma_0 = \frac{8f_0^2 L m_{\text{eff}}}{W} \tag{1.7}$$

In the situation of in-plane straining by comb-drive actuation, additional tension is induced. This

tension shifts the resonance frequency of the 2D material resonator. The coupled resonance frequency can be calculated with Equation 1.8. In case $V_{dc} = 0$, the force induced by the comb-drive $F(V_{dc})$ is zero. The comb-drive force can be calculated with Equation 1.9, where $N$ is the number of teeth, $\epsilon$ the vacuum permittivity, $h$ is the thickness, $d$ is the gap between the fingers and $\eta$ is the efficiency of the force applied to the 2D materials. Finally, both equations can be combined to find the coupling relationship between the comb-drive voltage and resonance frequency of the membrane in Equation 1.10 [44].

$$f = \frac{1}{2}\sqrt{\frac{\gamma_0 W + F\left(V_{\mathrm{dc}}\right)}{2Lm_{\mathrm{eff}}}} \tag{1.8}$$

$$F\left(V_{\mathrm{dc}}\right) = \eta N \frac{\in h}{d} V_{\mathrm{dc}}^2 \tag{1.9}$$

$$f = \sqrt{f_0^2 + \frac{\eta N \in h}{8Lm_{\mathrm{eff}} d} V_{\mathrm{dc}}^2} \tag{1.10}$$

## Clamping resonators to prevent slippage

When straining 2D materials, slippage can occur when the tensile force exceeds the Van der Waals adhesion forces [47]. As a result, an irreversible drop in Q-factor and resonance frequency has been observed [44, 49], thus limiting the maximum achievable strain [43]. In literature, various attempts have been made to increase the Van der Waals adhesion forces by surface treatments of the substrate [82]. Bouman conducted surface treatments in an attempt to decrease surface roughness and increase Van der Waals adhesion forces [49]. Plasma cleaning was attempted to remove nanoscopic contaminants, but no significant improvement in surface roughness was observed after a three-hour exposure. Vapor HF etching was then performed to reduce surface roughness, but this process was unsuccessful and complicated due to fragile suspended parts. Finally, electron beam-induced deposition (EBID) was used to coat the surface with a layer of gold to flatten irregularities and reduce roughness. Unfortunately, this method worsened the surface roughness from 135nm to 187nm (see Figure 1.7). In addition, it resulted in forming a gold-aluminum intermetallic that reduced the electrical conductivity of bond pads. To conclude, the surface treatments didn't significantly affect the surface adhesion; thus, proper clamping is required to prevent slippage and achieve higher strains.

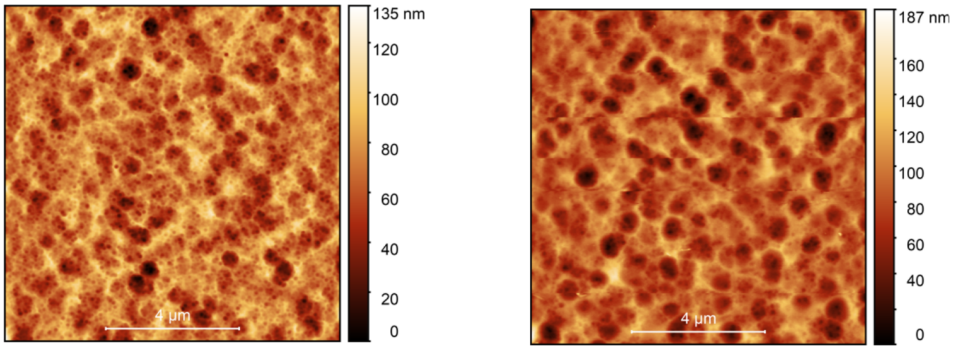


(a) (b)

**Figure 1.6:** AFM measurements of (a) Untreated MEMS device. Adapted from [49]. (b) Au-coated MEMS device. Adapted from [49].

### Dry and wet approaches for clamping 2D materials

Various studies have attempted different techniques to clamp 2D material membranes. These approaches can be broadly categorized into wet and dry methods. Wet methods involve submerging the device in a solution, where the surface tension of the liquid can cause electrostatic comb fingers to pull into each other without additional precautions [49]. On the other hand, dry methods do not require submergence.

One example of a wet method is the study by Verbiest, where an additional layer of PMMA was used for effective clamping [45]. The process involved submerging the entire device in various solutions

and then drying it using critical point drying to prevent damaging the device. This process required an extra electron-beam lithography (EBL) step to link the remaining PMMA on the graphene sheet and the substrate [61]. The study demonstrated that the graphene flake ruptured earlier than the clamping, indicating that an effective clamping was achieved. Figure 1.7a shows a false-colored SEM image of the device. Bouman also pioneered two-photo polymerization to clamp graphene [49]. This method required submerging the entire device in a photoresist and polymerizing it using a focussed electron beam. However, during an experiment using this method, the fingers of the comb drive became stuck when the device was removed from the solution due to the surface tension. This issue is shown in Figure 1.7b.

In contrast, dry methods were used in the studies by Perez-Garza and Xie. Perez-Garza clamped the graphene using an epoxy, which was precisely dispensed on the edges of the material using a femtopipette [43, 76], which is illustrated in Figure 1.7c. The positioning of the pipette was done using a nanomanipulation robot. It is worth noting that strains of up to 14% were measured in the study by Perez-Garza, which is significantly higher than reported in similar studies. Consequently, it is still debatable if the creeping of the epoxy caused this high strain value. In another study, Xie anchored the graphene flake using microdroplets of epoxy positioned by a tapered quartz micropipette as seen in Figure 1.7d [44]. Both studies achieved effective clamping without requiring critical point drying. Electron beam-induced deposition (EBID) is another dry method for clamping graphene. Lee used this technique to deposit a layer of glass ($SiO_2$) on top of graphene, effectively sealing the edges of a graphene drum and preventing leakages as shown in Figure 1.7e [83]. During this literature study, it was observed that EBID could also be a versatile technique to clamp graphene, as shown in Figure 1.7f. However, challenges with this method still exist since the shuttle of the MEMS-actuator moves due to electrical charging from the electron beam.

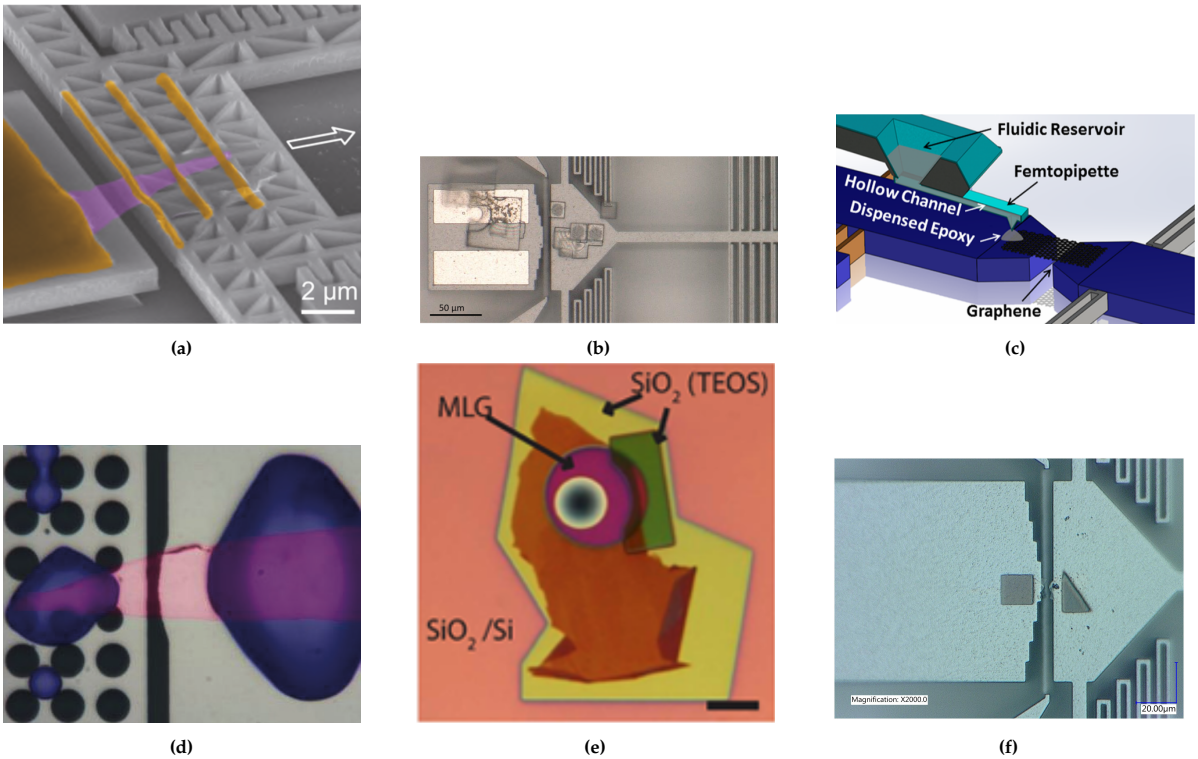


**Figure 1.7:** Different approaches of clamping graphene (a) False-colored SEM image of PMMMA clamping (yellow) on graphene (pink). Adapted from [25]. (b) MEMS with 2PP printed squares and snapped-in comb fingers. Adapted from [49]. (c) Schematic of applying epoxy using a femtopipette. Adapted from [76]. (d) Microdroplets of epoxy on MEMS. Adapted from [44]. (e) Glass ($SiO_2$) sealed graphene drum using EBID. Adapted from [83]. (f) EBID of platinum on MEMS and deposited with an FEI Helios G4 CX (Settings: 5kV, 11nA, 5000x magnification, 1$\mu s$ dwell time, 800nm height)

## 1.3. Dynamics of nanomechanical resonators

In addition to their use in straining applications, MEMS devices can also be used for driving. This is typically achieved through a comb-drive actuator activated by an alternating current (AC) voltage. By adjusting the AC voltage, it is possible to control the desired dynamics of the oscillations. This section describes the linear and nonlinear dynamics, which are often described by a combination of the Duffing, Van der Pol, and Matthieu-Hill equations [55, 72, 73]:

$$m_i\ddot{q}_i + c_i\dot{q}_i + \eta_i q_i^2\dot{q}_i + \left(k_i + k_{p,i0}\cos\left(\omega t - \phi\right)\right) q_i + \gamma q_i^3 = F_{ext,i0}\cos(\omega t - \phi) \tag{1.11}$$

where $q_i$ is the displacement, $m_i$ the modal mass, $c_i$ the damping coefficient, $\eta_i$ the nonlinear damping coefficient, $k_i$ the linear stiffness coefficient, $\gamma$ the nonlinear stiffness coefficient, $k_{p,i0}\cos\left(\omega t - \phi\right)$ the parametric driving and $F_{ext,i0}\cos(\omega t - \phi)$ the direct driving.

### Linear dynamics

In membranes undergoing small displacements, the influence of nonlinear terms diminishes, and the equation of motion can be adequately described using linear terms. The solutions to this linear equation are widely comprehended and can be found in standard textbooks about dynamics [84].

#### Free vibration

Free vibration occurs when the force terms $k_{p,i}$ and $F_{ext,i}(t)$ become zero. This will lead to the harmonic oscillator equation:

$$m_i\ddot{q}_i + c_i\dot{q}_i + k_i q_i = 0 \tag{1.12}$$

Next, when inserting the trial solution $q_i(t) = q_{i,0}e^{\lambda_i t}$, the following equation is obtained:

$$\lambda^2 m_i + \lambda_i c_i + k_i = 0 \tag{1.13}$$

Equation 1.13 can now be solved for $\lambda_i$ when taking the small damping approximation $c_i \ll \sqrt{4k_i m_i}$. This gives the under-damped solutions for $\lambda_i$:

$$\lambda_{i\pm} = -\frac{c_i}{2m_i} \pm i\sqrt{\frac{k_i}{m_i} - \frac{c_i^2}{4m_i^2}} \approx -\frac{\omega_i}{2Q_i} \pm i\omega_i \tag{1.14}$$

where the fundamental resonance frequency corresponds to $w_i = \sqrt{k_i/m_i}$ and the quality factor with $Q_i = \sqrt{k_i/m_i}/c_i$ for a given mode i. Finally, the two solutions of the equation ($q_{i\pm}(t)$) for a given mode i can be obtained:

$$q_{i\pm}(t) = q_{i,0\pm}e^{\frac{-\omega_i}{2Q_i}t}e^{\pm i\omega_i t} \tag{1.15}$$

#### Driven movement

When an external periodic driving force, denoted as $F_{\text{ext,i}}(t)$, is applied to the system, the equation of motion changes. This external force can be expressed as a sum of sinusoidal functions using the Fourier series notation, such that $F_{\text{ext,i}}(t) = F_{\text{ext,i}}(\omega)e^{i\omega t}$. By using this expression, solutions for any waveform can be created. Consequently, in the linear regime, the equation of motion changes to:

$$m_i\ddot{q}_i + c_i\dot{q}_i + k_i q_i = F_{\text{ext,i}}(\omega)e^{i\omega t} \tag{1.16}$$

The frequency response function $FRF(\omega)$ and its compliance $|FRF(\omega)|$ are now stated in Equations 1.17 and 1.18, respectively. The resonance frequency occurs at a phase angle of $\phi = \pi/2$, and a peak in magnitude can be observed at this frequency. This can be seen in Figure 1.8

$$FRF(\omega) = \frac{q_i(\omega)}{F_{\text{ext ,i}}(\omega)} = \frac{1}{-\omega^2 m_i + i\omega c_i + k_i} \tag{1.17}$$

$$\left|\frac{q_i(\omega)}{F_{\text{ext},i}(\omega)}\right| = \frac{1}{\sqrt{(k_i - m_i\omega^2)^2 + (c_i\omega)^2}} \tag{1.18}$$

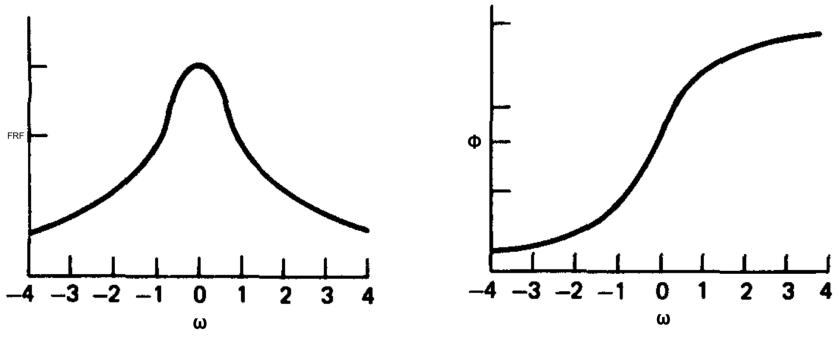


**(a)** Amplitude **(b)** Phase

**Figure 1.8:** Linear response curves. Adapted from [85].

## Nonlinear dynamics

The stiffness can be described in the nonlinear regime with the well-known Duffing equation [8, 26, 86, 87]. For a given mode $i$, the dynamics can be described by Equation 1.19 [8]. This equation contains the nonlinear stiffness term $\gamma q_i^3$, which is amplitude-dependent. Therefore, the effective stiffness becomes $k_{\text{eff,i}} = k_i + \gamma(q_i^2)$. Spring hardening occurs when $\gamma > 0$ and will lead to an increase in resonance frequency with an increase in amplitude ($\omega_i \approx \sqrt{k_{\text{eff,i}}/m_i}$). On the other hand, spring softening occurs when $\gamma < 0$ and will decrease resonance frequency with a higher amplitude. When solving Equation 1.19 analytically with approximating the solution, the frequency response function results in Equation 1.20.

$$m_i\ddot{q}_i + c_i\dot{q}_i + k_iq_i + \gamma q_i^3 = F_{\text{ext}\,i0}\cos(\omega t - \phi) \tag{1.19}$$

$$\left|\frac{q_{i0}}{F_0}\right| = \frac{1}{\sqrt{\left(k_i - m_i\omega^2 + \frac{3\gamma q_{i0}^2}{4}\right)^2 + \left(\frac{\omega_i m_i \omega}{Q_i}\right)^2}} \tag{1.20}$$

The multivaluedness significantly impacts the dynamics since it leads to jumping phenomena [85]. This jumping phenomenon has been observed in experiments with graphene [34, 74, 86]. During the experiments, the amplitude of the excitation frequency was kept constant while the excitation frequency ($\omega$) was gradually varied. Figure 1.9a demonstrates the phenomenon of spring hardening, where an increase in excitation frequency causes the amplitude to rise from point 5 to point 6. However, beyond the resonance frequency, a large drop in amplitude and a significant phase shift occur from point 6 to point 2. Conversely, when the frequency is decreased from point 1, the amplitude increases from point 2 to point 3 and then jumps upward to point 4 at $\omega = \sqrt{k_i/m_i}$ [8]. Figure 1.9b illustrates spring softening, which begins at point 1 with an increase in amplitude as the frequency decreases. After reaching point 3, a significant jump in amplitude occurs, followed by a reduction to point 5.

A graphene membrane's Duffing parameter ($\gamma$) depends on its geometry. As a result, any imperfections in the geometry of the membrane, such as asymmetry, inhomogeneities, or wrinkles that may occur during the transfer process, can impact this parameter [41, 50, 56]. Furthermore, the choice of actuation also affects the duffing parameter. It is observed that electrostatic actuation leads to a softening behavior [63]. In contrast, optothermally driven resonators exhibit a hardening behavior [74].

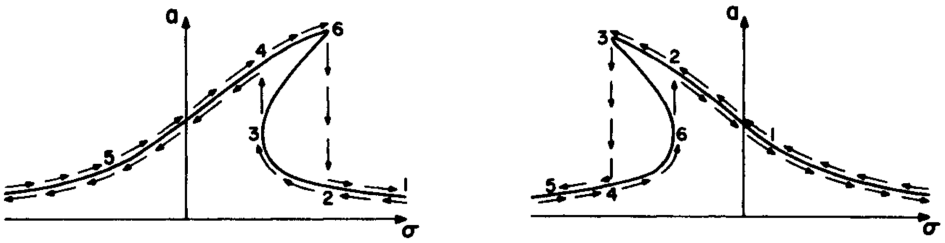


**(a)** Spring hardening ($\gamma > 0$) **(b)** Spring softening ($\gamma < 0$)

**Figure 1.9:** Duffing equations of motion. Adapted from [85].

The damping constant $c_i$ in Equation 1.18 assumes linear dissipation. This is reasonable for small-amplitude resonators [62]. However, the dissipation becomes nonlinear for very small devices [55] or very large amplitudes [88] due to nonlinear damping [89]. In this case, the effective dissipation coefficient becomes $c_{eff,i} = c_i + \eta_i q_i^2$. Thus, in the case of $\eta > 0$, the dissipation increases with an increase in amplitude. It was observed that by increasing the excitation force, the Duffing resonance peak frequency increased due to spring hardening, and at the same time, the peak amplitude decreased due to nonlinear damping [74]. The equation of motion with nonlinear damping results in the following:

$$m_i\ddot{q}_i + (c_i + \eta_i q_i^2)\dot{q}_i + k_i q_i + \gamma q_i^3 = F_{\text{ext}\,i0}\cos(\omega t - \phi) \tag{1.21}$$

## Modal mass and stiffness

In the equations of motion for both free and driven vibrations (see equations 1.12 and 1.16), the variables $m_i$ and $k_i$ represent the modal mass and stiffness. It is important to note that these values are numerical coefficients that depend on factors such as the mode shape, the system's geometry, and the measurement's location. They do not represent the actual mass and stiffness of the system itself [8].

If the modal stiffness and resonance frequency are known, it is possible to calculate the modal mass using the relationship $m_i = k_i/w_i^2$. However, while the resonance frequency can be determined relatively easily through measurements, determining the stiffness is more challenging. For example, in a thin graphene membrane, stiffness is strongly influenced by the pretension in the membrane. Nevertheless, determining this pretension is difficult, as it depends on the specific fabrication method and any imperfections in the device. As a result, this parameter is often determined experimentally.

There are various ways to determine the pretension experimentally. For example, the pretension could be determined by AFM or Raman spectroscopy by calculating the modal dynamic stiffness. Both methods for studying tension and stiffness can be found frequently in the literature [7, 24, 41, 48, 90, 91]. For example, for a doubly-clamped plate, the force vs. deformation relation follows from Equation 1.22 [24, 82, 90]. This equation can be utilized to extract the pretension $T$ by AFM measurements. Typical pretension values for a freely suspended graphene sheet are 0.07-1$Nm^{-1}$ [7, 90, 92]. Moreover, according to expression 1.22, the effective spring constant depends on the geometry as expressed in Equation 1.23. It should be noted that for flakes with 1 to 15 layers, there is no strong dependence on the thickness. Thus the term $\frac{30.78Wt^3}{L^3}$ can be neglected in this regime [24]. This membrane-to-plate crossover can be seen in Figure 1.10.

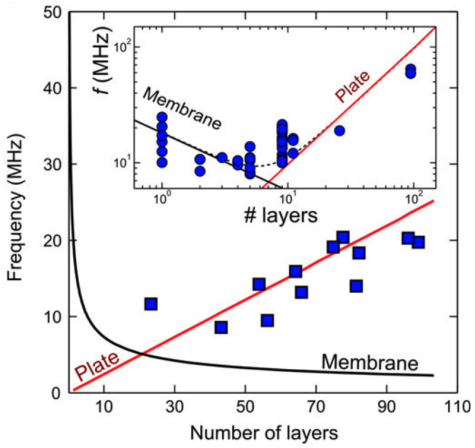


**Figure 1.10:** Membrane-to-plate crossover for multilayered $MoS_2$ circular resonator (D=6$\mu m$). Adapted from [61].

$$F = \left[\frac{30.78Wt^3}{L^3}E + \frac{12.32}{L}T\right]\delta + \frac{8WtE}{3L^3}\delta^3 \tag{1.22}$$

$$k_{\text{eff, doubly-clamped}} = \frac{30.78Wt^3}{L^3}E + \frac{12.32}{L}T \tag{1.23}$$

Another method involves changing the dynamics by tuning the tension in the membrane. Modal stiffness can be extracted by varying pretension and measuring the change in resonance frequency. This can be done by applying an out-of-plane force. For example, electrostatically [54, 93, 94] or by using gas pressure [47, 95]. Important to note is that an electrostatically applied force will include both tension changes and electrostatic softening [8, 94]. Another method to induce tension is to pass a high current through the suspended graphene membrane to heat it by Joule heating [78]. However, in this case, the device must support high temperatures up to 1200K. Finally, a novel way of tuning the tension is by straining using MEMS. These devices can mechanically tension a 2D material membrane in-plane, thus accurately controlling the tension via voltage control. This approach is beneficial because it is unaffected by non-uniform thermal distributions and can achieve a wide tuning range of resonance frequencies [27, 44, 49].

## 1.4. Objective and research questions

The current state-of-the-art sensing devices are reaching their limits. For example, commercially available MEMS-based force sensors have a maximum resolution of 0.5 µN [96] and MEMS capacitive force sensors reach limits of 0.68 µN [97]. Some fields, such as biology, require the ability to sense forces on an even smaller scale. This requires detecting forces that are in the range of nano ($10^{-9}$) or even picoscale ($10^{-12}$). Achieving this level of sensitivity is crucial for gaining a better understanding of the basic components of biological systems [97]. For instance, to comprehend the dynamics of single-cell bacteria, it is necessary to have a force-sensing capability of 6nN [98]. Similarly, to understand the binding forces between biomolecules, which play a crucial role in understanding tumor progression [99] and tissue formation [100], sensitivities as low as 20 pN are required [101].

However, the current MEMS-based force sensors are unable to reach these demanding sensitivities. Therefore, novel sensors made of 2D materials are the subject of intensive research due to their remarkable material properties. These materials are often extremely flexible in the out-of-plane direction yet highly stiff in the in-plane direction, which enhances their sensitivity and makes them promising for various mass, force, pressure, and temperature sensing. Additionally, 2D materials possess high resonance frequencies and can be tuned by moderate applied voltages, which is useful for voltage-controlled oscillators (VCOs) that play a crucial role in modern communication systems for applications such as timing references and frequency modulators. [60]. Extensive research has been conducted on electrostatically tunable 2D material resonators. However, it suffers from dissipation losses caused by

Joule heating. This is a major challenge since 2D material resonators are currently limited by their high dissipation rate, which leads to low Q-factors. Another challenge is the characterization of 2D materials, where a wide variety of elastic moduli is found for the same 2D materials; for example, the Young's modulus of graphene ranges from 430 GPa to 1120 GPa [102, 103].

Hybrid devices that integrate 2D materials on MEMS might overcome these challenges. However, there is limited knowledge regarding 2D material-MEMS hybrid devices to use them as a platform for material characterization or to enhance the properties of 2D material resonators by straining them. Still, they seem promising candidates to reduce dissipation losses by straining membranes in situ, which could lead to dissipation dilution and an improvement of the quality factor [104]. However, they are not commonly used due to challenges associated with transferring, clamping, and pre-deformations.

This study will enable the hunt for ultra-sensitive 2D material resonant sensors with low dissipation losses. It will address the high dissipation rate and explore the force-sensing capabilities in the piconewton scale. It will increase the low Q-factors of typical 2D material resonators by straining them in situ, diluting intrinsic losses. This will be enabled by integrating the membranes on a MEMS platform to induce strain in situ. It will also tackle slippage issues when straining 2D materials with a new fabrication approach to transfer and clamp 2D materials.

This leads to the following research questions:

- How can slippage be prevented in tunable 2D material resonators to maximize their tuning capabilities?
- Can in situ straining of 2D material resonators increase their low Q-factor and provide a platform for higher-Q resonators by diluting intrinsic losses?
- Could a hybrid device combining 2D materials and MEMS effectively analyze the dynamics of 2D materials by employing MEMS-induced tension, ultimately aimed at characterizing the material properties?
- Are 2D material resonators suitable for ultra-sensitive force sensing outperforming sensitivities of commercially available silicon-based devices rated at 0.5µN?

## 1.5. Thesis outline

The first chapter explored the remarkable properties of 2D materials, such as graphene, and its applications in novel sensors. It also discussed state-of-the-art actuation methods like electrostatic, opthothermal, base, and MEMS, comparing their advantages and limitations. It also gave an overview of the current research in tunable resonators by comparing the driving and straining methods. Furthermore, it explored the current challenges in tunable resonators, such as clamping challenges. Finally, it delved into the dynamics of resonators, discussing linear and nonlinear equations governing their behavior.

The second chapter contains a paper on tuning dissipation dilution in 2D material resonators by MEMS-induced tension. This paper describes a novel dry-transfer approach from transferring and clamping 2D materials to manufacture the devices. It also describes the experimental setup for measuring the dynamics. The same experimental setup is used during the whole project. Finally, it provides evidence of dissipation dilution in the 2D material resonators by straining the membranes in situ and measuring their quality (Q)-factor. This enables the hunt for higher-Q resonators based on 2D materials.

The third chapter attempts to characterize 2D materials dynamically via MEMS-induced tension. Two models that describe the dynamic with strain are developed, one that assumes that the membranes are flat and another that incorporates a pre-deformation based on a buckled beam model. In addition, it gives more insight into the topography of the 2D material resonators by analyzing wrinkles, bumps, and pre-deformations using SEM and white light interferometry.

The fourth chapter explores the feasibility of 2D material resonators as ultra-sensitive force sensors. It measures piconewton sensitivities across different 2D material resonators and outperforms MEMS capacitive-based force sensors by about two orders of magnitude.

The final chapter describes the project's conclusion and recommends future studies. In addition, to keep the thesis concise, the following appendices were added. Appendix A includes all the supplementary material of the paper about dissipation dilution: (i) Detailed instructions on fabricating the devices, (ii) MEMS stiffness characterization, (iii) Analytical derivation of the dissipation dilution

model and (iv) frequency vs. voltage measurements of the devices D1-D4 analyzed in the paper. Appendix B includes an analytical derivation of the electrostatic force of the MEMS device. Finally, Appendix C consists of a calculation of the critical out-of-plane deflection for buckled membranes.

# Chapter 2

# Tuning dissipation dilution in 2D material resonators by MEMS-induced tension

*In this paper, a MEMS platform is used for in situ tuning of 2D material resonators to enhance both the resonance frequency and Q-factor. To enable these experiments, a method is developed for the dry transfer and clamping of 2D materials on MEMS actuators, allowing for controlled straining of the 2D materials. By in situ straining, the tensile energy is increased, diluting intrinsic losses and resulting in a remarkable 91% increase in the Q-factor. These findings pave the way for designing high-Q resonators using 2D materials, overcoming their current dissipation rate limitations.*

# Tuning dissipation dilution in 2D material resonators by MEMS-induced tension

Michiel P.F. Wopereis,[1] Niels Bouman,[1] Satadal Dutta,[1] Peter G. Steeneken,[1] Farbod Alijani,[1] and Gerard J. Verbiest[1]

[1] *Department of Precision and Microsystems Engineering, Delft University of Technology, Mekelweg 2, 2628 CD Delft, The Netherlands*

Resonators based on two-dimensional (2D) materials have exceptional properties for application as nanomechanical sensors, which could allow them to operate at high frequencies with high sensitivity. However, the performance of 2D material resonators as nanomechanical sensors is currently limited by their high dissipation rate, resulting in low quality ($Q$)-factors. Here, we make use of micro-electromechanical systems (MEMS) to strain 2D material resonators in situ, enhancing both their resonance frequencies and Q-factors. We dry-transfer 2D materials on the MEMS actuators and use electron beam-induced deposition of platinum to clamp them, thus effectively ruling out slippage at the boundaries. By in-plane straining the membranes in a purely mechanical fashion, we then increase the tensile energy, thereby diluting dissipation. Using our method, we can increase the $Q$-factor of 2D material resonators by 91%, paving the way towards raising the $Q$-factor in resonators based on 2D materials.

## I. INTRODUCTION

Nanomechanical resonators made of two-dimensional (2D) materials are the subject of intensive research due to their remarkable properties. Their low mass, combined with their high Young's modulus, leads to resonance frequencies that are typically a few tens of MHz [1]. Yet, their extreme flexibility in the out-of-plane direction enhances the sensitivity to external stimuli and makes them promising for various applications, including mass [1–4], force[5–7], pressure[6, 8–11], and temperature sensing[6, 12, 13].

The performance of nanomechanical resonant sensors and clocks is generally limited by their dissipation per cycle ($\Delta W$). A low $\Delta W$ results in a high quality ($Q$-)factor, which is the ratio of stored energy $W$ to $\Delta W$ over a single oscillation cycle ($Q = 2\pi W/\Delta W$). A low $\Delta W$ and thus high $Q$-factor physically insulates the resonator from external noise sources, allowing long-term coherent oscillations while minimizing energy dissipation to the environment [14, 15]. Thus, enabling low phase-noise oscillators [16] and high-performance noise-rejection filters [15, 17, 18].

Increasing the tensile stress can be an effective strategy to realize high-$Q$ resonators [19, 20]. The tension leads to an increase in the stored energy $W$ without significantly affecting losses, thereby increasing the ratio $W/\Delta W$ and the $Q$-factor [21], an effect that is commonly known as dissipation dilution. Since this strategy was very successful in realizing high-$Q$ resonators in SiN that can be grown with high intrinsic tensile stress [20], it was also considered as a method for increasing the quality factor of 2D materials that could not be grown with high intrinsic stress. Out-of-plane electrostatic and thermal forces were used to achieve this quality factor tuning [22]. However, attempts to increase the $Q$-factor through out-of-plane electrostatic gating of 2D material membranes typically result in a reduction of the $Q$-factor instead of an increase by dissipation dilution[4, 5, 23]. This reduction is due to the voltage-dependent electronic Joule dissipation of the displacement current within the resonator [23, 24]. Furthermore, the out-of-plane electrostatic pulling force increases side wall adhesion, which facilitates dissipation through coupling with the substrate [22, 25, 26]. Thermal expansion-based tuning strategies [22] have the drawback of making it difficult to distinguish tension effects from other thermal effects on $Q$. For example, the change in membrane temperature changes material parameters, that can increase damping via e.g. the thermoelastic dissipation mechanism[15, 27]. Currently, 2D material resonators have substantially lower quality factors than high-stress silicon nitride devices with $Q > 10^9$ [28, 29]. However, with a dissipation dilution method to increase the $Q$ of 2D to similar values, they might become serious contenders for high-$Q$ sensors and high $fQ$ resonant quantum devices.

In this paper, we set a first towards this goal, by providing evidence of dissipation dilution in suspended 2D material resonators that are controllably tensioned in-plane using a micro-electromechanical systems (MEMS) actuator. To enable these experiments, we introduce a method to precisely suspend 2D materials over MEMS gaps and rigidly clamp them with a layer of platinum using electron-beam-induced deposition (EBID). We actuate the membrane resonances optothermally and record the resulting motion using an interferometry setup, from which we extract the $Q$-factor ($Q$) and resonance frequency ($f_0$). By applying strain with the MEMS actuator to the 2D material resonator in a mechanical and controllable fashion, we find an increase in resonance frequency as well as the $Q$-factor. Our findings thus provide a new way for enhancing the Q-factor of 2D materials via dissipation dilution.

## II. FABRICATION

We use a MEMS actuator that is designed and fabricated in the commercially available XMB10 process from

X-FAB [30, 31]. The resulting device (see Fig. 1) consists of a moving shuttle with 38 comb fingers that is held suspended by four serpentine flexures. The flexures are connected to fixed anchors that have aluminum bond pads for making electrical contact by wire bonding. The crystalline silicon shuttle has a thickness of 15 $\mu$m, length of 520 $\mu$m, comb finger length of 103 $\mu$m, and asymmetric finger spacing of 2.0 $\mu$m and 4.0 $\mu$m. The membranes are suspended over a 6 µm trench between the fixed anchor and the moving shuttle. Inside the trench, at a depth of 5 $\mu$m below the shuttle surface, a suspended silicon beam acts as a mirror for interferometric readout of the membrane motion. In order to transfer the membranes onto the MEMS actuator, we first mechanically exfoliate 2D materials [32] onto a 5 mm × 5 mm PDMS sheet on a microscope slide. Next, we use a microscope to select membranes on the PDMS sheet with a minimum length of 20 µm such that they can cover the suspended trench as well as parts of the fixed anchor and the moving shuttle. Membranes are selected based on their flatness and uniformity. Once we find a suitable membrane, we use a dome-shaped PDMS stamp covered with a sacrificial polypropylene carbonate (PPC) film to pick it up from the PDMS sheet[33]. The utilization of a PDMS dome results in a smaller contact area with the MEMS actuator, approximately 350 µm in diameter, which allows the precise positioning of a membrane while minimizing contaminations. We then bring the membrane on the PDMS dome in contact with the MEMS actuator and heat the stage to 110°C (above the melting point of PPC). This causes the PPC film to melt and ensures the transfer of the membrane onto the designated area (see Fig. 1(b)). After the transfer, we wire bond the MEMS actuator and connect all terminals to a common ground; this crucial step prevents any electrostatic force-induced movement during the rest of the fabrication process. Next, we remove the PPC film from the membrane and the MEMS actuator through annealing in a high vacuum oven at a pressure below $10^{-5}$ mbar for 3 hours at a temperature of 300 °C (exceeding the decomposition temperature of PPC[34]). After annealing, we inspect the sample optically to confirm the PPC removal (see Fig. 1(c)). Finally, we clamp the membrane with a layer of platinum using EBID [35]. Detailed information on the fabrication procedure is available in Supporting Information S1.

In total, we fabricated 4 devices (D1-D4) with different 2D materials using the method outlined above (see Table I). Figure 1(e) shows a schematic cross-section of a device including the dimensions. All membranes have a suspended length of 6µm, width $w$, and thickness $t$, as determined with a white light interferometer (see Table I).

To mechanically tension 2D materials with the MEMS actuators (see Figs. 1(f)-(g)), we apply a potential difference $V_{\mathrm{cd}}$ between the comb fingers. Due to the asymmetric placement of the comb fingers (see Fig. 1(h)), a force $F_{\mathrm{cd}} = -\frac{1}{2}\frac{\partial C}{\partial x}V_{\mathrm{cd}}^2$ will act on the moving shuttle and will tension the membrane and the four serpentine flexures. Here, $\frac{\partial C}{\partial x}$ is the change in capacitance $C$ between the comb fingers with respect to a change in position $x$ of the moving shuttle.

Based on their geometry, the MEMS actuators used here can controllably strain membranes up to ≈ 11%, which is set by the maximum in-plane displacement of ≈ 0.67 µm (1/3 of the 2 $\mu$m actuation gap) over a 6 µm suspended length. As the maximum in-plane displacement is the limiting factor, pre-deformations and wrinkles in 2D materials [22, 26, 36] can reduce the maximum achievable strain. Moreover, the bare MEMS actuator has a pull-in voltage of 13.5 ± 0.5 V (see Supporting Information 2). As a result, if the stiffness of the 2D membrane stiffness is low, e.g. because it is wrinkled, the MEMS actuator will collapse at this voltage. However, for certain devices, the stiffness of the 2D membrane was high, such that it increased the total device stiffness significantly with respect to that of the MEMS springs and, as a consequence, led to an increase in the pull-in voltage. We were able to apply voltages up to 60 V for device D4 without a pull-in, which demonstrates that the force and stiffness provided by the 2D material were substantial.

## III. MEASUREMENTS

We measure the dynamics of the membranes using an optical interferometry setup (see Fig. 2(a)). The devices are placed in a vacuum chamber with a pressure below $10^{-5}$ mbar and are actuated using a blue diode laser ($\lambda$ = 405 nm) that is power-modulated through a vector network analyzer (VNA). We use a red He-Ne laser ($\lambda$ = 632 nm) to measure the motion of the membrane as its reflected intensity highly depends on the distance between the membrane and the mirror (see Fig. 2(b)). The intensity of the reflected red laser light is detected using a photodiode and further processed by the VNA. Figure 2(c) shows a typical response recorded by the VNA. We observe multiple peaks in the spectrum that we identify as resonance frequencies. To analyze these further, we fit the frequency response $M$ of the fundamental resonance to the well-known harmonic oscillator model[15, 37, 38]:

$$M(f) = \frac{\left(Af^2/Q\right)}{\sqrt{\left(f_0^2 - f^2\right)^2 + \left(\frac{f_0 f}{Q}\right)^2}}, \tag{1}$$

where $f_0$ is the resonance frequency in Hz, $Q$ is the quality factor, and $A$ is the peak amplitude. Figure 2(c) shows this fit on the frequency response of device D4 at $V_{\mathrm{cd}} = 2$ V, from which we extract a resonance frequency of 8.22 MHz. We then repeat the measurement for different $V_{\mathrm{cd}}$ (see Fig. 2(d)) to analyze the dependence of $f_0$ and $Q$ on the applied force $F_{\mathrm{cd}}$. As Fig. 2(d) shows, we see an increase in $f_0$ with applied $V_{\mathrm{cd}}$ due to the increase in tension in the membrane, which is in agreement with results reported in the literature [39–42].

| Device | Material | Clamped | w ($\mu m$) | t (nm) | $Q_{\rm int}/f^2_{\rm plate}$ ($Hz^{-2}$) | $Q_{\rm int}$ | $Q_{\rm ext}$ |
|---|---|---|---|---|---|---|---|
| D1 | Graphene | No | 7.2 | 9.8 ± 0.33 | $7.084 \times 10^{-12}$ | $< 71$ | 182 |
| D2 | Graphene | No | 16.7 | 22.47 ± 0.15 | $2.106 \times 10^{-12}$ | $< 127$ | $> 1000$ |
| D3 | MoS2 | Yes | 19.9 | 77.79± 0.33 | $1.362 \times 10^{-12}$ | $< 64$ | 180 |
| D4 | WS2 | Yes | 16.0 | 94.39 ± 0.23 | $2.515 \times 10^{-12}$ | $< 203$ | $> 1000$ |

TABLE I. Characteristics of fabricated devices D1-D4, including 2D material, clamped using EBID of platinum, width $w$, thickness $t$ and fitted parameters $Q_{\rm int}/f^2_{\rm plate}$ and $Q_{\rm ext}$, where, $Q_{\rm int}$ is the intrinsic quality factor due to bending and elongation losses, $f_{\rm plate}$ is the resonance frequency due to the bending rigidity and $Q_{\rm ext}$ is damping from extrinsic dissipation sources (see Eq. (3)). The membrane thickness is determined using AFM. The width is obtained by measuring an optical or SEM image.

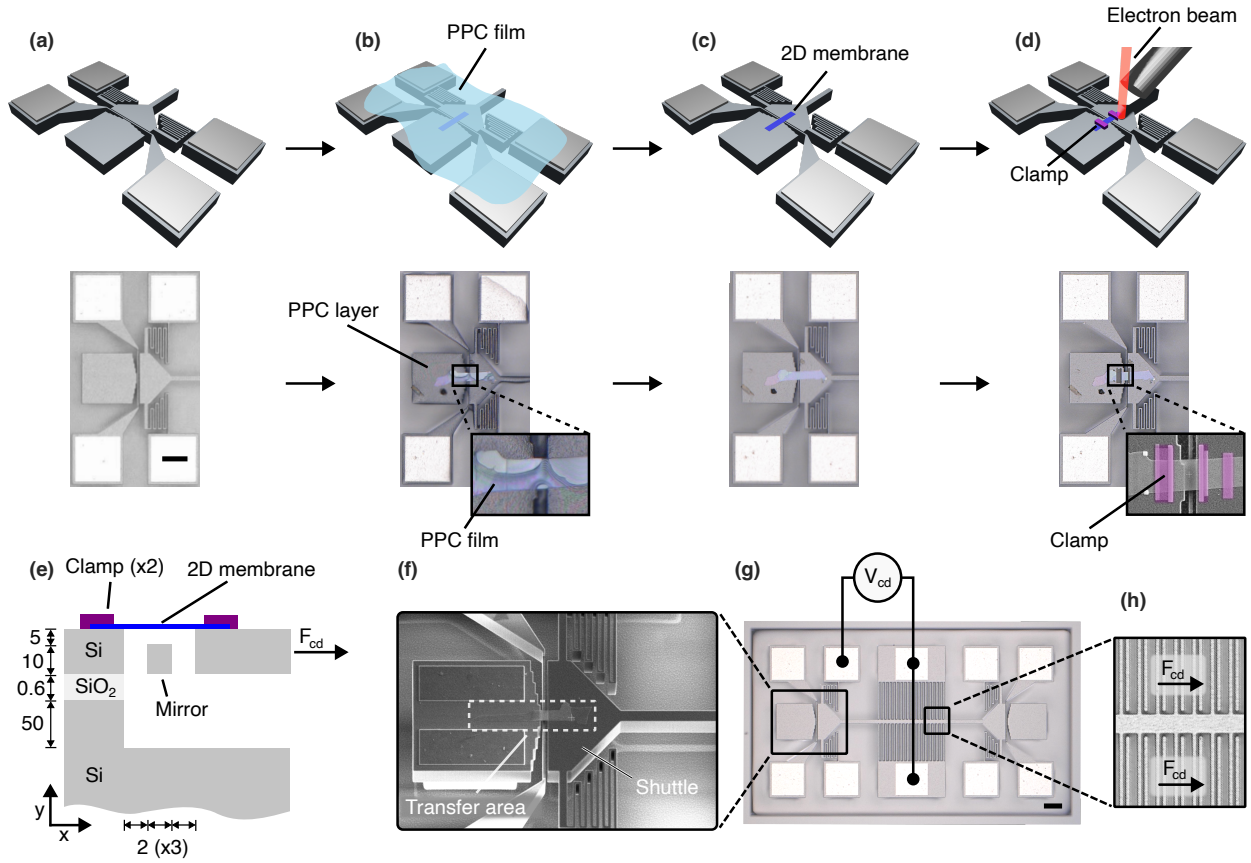


FIG. 1. Device geometry: drawings, optical and SEM micrographs. a) Device straining platform. Scale bar: 50 micrometers. b) Device after the membrane transfer using a sacrificial PPC layer. c) Device after annealing. d) Illustration of the EBID process, an optical image of the device after clamping, and a false-colored SEM image highlighting the platinum clamps. e) Side view of the final device. Dimensions are in micrometers. f) SEM image under an angle of the device. g) Top view of an empty MEMS actuator. Scale bar: 50 micrometers. Voltage over comb drive fingers ($V_{\rm cd}$). h) Detailed view of the comb drive indicating the direction of the comb drive force ($F_{\rm cd}$).

## IV. CLAMPING OF 2D MATERIAL RESONATORS

To evaluate the effectiveness of a deposited layer of platinum using EBID in clamping 2D material resonators, we compare the response of an unclamped device (D1) to the response of a clamped one (D3). We vary the comb-drive force $F_{\rm cd}$ for both devices by varying $V_{\rm cd}$. In a single sweep, we start at $V_{\rm cd} = 0$ V, increase the voltage to a maximum $V_{\rm max}$, return to 0 V, decrease the voltage to $-V_{\rm max}$, and finally return to 0 V. For each subsequent sweep, we increase $V_{\rm max}$ by 1 V up to a maximum of 5 V for device D1, to gradually increase the maximum force exerted on the membrane and monitor the shift in the fundamental resonance. Figure 3 shows $f_0$ as a function of $V_{\rm cd}$ extracted from one such experiment for devices D1 and D3. For the unclamped device (see Fig. 3(a)), we observe a significant decrease in $f_0$ at $V_{\rm cd} = 0$ V after each voltage sweep. At the last measurement point at 0

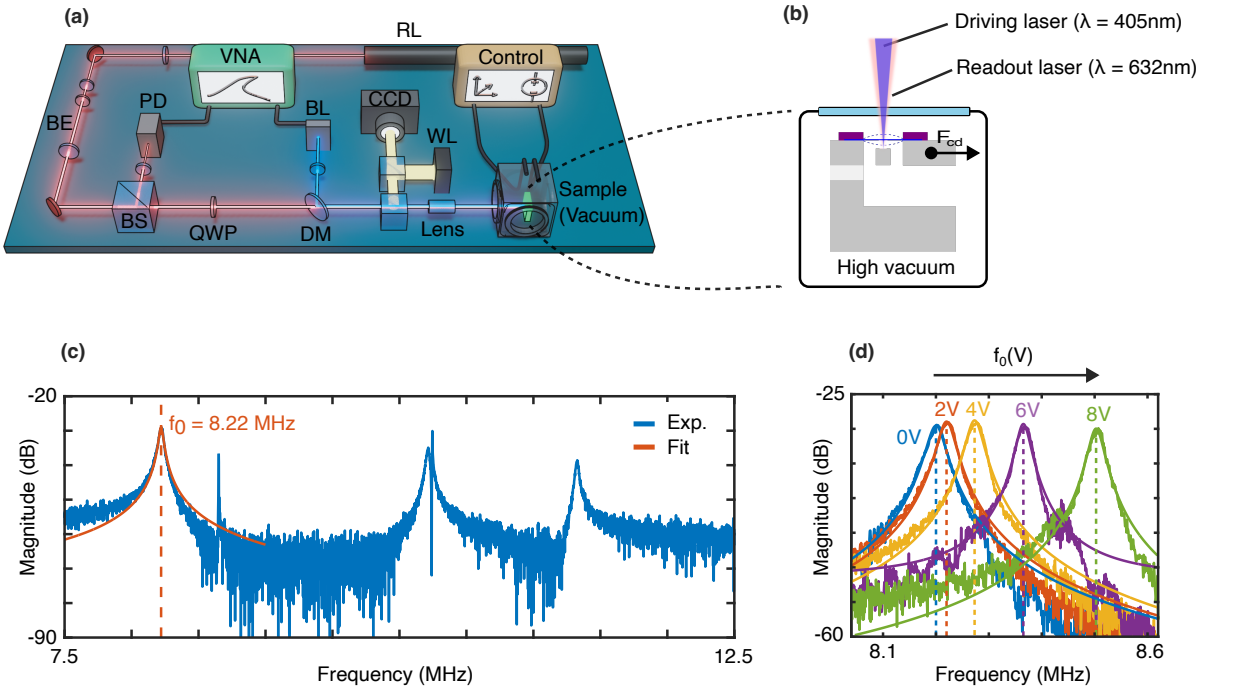


FIG. 2. Device measurements. (a) Fabry-Perot Interferometry setup for measuring the resonance frequencies. Vector Network Analyser (VNA), $V_{cd}$ and stage control (control), Beam expander (BE), Beam splitter (BS), Quarter wave plate (QWP), Dichroic mirror (DM), White light source (WL), Photodetector (PD), Red ($\lambda = 632$ nm) He-Ne Laser (RL), Blue ($\lambda = 405$ nm) Diode Laser (BL). (b) Side view of the device inside the high vacuum chamber. (c) Fitting the harmonic oscillator equation on the experimental data of the VNA for device D4 at $V_{cd} = 2$ V to extract the resonance frequency ($f_0$) and quality factor (Q). (d) experimental data of the VNA for device D4 for $V_{cd} = 0$ V, 2 V, 4 V, 6 V, and 8 V (DC).

V, $f_0$ shows an irreversible reduction from 4.30 MHz to 3.73 MHz, which corresponds to a decrease of approximately 13% with respect to the very first measurement on this membrane. The permanent reduction of $f_0$ might be attributed to irreversible slippage, unsticking, or ironing out the wrinkles that increase the effective length of the membrane, reduce its tension, and thus resonance frequency. This is in contrast to recent observations of a reversible sliding scenario where a closed $f_0$ vs. $V_{cd}$ loop is expected [43].

In contrast to the unclamped device D1, device D3 contains a clamped membrane, as depicted in the inset of Fig. 3(b). As Fig. 3(b) shows, we observe a notably different $f_0$ vs. $V_{cd}$ response when compared to the unclamped device. Initially, $f_0$ measures 7.49 MHz, ascending to 13.67 MHz at 30 V and decreasing back to 7.42 MHz at 0 V, a change of less than 1 %. In subsequent sweeps, the resonance frequency at $V_{cd} = 0$V remains stable within a range of 0.02 MHz. These measurements show that the resonance frequency $f_0$ of the device D3 is much more stable than that of the unclamped device, even at substantially higher actuation voltages, resulting in a 36 times larger force ($F_{cd} \propto V_{cd}^2$) than applied in measurements on device D1. This difference between the clamped and unclamped devices indicates that the deposited layer of platinum using EBID is effective in preventing permanent tension reduction during MEMS actuation. Since the EBID clamps are separated by a few microns from the edge of the trench and thus cannot significantly affect unwrinkling and adhesion mechanisms inside the trench, we also conclude that the irreversible changes in $f_0$ in Fig. 3(a) are most likely due to slippage of a large part of the flake over the silicon surface.

Furthermore, it's worth noting that the maximum voltage of 30 V significantly surpasses the pull-in voltage $V_{PI}$ of the bare MEMS actuator, which was determined to be $13.5 \pm 0.5$ V (see Supporting information S2), providing evidence that the clamped membrane generates substantial force on the shuttle, thus preventing its pull-in and collapse. Simultaneously, according to Newton's third law, we conclude that the MEMS actuator effectively pulls and strains the clamped membranes. An equivalent observation for unclamped device D2 and clamped device D4 can be found in Supporting information S4.

## V. DISSIPATION DILUTION

By fitting resonance peaks like in Fig. 2(d), we extract both the quality factor $Q$ and resonance frequency $f_0$. To study the effectiveness of the MEMS actuator in tuning the quality factor by dissipation dilution, we plot $Q$ vs

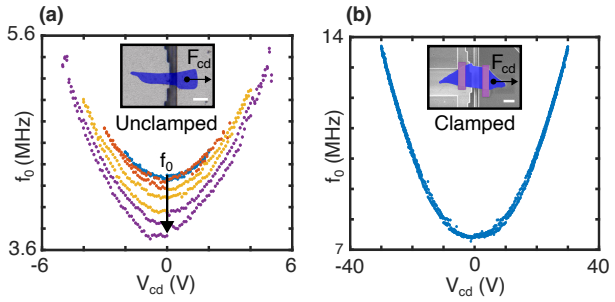


FIG. 3. Comparison of the resonance frequency ($f_0$) versus the comb drive voltage ($V_{\rm cd}$). $F_{\rm cd}$ indicates the pulling direction of the suspended shuttle by the comb drive actuator. Scale bars: 10 micrometers. a) Unclamped device D1, $V_{\rm max}$ = 2 V (blue), 3 V (orange), 4 V (yellow) and 5V (purple), false-colored optical image (blue: 2D membrane) b) Device D3 clamped with a platinum layer deposited by EBID,$V_{\rm max}$ = 30 V (blue), false-colored SEM image (blue: 2D membrane, purple: platinum clamps)

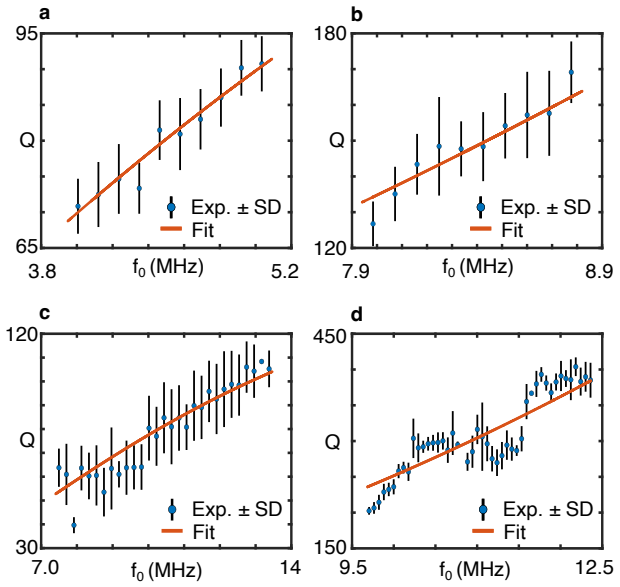


FIG. 4. Dissipation dilution in unclamped device D1-D2 and clamped devices D3-D4. Quality factor ($Q$) versus the resonance frequency ($f_0$). The unclamped devices exhibit a decline in $f_0$ and $Q$ due to slippage, in contrast with the clamped devices, which show consistent values for $f_0$ and $Q$ at $V_{\rm cd}$ = 0 V. a) Experimental data from unclamped device D1 from the $V_{max}$ = 4 V-cycle. The device starts at $f_0$ = 4.17 MHz and $Q$ = 73.5 and stops at $f_0$ = 3.96 MHz and $Q$ = 69.0 due to slippage b) Experimental data from unclamped device D2 from the $V_{max}$ = 12 V-cycle. The device starts at $f_0$ = 8.45 MHz and $Q$ = 150 and stops at $f_0$ = 7.95 MHz and $Q$ = 113 due to slippage. c) Experimental data of clamped device D3 from the $V_{max}$ = 30 V-cycle. The device maintains a consistent $f_0$ and $Q$ of 7.50 MHz and 63.8, respectively. d) Experimental data of clamped device D4 from the $V_{max}$ = 60 V-cycle. The device maintains a consistent $f_0$ and $Q$ of 9.70 MHz and 202, respectively.

$f_0$ for both unclamped and clamped devices over the full actuation voltage range in Fig. 4. It is seen that the $Q$-factor of all devices increases with $f_0$, as expected in a dissipation dilution scenario. For instance, device D4 experiences a 30% increase in $f_0$ and a 91% increase in Q. Interestingly, despite the presence of slipping effects, this trend even seems to hold for the unclamped devices D1 and D2 shown in Figs. 4(a) and (b), respectively.

We now compare the experimental relation between $f_0$ and $Q$ with theory. From literature[14], the quality factor $Q_D$ of a resonator in the presence of dissipation dilution is given by (see Supporting information S3):

$$Q_D \approx \left(\frac{f_0}{f_{\rm plate}}\right)^2 Q_{\rm int}, \tag{2}$$

where $f_0$ is the measured resonance frequency, $f_{\rm plate}$ is the frequency in the presence of bending rigidity, and $Q_{\rm int}$ is the intrinsic dissipation. In the presence of other external dissipation mechanisms with quality factor $Q_{\rm ext}$, the total $Q$-factor can be further reduced[15, 19] to a value $Q$:

$$\frac{1}{Q} = \frac{1}{Q_D} + \frac{1}{Q_{\rm ext}} \tag{3}$$

We fit Eq. (3) to the experimental data in Fig. 4 with $Q_{\rm int}/f_{\rm plate}^2$ and $Q_{\rm ext}$ as fit parameters (orange lines). We provide the fitting values in table I. Note that the fitted lines are almost linear because they span only a small frequency range. For the fit parameter $Q_{\rm int}/f_{\rm plate}^2$, we find a similar order of magnitude for all devices. For devices D1 and D3, we fitted an extrinsic damping contribution of $Q_{\rm ext} \approx 180$. For devices D2 and D4, the data could be fitted well without assuming an external dissipation source $Q_{\rm ext}$, and therefore, we took $1/Q_{\rm ext} = 0$. The good agreement between the experimental data and the fitted curves using Eq. (3) provides evidence that dissipation dilution can account for the observations.

## VI. DISCUSSION

In the previous sections, we studied the effect of in-plane stress on the $Q$-factor and resonance frequency of membranes made of multi-layered 2D materials. The results show that the quality factor can be enhanced by generating tension on the 2D material membranes, and the obtained data matches reasonably well with a dissipation dilution model. We note that this observation does not rule out other mechanisms that may affect the quality factors. These include (i) mode coupling to other modes of the membrane [44–46], (ii) a change in dissipation rate $\Delta W$ with applied tension [26, 47, 48], (iii) changes in the membrane's geometry with increasing tension, which

could be attribued to suppressing wrinkles [36, 49], or (iv) the release of edge adhesion during membrane straining [50], which facilitates the transfer of energy from the resonating membrane to the substrate, leading to acoustic radiation losses [51]. Future work could focus on systematically studying these effects as a function of applied tension.

The main advantage of using a MEMS actuator to apply the tension is that it provides a pure in-plane force, in contrast to thermal, electrostatic gating, or gas pressure-based approaches, where the force is accompanied by other effects that might modify $Q$. The presented method also has some limitations. First of all, actuator device fabrication, design, and wire bonding are time-consuming. Moreover, the actuation range is limited to 1/3 of the actuator gap, although other actuator designs can provide a more extensive range. Finally, transferring membranes to a movable shuttle is a complicated task and can affect membrane suspending and adhesion to the MEMS actuator.

A key prospect of the presented work is the ability to apply MEMS tensioning to significantly raise the quality factor of 2D materials, with the aim to eventually scale it down to the monolayer limit and outperform record silicon nitride/carbide devices [28, 29, 52]. Although currently, $Q$s of 2D materials seem to be limited by their low stress and by fabrication artifacts like wrinkles, in the monolayer limit, the intrinsic $Q_{\mathrm{int}}$ of 2D materials might be much higher than that of multilayer materials since interlayer dissipation mechanisms and thermoelastic damping are largely eliminated [53]. Moreover, for sensing applications, like resonant mass sensors, the large aspect ratio and low mass of 2D materials can increase sensitivity. In this respect, the high ultimate tensile stress of 2D materials like graphene, which was demonstrated to exceed 10 GPa [54], can potentially outperform the tension limitations of even silicon carbides [52].

Moreover, it is of interest to evaluate the minimum measured $Q$ in more detail. For device D4, we found a $Q$ of 202. Disregarding the small effect of pre-stress, we expect this $Q$ to be roughly equal to the intrinsic $Q$ since the thickness of the membrane is relatively high and the intrinsic $Q$ is primarily governed by the bending contribution. This intrinsic $Q$ is over 32 times lower than that of silicon nitride, for which a value of $69t$ nm$^{-1}$ was found[55], which for a thickness equal to that of device D4 of 94.39 nm evaluates to $Q_{\mathrm{int}} = 6513$. A question for further study is if the low intrinsic $Q$ in device D4 is due to the intrinsic crystal properties of $WS_2$ compared to SiN or if the value is limited by imperfections such as wrinkles. It is clear that the MEMS implementation of dissipation dilution demonstrated in this work, which results in a $Q$ enhancement up to 91%, is only a first step toward Q-factor engineering of 2D materials and by no means is yet as efficient as that in SiN resonators, where $Q/Q_{\mathrm{int}}$ factors of over $10^4$ are reached [28].

## VII. CONCLUSION

To conclude, we show signatures of dissipation dilution in 2D material resonators. We use a MEMS actuator to strain the membrane uniaxially and thus tune the resonance frequency and $Q$-factor. To induce dissipation dilution, we developed a device fabrication method using dry transfer of membranes on the MEMS actuator and a clamping technique using EBID of platinum to prevent edge-slippage. The MEMS platform can also be used to study slipping and sliding effects, where slipping was observed to reduce both the Q-factor and $f_0$, in line with the dissipation dilution mechanism that increases $Q$ with MEMS actuation force. By pulling on the membranes, we control the in-plane tension of the membranes, which resulted in an increase in resonance frequency $f_0$ of 30% and an accompanying increase of 91% in the $Q$ factor. Our results enable a leap in developing higher-$Q$ resonators based on 2D materials with potential applications in sensing, time-keeping, and information processing.

## SUPPORTING INFORMATION

The following files are available free of charge.

- supporting-information.pdf:
  S1: Detailed fabrication instructions
  S2: MEMS stiffness characterization
  S3: Derivation of the dissipation dilution model
  S4: $f_0$ vs V measurements for devices D2 and D4

## I. ACKNOWLEDGEMENTS

We would like to thank the Plantenna research program funded by the 4TU federation and Europractice for providing the design tools and multi-project wafer service.

[1] A. Sakhaee-Pour, M. T. Ahmadian, and A. Vafai, Applications of single-layered graphene sheets as mass sensors and atomistic dust detectors, Solid State Communications **145**, 168 (2008).

[2] B. Lassagne, D. Garcia-Sanchez, A. Aguasca, and A. Bachtold, Ultrasensitive mass sensing with a nanotube electromechanical resonator, Nano Letters **8**, 3735 (2008).

[3] J. Atalaya, J. M. Kinaret, and A. Isacsson, Nanomechanical mass measurement using nonlinear response of a graphene membrane, Europhysics Letters **91**, 48001 (2010).

[4] V. Singh, S. Sengupta, H. S. Solanki, R. Dhall, A. Allain, S. Dhara, P. Pant, and M. M. Deshmukh, Probing thermal expansion of graphene and modal dispersion at low-temperature using graphene nanoelectromechanical systems resonators, Nanotechnology **21**, 165204 (2010).

[5] P. Weber, J. Guttinger, A. Noury, J. Vergara-Cruz, and A. Bachtold, Force sensitivity of multilayer graphene optomechanical devices, Nat Commun **7**, 12496 (2016).

[6] M. C. Lemme, S. Wagner, K. Lee, X. Fan, G. J. Verbiest, S. Wittmann, S. Lukas, R. J. Dolleman, F. Niklaus, H. S. J. van der Zant, G. S. Duesberg, and P. G. Steeneken, Nanoelectromechanical sensors based on suspended 2d materials, Research (Wash D C) **2020**, 8748602 (2020).

[7] I. E. Rosłoń, A. Japaridze, P. G. Steeneken, C. Dekker, and F. Alijani, Probing nanomotion of single bacteria with graphene drums, Nature Nanotechnology **17**, 637 (2022).

[8] J. Romijn, S. Vollebregt, R. J. Dolleman, M. Singh, H. S. Van Der Zant, P. G. Steeneken, and P. M. Sarro, A miniaturized low power pirani pressure sensor based on suspended graphene, in *2018 IEEE 13th Annual International Conference on Nano/Micro Engineered and Molecular Systems (NEMS)* (IEEE, 2018).

[9] R. J. Dolleman, D. Davidovikj, S. J. Cartamil-Bueno, H. S. J. Van Der Zant, and P. G. Steeneken, Graphene squeeze-film pressure sensors, Nano Letters **16**, 568 (2016).

[10] D. Shahdeo, A. Roberts, N. Abbineni, and S. Gandhi, Graphene based sensors, in *Analytical Applications of Graphene for Comprehensive Analytical Chemistry*, Comprehensive Analytical Chemistry (2020) pp. 175–199.

[11] J. H. Choi, J. Lee, M. Byeon, T. E. Hong, H. Park, and C. Y. Lee, Graphene-based gas sensors with high sensitivity and minimal sensor-to-sensor variation, ACS Applied Nano Materials **3**, 2257 (2020).

[12] R. J. Dolleman, G. J. Verbiest, Y. M. Blanter, H. S. J. Van Der Zant, and P. G. Steeneken, Nonequilibrium thermodynamics of acoustic phonons in suspended graphene, Physical Review Research **2**, 10.1103/physrevresearch.2.012058 (2020).

[13] H. Liu, G. Baglioni, C. B. Constant, H. S. van der Zant, P. G. Steeneken, and G. J. Verbiest, Enhanced photothermal response near the buckling bifurcation in 2d nanomechanical resonators, arXiv preprint arXiv:2305.00712 (2023).

[14] L. Sementilli, E. Romero, and W. P. Bowen, Nanomechanical dissipation and strain engineering, Advanced Functional Materials **32**, 2105247 (2022).

[15] J. M. L. Miller, A. Ansari, D. B. Heinz, Y. Chen, I. B. Flader, D. D. Shin, L. G. Villanueva, and T. W. Kenny, Effective quality factor tuning mechanisms in micromechanical resonators, Applied Physics Reviews **5**, 041307 (2018).

[16] D. Leeson, A simple model of feedback oscillator noise spectrum, Proceedings of the IEEE **54**, 329 (1966).

[17] T. B. Gabrielson, Fundamental noise limits for miniature acoustic and vibration sensors, Journal of Vibration and Acoustics **117**, 405 (1995).

[18] T. Gabrielson, Mechanical-thermal noise in micromachined acoustic and vibration sensors, IEEE Transactions on Electron Devices **40**, 903 (1993).

[19] S. Schmid, *Fundamentals of Nanomechanical Resonators* (2016).

[20] S. S. Verbridge, J. M. Parpia, R. B. Reichenbach, L. M. Bellan, and H. G. Craighead, High quality factor resonance at room temperature with nanostrings under high tensile stress, Journal of Applied Physics **99**, 124304 (2006).

[21] S. A. Fedorov, N. J. Engelsen, A. H. Ghadimi, M. J. Bereyhi, R. Schilling, D. J. Wilson, and T. J. Kippenberg, Generalized dissipation dilution in strained mechanical resonators, Physical Review B **99**, 10.1103/physrevb.99.054107 (2019).

[22] D. Davidovikj, M. Poot, S. J. Cartamil-Bueno, H. S. J. Van Der Zant, and P. G. Steeneken, On-chip heaters for tension tuning of graphene nanodrums, Nano Letters **18**, 2852 (2018).

[23] N. Morell, A. Reserbat-Plantey, I. Tsioutsios, K. G. Schädler, F. Dubin, F. H. L. Koppens, and A. Bachtold, High quality factor mechanical resonators based on wse<sub>2</sub> monolayers, Nano Letters **16**, 5102 (2016).

[24] X. Song, M. Oksanen, M. A. Sillanpää, H. G. Craighead, J. M. Parpia, and P. J. Hakonen, Stamp transferred suspended graphene mechanical resonators for radio frequency electrical readout, Nano Letters **12**, 198 (2012).

[25] J. Rieger, A. Isacsson, M. J. Seitner, J. P. Kotthaus, and E. M. Weig, Energy losses of nanomechanical resonators induced by atomic force microscopy-controlled mechanical impedance mismatching, Nature Communications **5**, 10.1038/ncomms4345 (2014).

[26] P. G. Steeneken, R. J. Dolleman, D. Davidovikj, F. Alijani, and H. S. J. van der Zant, Dynamics of 2d material membranes, 2D Materials **8**, 10.1088/2053-1583/ac152c (2021).

[27] R. Lifshitz and M. L. Roukes, Thermoelastic damping in micro- and nanomechanical systems, Physical Review B **61**, 5600 (2000).

[28] D. Shin, A. Cupertino, M. H. J. de Jong, P. G. Steeneken, M. A. Bessa, and R. A. Norte, Spiderweb nanomechanical resonators via bayesian optimization: Inspired by nature and guided by machine learning, Advanced Materials **34**, 2106248 (2022).

[29] A. Cupertino, D. Shin, L. Guo, P. G. Steeneken, M. Bessa, and R. Norte, *Centimeter-scale nanomechanical resonators with low dissipation* (2023).

[30] X. Zou, S. Ahmed, N. Jaber, and H. Fariborzi, A compact high-sensitivity temperature sensor using an encapsulated clamped-clamped mems beam resonator, in *2021 21st International Conference on Solid-State Sensors, Actuators and Microsystems (Transducers)* (IEEE).

[31] P. Streit, R. Forke, S. Voigt, U. Schwarz, R. Ziegenhardt, S. Weidlich, D. Billep, M. Gaitzsch, and H. Kuhn, Vibration sensors with a high bandwidth and low snr, enhanced with post processing gap reduction, in *2022 23rd International Conference on Thermal, Mechanical and Multi-Physics Simulation and Experiments in Microelectronics and Microsystems (EuroSimE)* (IEEE).

[32] K. S. Novoselov, D. Jiang, F. Schedin, T. J. Booth, V. V. Khotkevich, S. V. Morozov, and A. K. Geim, Two-dimensional atomic crystals, Proceedings of the National Academy of Sciences **102**, 10451 (2005).

[33] K. Kinoshita, R. Moriya, M. Onodera, Y. Wakafuji, S. Masubuchi, K. Watanabe, T. Taniguchi, and T. Machida, Dry release transfer of graphene and few-

layer h-bn by utilizing thermoplasticity of polypropylene carbonate, npj 2D Materials and Applications **3**, 10.1038/s41699-019-0104-8 (2019).

[34] S. Wang, Y. Huang, B. Liao, G. Lin, G. Cong, and L. Chen, Structure and properties of poly(propylene carbonate), International Journal of Polymer Analysis and Characterization **3**, 131 (1997).

[35] M. Lee, D. Davidovikj, B. Sajadi, M. Siskins, F. Alijani, H. S. J. van der Zant, and P. G. Steeneken, Sealing graphene nanodrums, Nano Lett **19**, 5313 (2019).

[36] R. J. Nicholl, H. J. Conley, N. V. Lavrik, I. Vlassiouk, Y. S. Puzyrev, V. P. Sreenivas, S. T. Pantelides, and K. I. Bolotin, The effect of intrinsic crumpling on the mechanics of free-standing graphene, Nature Communications **6**, 8789 (2015).

[37] R. M. Schmidt, G. Schitter, and A. Rankers, *The design of high performance mechatronics-: high-Tech functionality by multidisciplinary system integration* (Ios Press, 2020).

[38] R. S. Figliola and D. E. Beasley, *Theory and design for mechanical measurements* (John Wiley & Sons, 2014).

[39] G. J. Verbiest, M. Goldsche, J. Sonntag, T. Khodkov, N. von den Driesch, D. Buca, and C. Stampfer, Tunable coupling of two mechanical resonators by a graphene membrane, 2D Materials **8**, 035039 (2021).

[40] M. Goldsche, G. J. Verbiest, T. Khodkov, J. Sonntag, N. V. D. Driesch, D. Buca, and C. Stampfer, Fabrication of comb-drive actuators for straining nanostructured suspended graphene, Nanotechnology **29**, 375301 (2018).

[41] J. Sonntag, M. Goldsche, T. Khodkov, G. Verbiest, S. Reichardt, N. V. Den Driesch, D. Buca, and C. Stampfer, Engineering tunable strain fields in suspended graphene by microelectromechanical systems, in *2019 20th International Conference on Solid-State Sensors, Actuators and Microsystems & Eurosensors XXXIII (TRANSDUCERS & EUROSENSORS XXXIII)* (IEEE).

[42] Y. Xie, J. Lee, Y. Wang, and P. X. Feng, Nanoelectromechanical systems: Straining and tuning atomic layer nanoelectromechanical resonators via comb-drive mems actuators (adv. mater. technol. 2/2021), Advanced Materials Technologies **6**, 2170008 (2021).

[43] Y. Ying, Z.-Z. Zhang, J. Moser, Z.-J. Su, X.-X. Song, and G.-P. Guo, Sliding nanomechanical resonators, Nature Communications **13**, 10.1038/s41467-022-34144-5 (2022).

[44] X. Wang, D. Zhu, X. Yang, L. Yuan, H. Li, J. Wang, M. Chen, G. Deng, W. Liang, Q. Li, S. Fan, G. Guo, and K. Jiang, Stressed carbon nanotube devices for high tunability, high quality factor, single mode ghz resonators, Nano Research **11**, 5812 (2018).

[45] A. Keşkekler, O. Shoshani, M. Lee, H. S. J. Van Der Zant, P. G. Steeneken, and F. Alijani, Tuning nonlinear damping in graphene nanoresonators by parametric–direct internal resonance, Nature Communications **12**, 10.1038/s41467-021-21334-w (2021).

[46] A. Keşkekler, V. Bos, A. M. Aragón, F. Alijani, and P. G. Steeneken, Multimode nonlinear dynamics of graphene resonators, Physical Review Applied **20**, 064020 (2023).

[47] C. Zener, Internal friction in solids. i. theory of internal friction in reeds, Physical Review **52**, 230 (1937).

[48] S. Schmid, K. D. Jensen, K. H. Nielsen, and A. Boisen, Damping mechanisms in high-q micro and nanomechanical string resonators, Physical Review B **84**, 10.1103/physrevb.84.165307 (2011).

[49] R. J. Nicholl, N. V. Lavrik, I. Vlassiouk, B. R. Srijanto, and K. I. Bolotin, Hidden area and mechanical nonlinearities in freestanding graphene, Physical Review Letters **118**, 10.1103/physrevlett.118.266101 (2017).

[50] R. J. Dolleman, Y. M. Blanter, H. S. J. Van Der Zant, P. G. Steeneken, and G. J. Verbiest, Phonon scattering at kinks in suspended graphene, Physical Review B **101**, 10.1103/physrevb.101.115411 (2020).

[51] P. Steeneken, J. Ruigrok, S. Kang, J. Van Beek, J. Bontemps, and J.-J. Koning, Parameter extraction and support-loss in mems resonators, arXiv preprint arXiv:1304.7953 (2013).

[52] M. Xu, D. Shin, P. M. Sberna, R. Van Der Kolk, A. Cupertino, M. A. Bessa, and R. A. Norte, High-strength amorphous silicon carbide for nanomechanics, Advanced Materials 10.1002/adma.202306513 (2023).

[53] N. Lindahl, D. Midtvedt, J. Svensson, O. A. Nerushev, N. Lindvall, A. Isacsson, and E. E. B. Campbell, Determination of the bending rigidity of graphene via electrostatic actuation of buckled membranes, Nano Letters **12**, 3526 (2012).

[54] M. Goldsche, J. Sonntag, T. Khodkov, G. J. Verbiest, S. Reichardt, C. Neumann, T. Ouaj, N. Von Den Driesch, D. Buca, and C. Stampfer, Tailoring mechanically tunable strain fields in graphene, Nano Letters **18**, 1707 (2018).

[55] L. Villanueva and S. Schmid, Evidence of surface loss as ubiquitous limiting damping mechanism in sin micro- and nanomechanical resonators, Physical Review Letters **113**, 10.1103/physrevlett.113.227201 (2014).

# Chapter 3

# Dynamical 2D material characterization through MEMS-induced tension

*This chapter analyzes the dynamic characterization of 2D materials by MEMS-induced tension. It analyses the topography and experimental dynamics of four devices and considers two dynamical models intending to extract the Young's modulus. One model assumes that the membranes are flat, and another incorporates an out-of-plane deformation.*

## 3.1. Introduction

Nanomechanical resonators made of two-dimensional (2D) materials are the subject of intensive research due to their remarkable properties, allowing them to operate at high frequencies with high sensitivity. This makes them ideal candidates to outperform current silicon-based sensors, such as force sensors, which reach sensitivity limits of 0.5 µN [96]. However, difficulties in manufacturing, which lead to wrinkles and pre-deformations [8, 41, 50, 56, 82, 93], have prevented them from reaching their full potential. Even the simplest graphene nano drums exhibited nanometer-scale wrinkles as observed using AFM [93].

These imperfections might explain the large deviations in reported Young's modulus values. For example, reported values for Young's modulus $E$ of monolayer graphene range from 430 GPa to 1120 GPa [102, 103], and for MoS2, it ranges from 160 GPa to 370 GPa [105, 106]. Therefore, there is a clear need to better understand pre-deformations in 2D material membranes and their effect on material characterization. This section aims to measure the Young's modulus of 2D materials by studying their dynamics under MEMS-induced tension. Furthermore, it will make a step toward comprehending wrinkles and pre-deformations in these devices under tension. The experimental setup and approach discussed in section 2 will be used to measure the dynamics. Two models will be used to characterize $E$. One model will assume that the membranes are flat to extract $E$ from the stress/strain relation. Another model will incorporate a pre-deformation that could explain the different dynamical behaviors observed in the devices and other studies [44].

For this study, four devices are fabricated with different 2D materials (see Table 3.1). The devices are manufactured using a novel dry-transfer method to accurately position 2D material membranes on MEMS-actuators as discussed in Appendix A - S1.

This study will give insight into the importance of the topography and pre-deformations in 2D material resonators for dynamically characterizing the material properties. This improved understanding of the topography and dynamics under tension will lead to better comprehending their complex behavior. These findings could pave the way for the development of ultrasensitive resonant force sensors that could potentially outperform those currently available on the market and characterize $E$ in a purely mechanical fashion via in situ straining.

| Device | Material | $\rho$ (kg/m$^3$) | $w$ (µm) | $t$ (nm) | $E_{\text{lit.}}$ (GPa) | $E_{\text{m1}}$ (GPa) | $E_{\text{m2}}$ (GPa) |
|---|---|---|---|---|---|---|---|
| D3 | MoS2 | 5006 [107] | 19.9 | 77.79 ± 0.33 | 160 [105] | | |
| D4 | WS2 | 7500 [108] | 16.0 | 94.39 ± 0.23 | 150 [109] | | |
| D5 | Graphene | 2267 [110] | 7.9 | 65.9 ± 0.7 | 430 [102] | $1.3 \times 10^{-3}$ | |
| D6 | FePS3 | 3375 [111] | 11.7 | 129.8 ± 1.1 | 103 [111] | | 7.4 |

**Table 3.1:** Characteristics of fabricated devices and fitted Young's modulus $E$, including 2D material, density $\rho$, width $w$, thickness $t$, $E$ from literature $E_{\text{lit.}}$, $E$ from the flat membrane dynamical model $E_{\text{m1}}$ and $E$ from the pre-deformation model $E_{\text{m2}}$. The thickness of devices D3-D4 is measured using AFM, and the thickness of D5-D6 is measured using white light interferometry. The width is obtained by measuring a SEM image.

## 3.2. Results

### 3.2.1 Topography analysis of 2D material resonators under MEMS-induced tension

A good understanding of the topography of 2D membranes is important since it can influence the dynamics[44]. In most studies for material characterization of 2D materials, the membranes are assumed to be flat with uniform deformation [105, 112]. This section demonstrates that although the membranes appear flat on high-resolution SEM images, white light interferometry reveals large deviations in geometry, wrinkles, and bumps. These deviations impact the dynamics of the 2D material resonators. Four 2D material resonators will be strained under MEMS-induced tension.

The results for devices D3-D6 can be seen in Figure 3.1. It was discovered that all devices have pre-deformations, which range from about 60 nm in Figure 3.1(b2) up to 4 $\mu$m in Figure 3.1(c2). In Figure 3.1(c2), wrinkles were observed in the suspended part of the membrane. When the voltage was increased to 14.1 V, there was a pull-in of the MEMS actuator. Thus, the fingers of the comb drive stuck together, resulting in an axial displacement of 2 $\mu$m. The membrane can be seen after the pull-in in Figure 3.1(c3). The interferometry image shows that most wrinkles were flattened out, but there is still a pre-deformation of approximately 1 $\mu$m. In the interferometry images of the other devices (Figures 3.1(b)-(d)), pre-deformations are also visible, and the membranes appear uneven with noticeable bumps, hills, and valleys.

Interestingly, the Si-2D material interface between the clamps and the cavity does not always appear flat. For instance, at the bottom of Fig. 3.1(b2), an out-of-plane deformation of 60 nm can be observed. After straining, the deformation shown in Figure 3.1(b3) becomes even larger. Additionally, a wrinkle is also present on the left side just before the cavity, as seen in Figs. 3.1(c2)-(c3). Thus, it can be seen that the membrane does not always adhere to the Si substrate.

It is worth noting the changes in pre-deformations of the membranes before and after straining, which might explain the strain fields of the membranes. In Fig. 3.1(a2), it can be observed that the bottom part of the membrane is almost flat with $z_0 \approx 0$ nm, whereas the top and center areas are deformed with $z_0 > \approx 35$ nm. After a voltage of 30 V is applied in Fig. 3.1(b3), the deformation seems to be similar, which might suggest that only the bottom part of the membrane is effectively strained. Likewise, in Fig. 3.1(b2)-(b3), only the center part of the membrane appears to be flat, and the out-of-plane deformation on the edges is even increased after a voltage is applied, especially on the top area of the membrane (see Fig. 3.1(b3)).

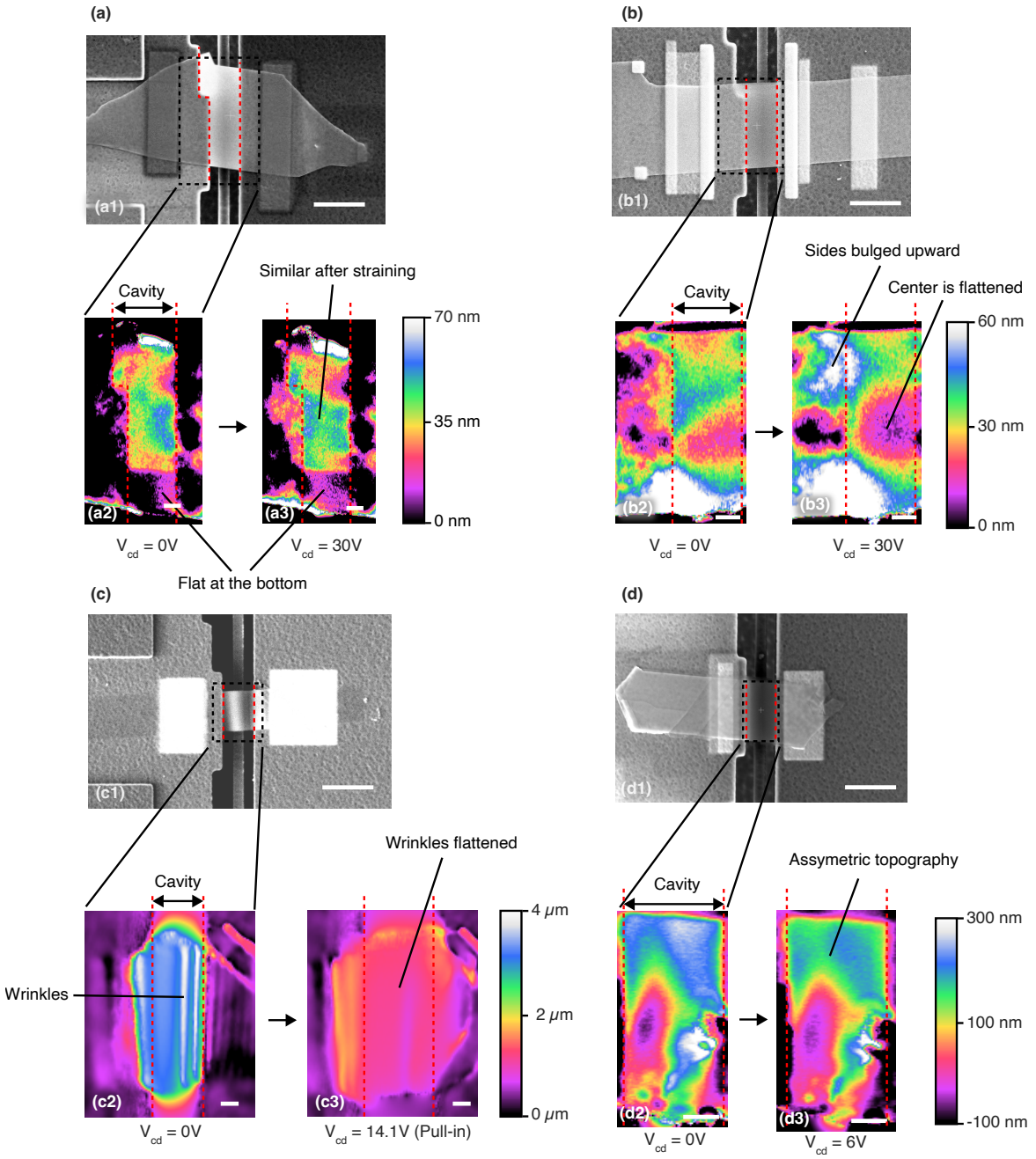


**Figure 3.1:** Images of device D3-D6 showcasing sub-image 1 (SEM, scale bar: 10 µm), sub-image 2 (white light interferometer, before straining, scale bar: 2 µm) and sub-image 3 (white light interferometer, post-straining, scale bar: 2 µm). Red dashed lines represent the cavity ($L$ = 6µm). Black dashed lines represent the view area of the white light interferometry. a) Device D3. The top and center seem to be slightly affected by strain. b) Device D4. The sides bulge up after straining. c) Device D5. Wrinkles are noticeable before straining, which are flattened after straining. d) Device D6.

### 3.2.2 Dynamics of tunable 2D material resonators

2D material resonators are strained under MEMS-induced tension ($F_{\mathrm{cd}} \propto V_{\mathrm{cd}}^2$ according to Eq. (1.9)), and the fundamental resonance frequency $f_0$ is measured at a particular voltage. Figure 3.2 shows $f_0$ versus $V_{\mathrm{cd}}$ for devices D3-D6. An increase in $f_0$ with $V$ is observed for devices D3-D5. In contrast, device D6 initially exhibits a decrease in $f_0$, which saturates and eventually increases again, forming a w-shaped $f_0$ vs. $V_{\mathrm{cd}}$ curve. Comparing the increase in $f_0$ with increasing $V_{\mathrm{cd}}$ for devices D3-D5 reveals deviations. In the 0 V to 12 V voltage range, $f_0$ of devices D3 and D4 increase with ≈13% and ≈5%,

respectively (see Figs. 3.2(a)-(b)). This is in contrast with device D5, which displays a slight increase of ≈2% in $f_0$ (see Fig. 3.2(c)). This minor increase in $f_0$ might be due to the large pre-deformation observed in Fig. 3.1(c2). Notably, despite all devices being firmly clamped through the procedure outlined in section 2, a frequency drop of ≈0.3% is measured from 16.54 MHz to 16.50 MHz when comparing the initial measurement with the last measurement at $V_{cd}$=0 V for device D6 (see Fig. 3.2(d).

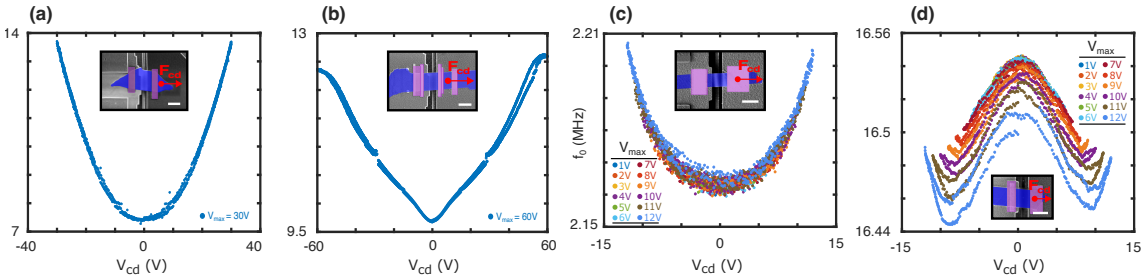


**Figure 3.2:** Fundamental resonance frequency ($f_0$) vs. voltage ($V$) for devices D3-D6. a) $f_0$ vs. $V$ for device D3. Voltage sweep with $V_{max}$ = 30 V. b) $f_0$ vs. $V$ for device D4. Voltage sweep with $V_{max}$ = 60 V. c) $f_0$ vs. $V$ for device D5. 12 voltage sweeps from $V_{max}$ = 1 V to $V_{max}$ = 12 V. d) $f_0$ vs. $V$ for device D6. 12 voltage sweeps from $V_{max}$ = 1 V to $V_{max}$ = 12 V.

### 3.2.3 Flat membrane dynamical model: Extracting stress and strain

This section aims to understand the dynamics of 2D material resonators and examines the assumption of a flat membrane. A model will be introduced to extract the stress $\sigma$ and strain $\epsilon$ in the membranes. These values will be used to estimate the Young's modulus knowing $E = \sigma/\epsilon$. The membrane will be modeled as a flat string with negligible bending rigidity. The bending rigidity will be neglected since the change in tension dominates the change in $f_0$ [24].

$$f = \sqrt{\frac{\sigma}{4L^2\rho}}, \tag{3.1}$$

Equation (3.1) can be used to relate the change in stress ($\Delta\sigma$) with the change in $f_0$, since $f_0$ at a $V_{cd}$ is experimentally determined [44]:

$$\Delta\sigma(V) = 4L^2\rho(f_0(V)^2 - f_0^2), \tag{3.2}$$

The movement of the shuttle ($x$) determines the strain ($\epsilon$) in the membrane, assuming the membranes are flat. When a voltage is applied over the comb drive, the force induced by the comb drive ($F_{cd}$) is balanced by MEMS flexures holding the shuttle ($F_{kcd}$), and the force in the membrane ($F_{2d}$) following Newton's third law (see Fig. 3.3(a)). Therefore, $F_{cd}$ should balance $F_{kcd}$ and $F_{2d}$ such that the summation of forces is 0:

$$F_{sum} = F_{cd} - F_{2d} - F_{kcd} = 0, \tag{3.3}$$

The axial force in the membrane can be calculated from the change in stress, which is known from the dynamics:

$$F_{2d} = \Delta\sigma w t, \tag{3.4}$$

Moreover, $F_{kcd} = k_{cd}x$, where $k_{cd}$ refers to the stiffness of the comb drive serpentine flexures, which is calculated in Appendix A - S2. Also, $F_{cd}$ can be determined using a parallel plate approximation and is derived in Appendix B. Finally, $x$ can be solved by solving the force balance (Eq. (3.3)):

$$\frac{A\,V^2\,\varepsilon_0\left(d_2{}^2 - d_1{}^2 + 2\,x\,(d_1 + d_2)\right)}{2\,(d_2 + x)^2\,(d_1 - x)^2} - 4wtL^2\rho(f_0(V)^2 - f_0^2) - k_{cd}x = 0, \tag{3.5}$$

Assuming the membranes are flat implies $\Delta L = x$, allowing to estimate the membrane strain as $\epsilon = \Delta L/L = x/L$, where $L$ represents the suspended length of the membrane ($L$ = 6 µm). In Figure 3.3(b), the stress-strain relation for device D5 demonstrates a linear increase in stress with strain. Employing a linear fit provides the ratio $\Delta\sigma/\epsilon$ to estimate Young's modulus, resulting in approximately 1.3 MPa,

which is orders of magnitude lower than the literature values (see Table 3.1). Additionally, this device exhibits a comb drive pull-in at 14 V, equivalent to an empty MEMS actuator (see Appendix A - S2). This suggests that the stiffness of the membrane is almost negligible, which could be explained by the large pre-deformation observed in Fig 3.1(c2)-(c3). Notably, Eq. (3.5) could not be solved for devices D3-D4, since $F_{\text{sum}} > 0$ for every $x > 0$. Thus, they have been excluded from this analysis. Interestingly, device D6 in Fig.3.3(c) initially shows a decrease in stress, followed by an increase at $\epsilon = 0.026$. This shows that this model is unsuitable for 2D material resonators with an initial decrease in $f_0$ upon axial strain. This might be the result of buckling causing a decrease in out-of-plane stiffening with strain [113]. The next section will examine the dynamics of pre-deformed 2D material resonators.

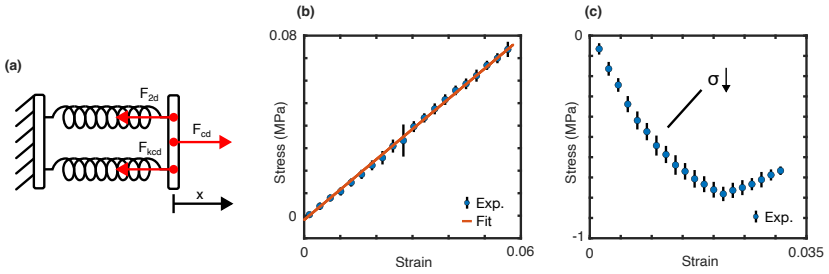


**Figure 3.3:** Stress-strain model. a) Illustration of the force equilibrium of a device. b) Stress vs. strain relation for device D5. Fit $\sigma/\epsilon = 1.3$ MPa c) Stress vs. strain relation for device D6. Showing an unrealistic decrease in stress with applied tension

### 3.2.4 Dynamics of pre-deformed membranes under MEMS-induced tension

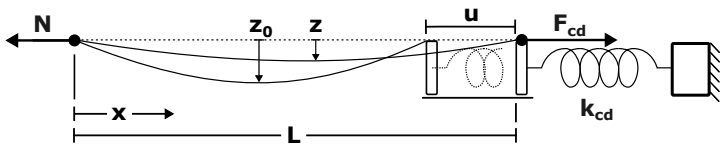


**Figure 3.4:** Schematic representation of a pre-deformed membrane under MEMS-induced tension. Axial force in the membrane $N$, membrane length $L$, pre-deformation before straining $z_0$, pre-deformation at $V_{\text{cd}}$ $z(V)$, axial displacement $u$, comb-drive force $F_{\text{cd}}$ and comb drive stiffness $k_{\text{cd}}$

As observed in Fig. 3.1, out-of-plane pre-deformations occur during fabrication. A model has been developed in this section to comprehend the impact of a buckled membrane on dynamics under MEMS-induced tension. This model aims to characterize $E$ from the dynamics and understand the w-shaped $f_0$ vs. $V_{\text{cd}}$ dynamics in Fig. 3.2(d), as well as in unraveling the multiple fitting regimes in the earlier studies [44].

The model represents a buckled beam and is illustrated in Fig. 3.4. Here, the membrane is modeled with a pre-deformation $z_0$. This deformation decreases to $z$ when the membrane moves with an axial displacement $u$ due to the MEMS-induced tension. Additionally, the suspension of the comb drive shuttle with the serpentine flexures, having a stiffness $k_{\text{cd}}$, is taken into account. The length $L$, width $W$, thickness $t$, and Youngs' modulus $E$ are also considered. This model is based on Bouwstra's buckled beam model [114]:

$$u = \frac{NL}{EA} + \frac{1}{2}\int_0^L \left(z_0'(x)\right)^2 \, \mathrm{d}x - \frac{1}{2}\int_0^L \left(z'(x)\right)^2 \, \mathrm{d}x, \tag{3.6}$$

Where $u$ is the axial displacement, $N$ is the actual axial force, $z(x) = z \cdot \psi(x)$, $z_0(x) = z_0 \cdot \psi(x)$, and $A$ is the cross-section of the membrane ($A = Wt$). Next, the equation is solved by approximating the deflected shape with $\psi(x) = (1 - \cos(2\pi x/L))/2$. This yields:

$$\frac{u}{L} = \frac{N}{EA} + \left(\frac{\pi z_0}{2L}\right)^2 - \left(\frac{\pi z}{2L}\right)^2, \tag{3.7}$$

Where $z$ is known from the buckling model:

$$z = z_0/(1 + N/N_b), \tag{3.8}$$

with $N_b = 4\pi^2 EI/L^2$ [115], gives:

$$u = \frac{NL}{EA} + \left(\frac{\pi}{2L}\right)^2 \left[1 - \frac{1}{(1 + N/N_b)^2}\right] z_0^2, \tag{3.9}$$

Next, the comb drive force $F_{\text{cd}}$ is based on the axial displacement $u$ and can be calculated by (see Appendix B):

$$F_{\text{cd}} = \frac{A\epsilon_0}{2} \left(\frac{1}{(d_1 - u)^2} - \frac{1}{(d_2 + u)^2}\right) V^2 \tag{3.10}$$

$F_{\text{cd}}$ must balance $N$ and $F_{\text{kcd}}$, such that:

$$F_{\text{cd}} - N - k_{\text{cd}} u = 0 \tag{3.11}$$

Eq. (3.11) can be solved for $N$ by substitution of $u$ from Eq. (3.9) in the force balance from Eq. (3.11). Then substitute $u$ from Eq. (3.9) in Eq. (3.10) to get $F_{\text{cd}}(N)$. Finally, $F_{\text{cd}}(N)$ can be substituted in Eq. (3.11) and solved for $N$. Knowing $N$, $z$ can easily be solved using Eq. (3.8) and $u$ by using Eq. (3.9).

**Dynamics of buckled membranes utilizing Euler-Bernoulli theory**

Knowing the axial displacement $u$ and the out-of-plane deformation $z$ for a particular $V_{\text{cd}}$, a model can be made that predicts $f_0$ given that configuration. The predicted $f_0$ can then be compared with the experimental values to comprehend the dynamics. The dynamics can be calculated with the Euler-Bernoulli theory. First, the strain in the membrane is calculated with:

$$\varepsilon_s \approx \varepsilon_0 + \frac{u}{L} + \frac{1}{2}\left(z'(x)\right)^2 \approx \varepsilon_0 + \frac{u}{L} + \frac{1}{2}\left(\frac{z\pi}{L}\right)^2 \sin^2\left(\frac{2\pi x}{L}\right), \tag{3.12}$$

Next, the total potential energy is calculated with:

$$V = \frac{1}{2} EA \int_0^L \varepsilon_s^2 dx + \frac{1}{2} EI \int_0^L \left(z''(x)\right)^2 dx, \tag{3.13}$$

The first term in Eq. (3.13) describes the stretching of the membrane, and the second term describes the bending energy. By taking the second derivative of Eq. (3.13) the effective stiffness can be calculated:

$$k_{\text{eff}} = \frac{\partial^2 V}{\partial z^2} = \underbrace{2EI\frac{\pi^4}{L^3}}_{\text{BR}} + \underbrace{\frac{EA\,\pi^2}{2L}\left(\varepsilon_0 + \frac{u}{L}\right)}_{\text{IS}} + \underbrace{\frac{9\,\pi^4 z^2}{16L^3}}_{\text{OS}} \tag{3.14}$$

Interestingly, there are three competing terms in Eq. (3.14). The first term accounts for bending rigidity (BR), the second for in-plane stretching (IS), and the last for out-of-plane stretching (OS). Note that $u(V)$ and $z(V)$ are related to the force balance in Eq. (3.11). Finally, the effective mass $m_{\text{eff}}$ can be calculated using the mode shape. Approximating the deflected shape with $\psi(x) = (1 - \cos(2\pi x/L))/2$ this yields [114]:

$$m_{\text{eff}} = m_0 \frac{1}{L} \int_0^L |\varphi(x)|^2 dx = \frac{3}{8} m_0, \tag{3.15}$$

And $f_0$ knowing $k_{\text{eff}}$ and $m_{\text{eff}}$:

$$f_0 = \frac{1}{2\pi}\sqrt{\frac{k_{\text{eff}}}{m_{\text{eff}}}}. \tag{3.16}$$

Additionally, further analysis was carried out to investigate the membrane's stiffness on $N$. For an initial decrease in resonance frequency as observed in Fig. 3.2(d), $\partial k_{\text{eff}}/\partial N$ should be smaller than 0. This expression was evaluated at $\partial k_{\text{eff}}/\partial N = 0$, resulting in (see Appendix C):

$$z_c = \sqrt{4/21}t, \tag{3.17}$$

This implies that when $z > z_c$, an initial decrease in $f_0$ is expected.

### Fitting to the data

To analyze this expression further, the experimental results $f_0(V)$ for devices D3-D6 are fitted using an SQP optimization algorithm on the buckling model. With Young's modulus $E$, pre-deformation $z_0$, and pre-strain $\epsilon_0$ as the fitting parameters. Surprisingly, the model can only find a fit for device D6 (see Fig. 3.5(d)). The fitted values for $E$, $z_0$, and $\epsilon_0$ were 7.4 GPa, 73 nm, and 0.01, respectively. $E$ is relatively low considering the literature value of 103 GPa [111]. Although it is unclear where the readout laser was focused exactly, $z_0$ is within the deformation range observed in Fig. 3.1(d2).

In addition, to investigate the effect of the critical pre-deformation (see Eq. (3.17)) on the dynamics, $z_0$ was varied such that $z_0 = 0$, $0 < z_0 < z_c$, $z_0 = z_c$ and $z_0 > z_c$. Furthermore, for device D3-D5, $\epsilon_0$ was assumed to be 0, and $E$ was gathered from literature (see Table 3.1). In contrast, for D6, the fitted values for $E$ and $\epsilon_0$ were used for all plots ($E = 7.4$ GPa, $\epsilon_0 = 0.01$). Observing the results in Fig. 3.5, it can be seen that $f_0$ increases the fastest from $V_{cd} = 0V$ with increasing $V_{cd}$ when $z_0 = 0$. This increase becomes flatter with increasing $z_0$ until there is a partially flat $f - V$ in a lower frequency bound at $z_0 = z_c$ (see purple plots in Fig. 3.5). Interestingly, when $z_0 > z_c$, an initial decrease in $f_0$ is observed for all devices, similar to the observation in device D6. Furthermore, it is noticeable that the lowest $f_0$ from the model is always greater than the experimental $f_0$ for devices D3-D5. This means that either $k_{\text{eff}}$ is overestimated or $m_{\text{eff}}$ is underestimated or a combination of the two following Eq. (3.16).

Finally, from the plots using the literature value of $E$ in Figs. 3.5(a)-(c) with a chosen $z_0$, it can be seen that in all cases, the estimated $f_0$ at $V_{cd} = 0$ V is always greater than the experimental value. Although differentiation between the individual factors affecting $f_0$ is not possible, this observation could indicate an overestimation of $E$ according to Eqns. (3.14) and (3.16).

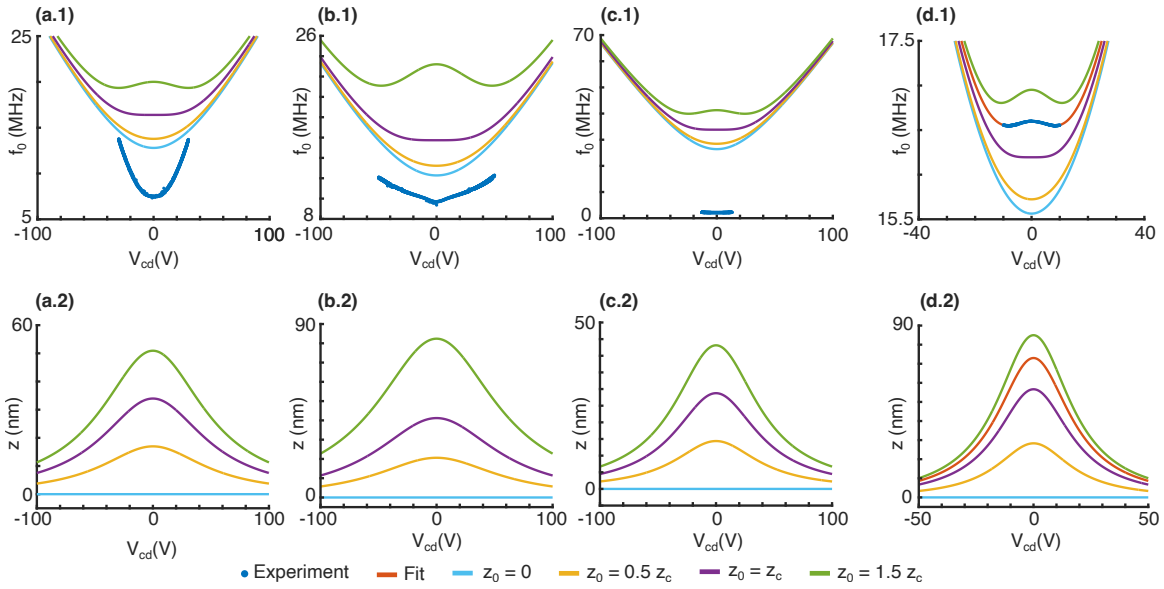


**Figure 3.5:** Dynamics and pre-deformation of devices D3-D6 under MEMS-induced tension. $z_c$ is device specific and determined with Eq. (3.17). Sub-image 1 shows the dynamics versus $V_{cd}$ and includes the experimental data (blue). Sub-image 2 models the pre-deformation versus $V_{cd}$. a) Device D3. b) Device D4. c) Device D5 d) Device D6. Fit: $E = 7.4$ GPa, $\epsilon_0 = 0.01$, $z_0 = 73$ nm)

## 3.3. Discussion

The study investigated the dynamics of 2D material resonators through MEMS-induced tension for material characterization. This study revealed significant influences from pre-deformations like bumps, wrinkles, and buckling [8, 41, 50, 56, 82, 93]. These deformations caused changes in the expected dynamics, leading to distinct behaviors: a slower increase in $f_0$, almost constant $f_0$ within a specific $V_{cd}$ range, or an initial decrease in $f_0$. Conventional models based on bending rigidity and tension failed to explain the observed w-shaped $f_0$ vs. $V$ curve in device D6; therefore, a new model inspired by a buckled beam model was introduced [90, 114, 116].

The developed model uncovered three competing terms governing the membrane's effective stiffness: bending rigidity, in-plane stretching, and out-of-plane stretching. The competition between the in-plane

and out-of-plane stretching during axial displacement $u$ led to interesting behaviors. Above a threshold value $z_c$, the reduction in out-of-plane stiffness outweighed the increase in in-plane stiffness, causing a decrease in $f_0$ until $z_0 = z_c$. In contrast, below $z_c$, an increase in in-plane stiffness dominated, resulting in an increased $f_0$. Notably, within the range of 0 to $z_c$, $f_0$ displayed a slower rate of increase compared to a flat membrane, similar to earlier findings [44]. Device D6, despite being clamped, showed a decrease in $f_0$ at $V_{\text{cd}} = 0$ V, possibly due to shuttle heating inducing an axial displacement and subsequent reduction in $z_0$ and $f_0$, assuming $z_0 > z_c$.

Furthermore, it was also observed that for the devices D3-D5, the estimated $f_0$ was larger than the experimental determined $f_0$. Following Eq. (3.16), either $k_{\text{eff}}$ should have been smaller or $m_{\text{eff}}$ should have been larger, or a combination of the two. Possible explanations for the higher $f_0$ could be (i) An overestimation of $E$, (ii) an overestimation of $t$ due to surface pollution or more layers on the sides compared to the suspended cavity (the AFM measurement was done on the Si-2D membrane interface), (iii) an underestimation of $\rho$ due to surface pollution (possibly from EBID of platinum), or (iv) an underestimation of $L$ due to to the pre-deformation. In addition, the experimental $f_0$ for device D3 increases faster than the model. This could indicate that the effective width of the flake is smaller than the measured width from SEM, which is confirmed by the observations in Figs. 3.1(a2)-(a3).

Analyzing pre-existing deformations using SEM and white light interferometry provided valuable insights. Surprisingly, even with deformations of up to 4 µm in device D5, the SEM failed to reveal these imperfections.

These deformations were also observed to impact the dynamics and material characterization significantly. For example, device D5 could resist repeatable pull-ins, equivalent to straining a flat membrane by over 33%. Moreover, attempting to fit $\sigma/\epsilon$ resulted in anomalously low values for $E$. This poses questions about the reliability of strain and $E$ values reported in the literature, where out-of-plane deformations have been neglected [90, 102]. These images also revealed insights into the strain fields. Notably, device D4 exhibited distinctive upward bulging along its sides under increased potential, indicating localized strain in the center rather than uniform strain across the membrane. Likely contributors to this asymmetry include the transfer process onto the shuttle, wire bonding, and potential misalignment on the shuttle. Suprisingly, Eq. (3.11) couldn't resolve for a positive axial displacement $x$, indicating that $F_{2\text{d}}$ and $F_{\text{kcd}}$ could not be counterbalanced by $F_{\text{cd}}(x)$. This could potentially arise from a larger estimated $F_{2\text{d}}$ value when estimating the force using the full width of the flake in Eq. (3.4). This observation underscores the significance of a uniform stress distribution in 2D material resonators.

Comprehending the pre-deformations in nanomechanical resonators is crucial as they play a vital role in dynamical material characterization. Further studies can investigate how variations like bumps, wrinkles, buckling, or asymmetrical strain fields distinctly affect $f_0$. Additionally, future studies could concentrate on refining fabrication techniques, such as membrane transfer, membrane alignment, and wire bonding, to reduce imperfections and ensure a more uniform stress distribution. Finally, the mathematical models could be simplified by measuring the shuttle displacement $x$. This could be done experimentally with an LCR measurement since the measured inductance can be converted to a displacement. Alternatively, the distance could be measured optically using SEM at the applied voltages $x(V)$. In addition, the height of the pre-deformations at a specific voltage $z(V)$ could be measured using white light interferometry or AFM such that $k_{\text{eff}}$ can be estimated from purely the experimental measurement.

## 3.4. Conclusion

This chapter examines the dynamics of 2D material resonators using MEMS-induced tension to characterize 2D materials dynamically. It revealed imperfections in the topography of the nanomechanical resonators, influencing the dynamics. Conventional models failed to explain a reduction in $f_0$ with axial strain, necessitating a new model based on a buckled beam concept incorporating out-of-plane stiffening. The membrane stiffness is influenced by three factors: bending rigidity, in-plane, and out-of-plane stretching. Interaction between these factors resulted in interesting behaviors for $f_0$, with decreasing $f_0$ above a threshold of $\sqrt{4/21}t$ and increasing $f_0$ below it. The devices were examined using SEM and white light interferometry, which revealed pre-deformations and asymmetrical strain fields. Factors such as membrane transfer and wire bonding could be responsible for this asymmetry. Both mathematical models failed to yield valid values for $E$, whether by assuming that the membranes are flat or buckled. This emphasizes the importance of understanding the imperfections in the topography of 2D material resonators to gain better insights into their dynamics for use in material characterization.

# Chapter 4

# Ultra-sensitive force sensing with 2D material resonators

*This chapter characterizes the sensitivity of 2D material resonant force sensors by accurately probing forces generated by MEMS-induced tension. The extreme precision of these sensors could enable groundbreaking research in biological systems, which often requires sensing at the nano- and picoscale.*

## 4.1. Introduction

This study explores the potential of 2D material resonators as ultra-sensitive force sensors for measuring nN ($10^{-9}$) and pN ($10^{-12}$) forces, potentially outperforming commercially available MEMS-based force sensors with sensitivities of 0.5 µN [96].

These ultra-low sensitivities are significant in gaining a better understanding of the basic components of biological systems [97]. For example, a novel study by Roslon estimated that single-cell bacteria exert a force of up to 6nN [98]. Measurement of these tiny forces would allow for rapid screening of antibiotics. However, most of these studies rely on approximations of the stiffness of circular nano drums and estimate the force of these drums based on their deflection [98], which might be inaccurate due to wrinkles or asymmetrical topography of the membranes.

In this particular study, the MEMS device provides a platform for examining the force sensitivity of different 2D material resonators. Devices D3-D6 that have been manufactured according to the method in Appendix A - S1 can be found in Table 4.1. The purpose of this study is to measure the force sensitivity in a purely mechanical fashion, overcoming approximations and consequently improving reliability. The MEMS offers a platform for calibrating and measuring the force sensitivity of the 2D material resonators.

| Device | $E$ (GPa) | $\sigma_s$ (GPa) | $k_m$ (N/m) | $V_{\max}$ (V) | $F_{\max}$ ($\mu$N) | $\sigma_{\text{avg}}$ (MPa) | $\epsilon_{\text{avg}}$ ($\times 10^{-4}$) | S (pN/Hz) |
|---|---|---|---|---|---|---|---|---|
| D3 | 160 [105] | 16.9 | 41281 | 30 | 42.56 | 27.50 | 1.718 | 6.7 |
| D4 | 150 [109] | 19.91 | 37756 | 60 | 170.25 | 112.73 | 7.515 | 60 |
| D5 | 430 [102] | 25 | 37310 | 12 | 6.81 | 13.08 | 0.304 | 170 |
| D6 | 103 [111] | | 37958 | 12 | 6.81 | 4.49 | 0.435 | -20 |

**Table 4.1:** Sensitivity characterization of 2D material resonant force sensors. Young's modulus $E$, strength $\sigma_s$ adapted from [117], membrane stiffness $k_m$, maximum applied experimental voltage $V_{\max}$, maximum applied force when neglecting the increased capacitance with decreased plate distance $F_{\max} = F_{\text{cd}}(V_{\max}, 0)$, average stress at $F_{\max}$ $\sigma_{\text{avg}}$, average strain at $\sigma_{\text{avg}}$ $\epsilon_{\text{avg}}$, and sensitivity (S).

## 4.2. Extracting stress and strain using a static approach

This section delves into the stress and strain by assuming that the 2D material membranes are in a flat configuration. This will help to understand the potential of these devices as an ultra-sensitive force sensor. Assuming a uniform force distribution, the stress and strain can be approximated. Starting with the in-plane stiffness of the membranes $k_m$:

$$k_m = \frac{Ewt}{L}, \tag{4.1}$$

The values for $k_m$ can be found in Table 4.1. From this table, it can be seen that $k_m$ is much greater than $k_{\text{cd}}$, which was measured experimentally at 38.4 N/m (See Appendix A - S2). Therefore, to approximate the stress in the membranes, the contribution of the counterforce of the comb drive will be neglected ($k_m \gg k_{\text{cd}}$). Furthermore, the force induced by the comb drive can be calculated with (see Appendix B):

$$F_{\text{cd}}(V, x) = \frac{A\epsilon_0}{2}\left(\frac{1}{(d_1 - x)^2} - \frac{1}{(d_2 + x)^2}\right)V^2 \tag{4.2}$$

Where $A$ is the overlapping area between the comb drive fingers ($A$=1.5×10$^{-9}$m$^2$), $\epsilon_0$ is the vacuum permittivity ($\epsilon_0 = 8.854\times10^{-12}Fm^{-1}$), $d_1$ is the distance of the smallest gap ($d_1 = 2$ µm), $d_2$ is the distance of the biggest gap ($d_1 = 4$ µm). When a small displacement is assumed $x \approx 0$, $F_{\text{cd}}$ can be simplified to:

$$F_{\text{cd}}(V, 0) = 4.729\times10^{-8}\,V^2 \tag{4.3}$$

Now, since the contribution of $k_{cd}$ is neglected, the force in the comb drive actuator is approximately the force in the membrane. Therefore, the stress can be approximated:

$$\sigma_{avg} \approx \frac{F_{max}}{wt}, \tag{4.4}$$

Where $F_{max}$ is the force at $F_{cd}(V_{max}, 0)$. Finally, the average strain in the membrane $\epsilon_{avg}$ is:

$$\epsilon_{avg} \approx \frac{\sigma_{avg}}{E}, \tag{4.5}$$

Table 4.1 contains an overview of the derived $\sigma_{avg}$ and $\epsilon_{avg}$ for devices D3-D6. For these formulas, the literature values for $E$ were used, as cited in the table. Note that these values only hold under the conditions that the membranes are flat. It is of interest to compare the results of the dynamical model with the force balance. For device D5, it can be observed that from the dynamics, $\sigma$ and $\epsilon$ was $\approx 0.08$ MPa, and 0.06, respectively. In contrast to the static values found of 13.08 MPa and $0.304 \times 10^{-4}$. The high strain values and the pull-in of device D5 near the MEMS pull-in suggest that the observed stiffness of the membrane was much lower than expected from a flat configuration.

## 4.3. Measuring piconewton forces

2D materials could be used as a new type of resonant force sensor. When a force is applied to the membranes, this changes its pretension. This is similar to tuning a guitar string, which changes in frequency when tuned. This section examines the sensitivity of the membranes when an external force of the comb drive is applied. It is assumed that the membranes are flat, so the effect of $x$ on the comb drive force in the voltage range is negligible (note the low strain values in Table 4.1). Therefore, equation (4.3) estimates the exerted force. Furthermore, the comb drive stiffness is neglected since $k_m \gg k_{cd}$.

Figure 4.1 plots $F_{cd}(V, 0)$ versus the $f - f_{min}$ for devices D3-D6. Where $f_{min}$ is the minimum frequency measured. This shows the sensitivity of the devices based on the exerted force. It can be observed that device D3 is the most sensitive, with a sensitivity of 6.7 pN/Hz (see Fig. 4.1(a)). Device D4 in Fig. 4.1(b) shows the largest force range of about 150 µN; this range could be much higher since this device was not strained to its ultimate limits. It is worth noting that the sensitivity of this device is changing. The device is more sensitive within the 0 to 0.5 MHz range (smaller slope). This was also noticeable in the $f_0$ vs. $V_{cd}$ graph in Fig. 3.2(b). Device D6 shows the opposite sensitivity where the induced force reduces the frequency (see Fig. 4.1(d). Although the comb drive forces were approximated (assuming $x = 0$), these 2D materials show the potential to measure forces very accurately.

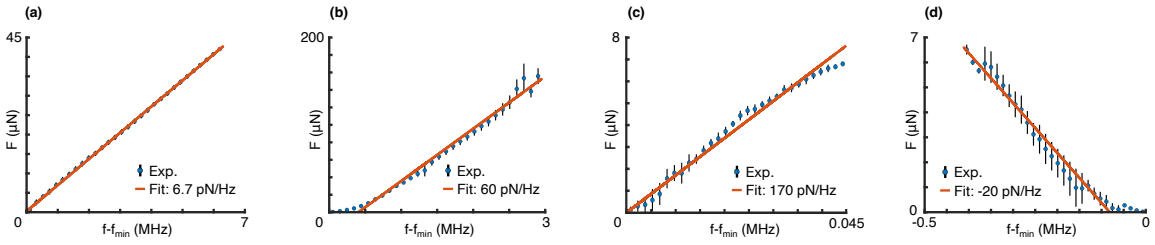


**Figure 4.1:** Approximation of the force $F_{cd}(V, 0)$ versus the change in resonance frequency with the sensitivity fit in pN/Hz. a) Device D3. b) Device D4 c) Device D5 d) Device D6

## 4.4. Discussion

This study explored the potential of 2D material resonators for ultra-sensitive force sensing, potentially surpassing commercially available silicon-based devices. Using a MEMS actuator, the study benchmarked force sensitivity across 2D materials.

In a flat configuration, the stiffness of the flakes (≈40 kN/m) greatly surpassed the comb drive stiffness of 38.42 N/m (see Appendix A - S2). Hence, the comb drive stiffness was neglected. It was assumed that the MEMS shuttle did not move much axially within the experimental voltage range, so the force of the comb drive at zero displacement was approximately equal to the force at

non-zero displacement. For instance, device D4 was assumed to displace 0.75 nm in-plane ($x = \epsilon_{\text{avg}} L$). Neglecting $x$ yielded a force of 170.25 µN ($F_{\text{cd}}(V, 0)$), while including $x = 0.75$ nm resulted in 170.44 µN ($F_{\text{cd}}(V, 0.75\text{nm})$). However, these stiffness calculations significantly exceeded the observations in the experiments. For example, device D5 should have moved only 0.03 nm ($x = \epsilon_{\text{avg}} L$). However, at around 14 V, it exhibited a pull-in, moving 2 µm. This might be the effect of wrinkles as observed in Fig. 3.1(c2), which emphasizes the importance of understanding pre-deformations.

This also shows that the assumption of a flat membrane and thereby neglecting $x$ in the calculation of the comb drive force is not very precise for the devices that show a clear displacement of $x$ such as device D5. Since a reduction in the plate distance of the comb drive actuator, increases the capacitance and thereby the exerted force (see Appendix B). For further studies, it would be advisable to measure the capacitance using an LCR measurement to determine $x$ experimentally thereby increasing the validity of the results.

Comparing the estimated stress values in Table 4.1 with the ultimate tensile strength is of interest. These values are much lower than the ultimate tensile strength, giving them a competitive advantage over Si-based sensors with lower yield strength[118].

The sensitivity of the devices could be improved by making them more responsive to external forces. When neglecting bending rigidity, $f_0$ is proportional to $\sqrt{\sigma}$ (Eq.(3.1)), and the membrane's cross-section determines this tension. Therefore, the sensitivity can be further improved by reducing the cross-section of the devices (see Eq. (4.4)). It would be valuable in future studies to investigate the ultimate sensitivity limit of 2D material resonant force sensors at the monolayer.

The observed variations in sensitivity among the devices in Figure 4.1 can be attributed to several potential factors. These factors include (i) differences in the effective width in contrast to the actual width of the devices, (ii) variations in device height, (iii) differences in surface topography, (iv) potential pre-deformations, (such as a pre-existing 4 µm deformation in device D5), and (v) the occurrence of buckling resulting in a reduction in $f_0$ with respect to the applied force. These factors can significantly impact device sensitivity, leading to diverse performance characteristics.

There are minor variations observable from the sensitivity fit in Fig. 4.1, possibly due to hysteresis or unwrinkling in some devices. This hysteresis can be caused by slipping over the silicon surface before the clamping points [64] since the clamps were placed a few microns before the cavity to avoid contaminating the membranes. Additionally, the accuracy of the $f_0$ measurements may be limited due to the precision of the measurements carried out using the VNA [10]. The bandwidth and number of points were minimized to speed up the measurement process, but this could have decreased accuracy. Focusing on a smaller interval, increasing the number of data points, and reducing the bandwidth are recommended to improve the readout accuracy.

## 4.5. Conclusion

To conclude, this study showed that 2D material resonators have the potential to be ultra-sensitive force sensors that could outperform commercially available silicon-based sensors. For studying the sensitivity, 2D material membranes were dry transferred on a MEMS device that could strain the membrane in a purely mechanical way. This approach reached sensitivities of 6.7 pN/Hz, outperforming the sensitivity of commercially available tension devices by almost two orders of magnitude [96]. In addition, the force range of this commercially available device is ±200 µN [96]. 2D material resonant force sensors could expand this range since their ultimate tensile strength limits their force range. Therefore, 2D material resonant force sensors can outperform Si-based force sensors in both force range and sensitivity.

However, the precision of vibration measurements remains a limiting factor [10]. Therefore, improved readout of the membrane dynamics could overcome these limitations. Also, the sensitivity is affected by pre-deformations such as wrinkles and even buckling which impacts the expected behavior.

Future studies could focus on finding the ultimate sensitivities of these materials, such as the sensitivity of narrow monolayer 2D material membranes. In addition, the tradeoff between sensitivity and force range can be examined. Finally, future studies could improve the readout and the individual effects that play a role in the fluctuations of the resonance frequency, such as heating induced by the measurement.

# Chapter 5

# Conclusion and outlook

*This chapter summarizes the key findings of the thesis, presenting the most important conclusions. Furthermore, it provides an outlook highlighting open research questions, offering promising directions for future studies of 2D resonators.*

## 5.1. Conclusion

This thesis examined the dynamics and dissipation dilution of 2D material resonators under MEMS-induced tension. The study established in situ tuning of 2D material resonators to tune the Q-factor and resonance frequency. The results proved that this tuning aligns with dissipation dilution models for nanomechanical resonators. By adjusting the in-plane tension, it is shown that the Q-factor can be increased by 91% with a simultaneous 30% increase in resonance frequency $f_0$. A dry-transfer technique was used to precisely place membranes on the MEMS device within a 350 µm diameter contact area to enable the experiments.

A clamping technique was developed using EBID to prevent slippage when tuning the 2D material resonators. The clamping method was tested and found to be effective as an unclamped membrane showed a significant permanent loss in $f_0$ in comparison to a clamped 2D material resonator under MEMS-induced tension. Even when a substantially higher force was applied to the clamped 2D material resonator.

Moreover, the dynamics and topography of the 2D material resonators were studied under MEMS-induced tension with the aim of characterizing Young's modulus and understanding pre-deformations. Scanning electron microscopy (SEM) and white light interferometry were used to study the topography of four devices, D3-D6, after fabrication. This revealed the influence of wrinkles, bumps, pre-deformations, and asymmetrical strain fields on the dynamics of the resonators. It was shown that the assumption of a flat membrane is unsuitable for probing the material characteristics from a pre-deformed membrane, particularly in buckling scenarios where the out-of-plane stiffness of the membranes cannot be neglected. Therefore, a new model was developed based on a buckled beam model, incorporating the reduction of out-of-plane stiffening when the membranes were strained in situ. Interestingly, it was found that under the influence of axial strain, $f_0$ of a buckled resonator decreases when the out-of-plane deformation is above $\sqrt{4/21}t$ and increases when it is below it. This revealed the competition between in-plane stiffening and out-of-plane stiffening. Both models could not accurately probe Young's modulus from the dynamics, which is likely due to inaccurate assumptions of the membrane topography leading to inaccurate predictions of the strain in the membrane. This might be overcome by probing the uniaxial displacement of the shuttle experimentally, for example, by an LCR measurement.

It was also shown that 2D material resonators can be used as ultra-sensitive force sensors reaching piconewton sensitivities, surpassing the sub-micron resolution of silicon-based sensors. By in-plane straining the 2D material membranes, sensitivities of 6.7 pN/Hz were achieved, significantly outperforming commercially available tension devices by nearly two orders of magnitude. This paves the way for fundamental research on biological systems, such as the binding forces between molecules ($F$ = 20pN), crucial in understanding tumor progression and tissue formation. In addition, the force range of these tunable 2D material resonators is limited by their ultimate tensile strength, providing a broad force range in comparison with their silicon-based competitors. However, the precision of the readout of the dynamics remains a limiting factor in the resolution.

These findings, along with a better understanding of the impact of pre-deformations, pave the way towards developing higher-Q 2D material resonators that could be used in piconewton force sensing, time-keeping, and information processing, potentially outperforming state-of-the-art SiN devices [118].

## 5.2. Outlook

Experimentally tuning 2D material resonators by MEMS-induced tension has opened up new possibilities for Q-factor tuning and ultra-sensitive force sensing. Additionally, it has revealed the complexity of pre-deformations in dynamic material characterization. It is clear that the experimental research conducted in this thesis represents a small step forward in understanding the complex dynamics of 2D material resonators. The following open research questions provide promising directions for further study:

**Understanding the individual factors contributing to the Q-factor**
The research paper provides evidence of dissipation dilution in nanomechanical resonators. However, the larger picture of all the individual factors contributing to damping and its temperature dependence remains unclear. Various factors such as clamping, thermoelastic dissipation, collisions with gas molecules, surface roughness, and adsorbates on the substrate all contribute to the Q-factor [8, 79]. How

can one quantify these individual factors and determine their dependence on the geometry and material of the resonator?

**Exploring the limits of dissipation dilution in 2D material resonators**
While dissipation dilution has been proved to boost the Q-factor of 2D material resonators by 91%, its Q-factor is still much lower than that of SiN resonators, where Q-factors of over a billion have been reached [118]. SiN resonators are currently limited due to ultimate tensile strength limitations [119]. However, 2D materials may overcome this limitation as they have been found to have higher tensile strength numbers [25]. It's worth noting that this thesis didn't subject 2D materials to their strain limits. Therefore, the question remains: what is the ultimate Q-factor enhancement that can be achieved by dissipation dilution in 2D materials, and can they surpass SiN nanomechanical resonators?

**Improving the material characterization by experimentally measuring the in-plane displacement**
The dynamical models from Section 3 were unable to measure $E$ accurately. This might be caused due to inaccurate estimations of the uniaxial displacement of the shuttle. To make these models more accurate, the uniaxial displacement of the shuttle could be directly measured with an LCR measurement. Can the material characterization using MEMS-induced tension be improved by measuring the uniaxial displacement of the shuttle experimentally?

**Understanding the effect of asymmetric pre-deformations on the Dynamics of 2D resonators**
Bumps, wrinkles, and pre-deformations were observed when examining the membranes using white light interferometry. These irregularities appear to affect the strain fields of the membranes, causing them to be asymmetrical when strained. How are these pre-deformations affecting the dynamics of the membranes and their vibrational mode shapes?

**Optimize the fabrication process to limit imperfections**
Observations have highlighted irregularities like asymmetrical membrane positioning or surface imperfections such as bumps and wrinkles, leading to unexpected behaviors like edges bulging upward during axial straining. Processes like exfoliation, membrane transfer, wire bonding, annealing, and clamping potentially influence the geometry of the membrane. Understanding how each step in this process shapes the final geometry is crucial. What factors contribute to the flake's final topography, and how can the manufacturing process be optimized to minimize imperfections?

**Exploring the effects of width and thickness in the buckling model**
The developed dynamical model based on the concept of a buckled beam is a first step towards a better understanding of pre-deformed resonators. It is worth examining the impact of the width of the membrane, as the flexural rigidity of a beam tends to increase with its width. This is due to the suppression of in-plane dilation accompanying axial strain, making a plate stiffer compared to a beam [116]. How does the width of the flake impact the stiffness of the membrane? What happens in the monolayer limit when the bending rigidity is no longer determined by interlayer interactions but by intra-monolayer interactions [120]?

# Acknowledgements

Even before I started my master's degree, I was fascinated by materials like graphene. It is a material stronger than steel and diamond, flexible, conductive, and even transparent. Although I was unaware of its actual applications at the time, I now see the immense potential of these 2D materials in the fields of fast screening of antibiotics or extremely sensitive sensors. I'm very thankful that I got the opportunity to do fascinating experiments with these materials and get hands-on experience with the most high-tech machines.

I want to express my heartfelt appreciation to my supervisors, who guided me through this journey. I'm very thankful that I could work in such an incredible team. **Gerard**, it was an absolute pleasure working with you throughout this project. You are curious and open-minded and can come up with exceptionally creative and counterintuitive ideas. It is fascinating to see how quickly you can grasp complicated problems, and even more fascinating is when you start solving complex mathematical problems on the whiteboard within a matter of seconds. Your support and dedication have been pivotal to the success of this project, and I'm incredibly thankful. **Peter**, you're a truly creative and inspiring leader. Seeing how you analyze problems from every angle to find the best solutions was very enjoyable. You were irreplaceable at times when I was stuck and needed new ideas or insights. Notable were the simplest toys, like a rubber band or a piece of thin paper, which helped me to unravel the most complicated dynamics. Thanks again for all the inspiring moments and your dedication throughout the project. **Farbod**, your enthusiasm and energy throughout the project have been incredibly enjoyable. You've been a true inspiration, encouraging me to dive deep into the topic of nonlinear dynamics and comprehend the complex behavior in the nonlinear domain. Thanks to you, I've gained the confidence to tackle even the most intricate concepts. I am deeply grateful for your valuable guidance and continued support.

Also a big thanks to: **Niels** For helping me with sample fabrication and measurements, **Donghoon** for your help with the annealing setup and EBID training, **Maurits and Damian** for the training with the wire-bonding machine, **Irek** For your inspiration and initial tests with EBID, **Ze Yu** for your help with AFM, **Alex, Patrick, and Bradley** for all the lab support and training, **Ashwinray** for your help with Lynceetech and everyone else that helped me or inspired me throughout the project.

# References


[1] M. H. Kang *et al.*, "Mechanical robustness of graphene on flexible transparent substrates," *ACS Applied Materials Interfaces*, vol. 8, no. 34, pp. 22 506–22 515, 2016, OA status: green$_{published}$, ISSN: 1944-8244.

[2] H. Tomori *et al.*, "Introducing nonuniform strain to graphene using dielectric nanopillars," *Applied Physics Express*, vol. 4, no. 7, p. 075 102, 2011, ISSN: 1882-0778.

[3] P. L. De Andres and J. A. Vergés, "First-principles calculation of the effect of stress on the chemical activity of graphene," *Applied Physics Letters*, vol. 93, no. 17, p. 171 915, 2008, ISSN: 0003-6951.

[4] M. Yang, A. Nurbawono, C. Zhang, R. Wu, Y. Feng, and Ariando, "Manipulating absorption and diffusion of h atom on graphene by mechanical strain," *AIP Advances*, vol. 1, no. 3, p. 032 109, 2011, ISSN: 2158-3226.

[5] T. Low and F. Guinea, "Strain-induced pseudomagnetic field for novel graphene electronics," *Nano Letters*, vol. 10, no. 9, pp. 3551–3554, 2010, ISSN: 1530-6984.

[6] M. C. Rechtsman, J. M. Zeuner, A. Tünnermann, S. Nolte, M. Segev, and A. Szameit, "Strain-induced pseudomagnetic field and photonic landau levels in dielectric structures," *Nature Photonics*, vol. 7, no. 2, pp. 153–158, 2013, ISSN: 1749-4885.

[7] C. Lee, X. Wei, J. W. Kysar, and J. Hone, "Measurement of the elastic properties and intrinsic strength of monolayer graphene," *Science*, vol. 321, no. 5887, pp. 385–388, 2008, doi: 10.1126/science.1157996.

[8] P. G. Steeneken, R. J. Dolleman, D. Davidovikj, F. Alijani, and H. S. J. van der Zant, "Dynamics of 2d material membranes," *2D Materials*, vol. 8, no. 4, 2021, ISSN: 2053-1583.

[9] B. Lassagne, D. Garcia-Sanchez, A. Aguasca, and A. Bachtold, "Ultrasensitive mass sensing with a nanotube electromechanical resonator," *Nano Letters*, vol. 8, no. 11, pp. 3735–3738, 2008, ISSN: 1530-6984.

[10] P. Weber, J. Guttinger, A. Noury, J. Vergara-Cruz, and A. Bachtold, "Force sensitivity of multilayer graphene optomechanical devices," *Nat Commun*, vol. 7, p. 12 496, 2016, Weber, P Guttinger, J Noury, A Vergara-Cruz, J Bachtold, A eng European Research Council/International Research Support, Non-U.S. Gov't England 2016/08/10 Nat Commun. 2016 Aug 9;7:12496. doi: 10.1038/ncomms12496., ISSN: 2041-1723 (Electronic) 2041-1723 (Linking).

[11] A. Sakhaee-Pour, M. T. Ahmadian, and A. Vafai, "Applications of single-layered graphene sheets as mass sensors and atomistic dust detectors," *Solid State Communications*, vol. 145, no. 4, pp. 168–172, 2008, ISSN: 0038-1098.

[12] J. Atalaya, J. M. Kinaret, and A. Isacsson, "Nanomechanical mass measurement using nonlinear response of a graphene membrane," *Europhysics Letters*, vol. 91, no. 4, p. 48 001, 2010, ISSN: 0295-5075.

[13] V. Singh *et al.*, "Probing thermal expansion of graphene and modal dispersion at low-temperature using graphene nanoelectromechanical systems resonators," *Nanotechnology*, vol. 21, no. 16, p. 165 204, 2010, Singh, Vibhor Sengupta, Shamashis Solanki, Hari S Dhall, Rohan Allain, Adrien Dhara, Sajal Pant, Prita Deshmukh, Mandar M eng Research Support, Non-U.S. Gov't England 2010/03/31 Nanotechnology. 2010 Apr 23;21(16):165204. doi: 10.1088/0957-4484/21/16/165204. Epub 2010 Mar 30., ISSN: 1361-6528 (Electronic) 0957-4484 (Linking).

[14] R. J. Dolleman, P. Belardinelli, S. Houri, H. S. J. Van Der Zant, F. Alijani, and P. G. Steeneken, "High-frequency stochastic switching of graphene resonators near room temperature," *Nano Letters*, vol. 19, no. 2, pp. 1282–1288, 2019, ISSN: 1530-6984.

[15] M. C. Lemme *et al.*, "Nanoelectromechanical sensors based on suspended 2d materials," *Research (Wash D C)*, vol. 2020, p. 8 748 602, 2020, Lemme, Max C Wagner, Stefan Lee, Kangho Fan, Xuge Verbiest, Gerard J Wittmann, Sebastian Lukas, Sebastian Dolleman, Robin J Niklaus, Frank van der Zant, Herre S J Duesberg, Georg S Steeneken, Peter G eng Review 2020/08/09 Research (Wash D C). 2020 Jul 20;2020:8748602. doi: 10.34133/2020/8748602. eCollection 2020., ISSN: 2639-5274 (Electronic) 2639-5274 (Linking).

[16] J. Romijn *et al.*, "A miniaturized low power pirani pressure sensor based on suspended graphene," in *2018 IEEE 13th Annual International Conference on Nano/Micro Engineered and Molecular Systems (NEMS)*, IEEE, 2018.

[17] R. J. Dolleman, D. Davidovikj, S. J. Cartamil-Bueno, H. S. J. Van Der Zant, and P. G. Steeneken, "Graphene squeeze-film pressure sensors," *Nano Letters*, vol. 16, no. 1, pp. 568–571, 2016, ISSN: 1530-6984.

[18] D. Shahdeo, A. Roberts, N. Abbineni, and S. Gandhi, "Graphene based sensors," in *Analytical Applications of Graphene for Comprehensive Analytical Chemistry* (Comprehensive Analytical Chemistry), Comprehensive Analytical Chemistry. 2020, pp. 175–199, ISBN: 9780323853712.

[19] J. H. Choi, J. Lee, M. Byeon, T. E. Hong, H. Park, and C. Y. Lee, "Graphene-based gas sensors with high sensitivity and minimal sensor-to-sensor variation," *ACS Applied Nano Materials*, vol. 3, no. 3, pp. 2257–2265, 2020, ISSN: 2574-0970.

[20] I. E. Rosłoń *et al.*, "High-frequency gas effusion through nanopores in suspended graphene," *Nature Communications*, vol. 11, no. 1, 2020, ISSN: 2041-1723.

[21] J.-H. Lee, S.-J. Park, and J.-W. Choi, "Electrical property of graphene and its application to electrochemical biosensing," *Nanomaterials*, vol. 9, no. 2, p. 297, 2019, ISSN: 2079-4991.

[22] Y. Song, Y. Luo, C. Zhu, H. Li, D. Du, and Y. Lin, "Recent advances in electrochemical biosensors based on graphene two-dimensional nanomaterials," *Biosensors and Bioelectronics*, vol. 76, pp. 195–212, 2016, ISSN: 0956-5663.

[23] G. P. Veronese *et al.*, "Graphene as transparent conducting layer for high temperature thin film device applications," *Solar Energy Materials and Solar Cells*, vol. 138, pp. 35–40, 2015, ISSN: 0927-0248.

[24] A. Castellanos-Gomez, V. Singh, H. S. J. van der Zant, and G. A. Steele, "Mechanics of freely-suspended ultrathin layered materials," *Annalen der Physik*, vol. 527, no. 1-2, pp. 27–44, 2015, https://doi.org/10.1002/andp.201400153, ISSN: 0003-3804.

[25] M. Goldsche *et al.*, "Tailoring mechanically tunable strain fields in graphene," *Nano Letters*, vol. 18, no. 3, pp. 1707–1713, 2018, OA status: $\text{green}_{p}ublished$, ISSN: 1530-6984.

[26] Z. J. Su *et al.*, "Tunable parametric amplification of a graphene nanomechanical resonator in the nonlinear regime," *Nanotechnology*, vol. 32, no. 15, p. 155 203, 2021, Su, Zi-Jia Ying, Yue Song, Xiang-Xiang Zhang, Zhuo-Zhi Zhang, Qing-Hang Cao, Gang Li, Hai-Ou Guo, Guang-Can Guo, Guo-Ping eng England 2020/11/13 Nanotechnology. 2021 Apr 9;32(15):155203. doi: 10.1088/1361-6528/abc9ea., ISSN: 1361-6528 (Electronic) 0957-4484 (Linking).

[27] G. J. Verbiest *et al.*, "Tunable coupling of two mechanical resonators by a graphene membrane," *2D Materials*, vol. 8, no. 3, p. 035 039, 2021, ISSN: 2053-1583.

[28] P. G. Steeneken, T. G. S. M. Rijks, J. T. M. V. Beek, M. J. E. Ulenaers, J. D. Coster, and R. Puers, "Dynamics and squeeze film gas damping of a capacitive rf mems switch," *Journal of Micromechanics and Microengineering*, vol. 15, no. 1, pp. 176–184, 2005, ISSN: 0960-1317.

[29] X. Rottenberg, I. De Wolf, B. Nauwelaers, W. De Raedt, and H. Tilmans, "Analytical model of the dc actuation of electrostatic mems devices with distributed dielectric charging and nonplanar electrodes," *Journal of Microelectromechanical Systems*, vol. 16, no. 5, pp. 1243–1253, 2007, ISSN: 1057-7157.

[30] E. M. Chudnovsky and R. Zarzuela, "Stability of suspended graphene under casimir force," *Physical Review B*, vol. 94, no. 8, 2016, ISSN: 2469-9950.

[31] D. Davidovikj, J. J. Slim, S. J. Cartamil-Bueno, H. S. J. Van Der Zant, P. G. Steeneken, and W. J. Venstra, "Visualizing the motion of graphene nanodrums," *Nano Letters*, vol. 16, no. 4, pp. 2768–2773, 2016, ISSN: 1530-6984.

[32] J. Xia, F. Chen, J. Li, and N. Tao, "Measurement of the quantum capacitance of graphene," *Nature Nanotechnology*, vol. 4, no. 8, pp. 505–509, 2009, ISSN: 1748-3387.

[33] R. A. Barton *et al.*, "Photothermal self-oscillation and laser cooling of graphene optomechanical systems," *Nano Letters*, vol. 12, no. 9, pp. 4681–4686, 2012, ISSN: 1530-6984.

[34] J.-J. Suo *et al.*, "Tuning the nonlinearity of graphene mechanical resonators by joule heating," *Journal of Physics: Condensed Matter*, vol. 34, no. 37, p. 374 004, 2022, ISSN: 0953-8984.

[35] D. Davidovikj, M. Poot, S. J. Cartamil-Bueno, H. S. J. Van Der Zant, and P. G. Steeneken, "On-chip heaters for tension tuning of graphene nanodrums," *Nano Letters*, vol. 18, no. 5, pp. 2852–2858, 2018, ISSN: 1530-6984.

[36] R. J. Dolleman, G. J. Verbiest, Y. M. Blanter, H. S. J. Van Der Zant, and P. G. Steeneken, "Nonequilibrium thermodynamics of acoustic phonons in suspended graphene," *Physical Review Research*, vol. 2, no. 1, 2020, ISSN: 2643-1564.

[37] F.-T. Shi, S.-C. Fan, C. Li, and Z.-A. Li, "Opto-thermally excited fabry-perot resonance frequency behaviors of clamped circular graphene membrane," *Nanomaterials*, vol. 9, no. 4, p. 563, 2019, ISSN: 2079-4991.

[38] R. Singh, R. J. Nicholl, K. I. Bolotin, and S. Ghosh, "Motion transduction with thermo-mechanically squeezed graphene resonator modes," *Nano Letters*, vol. 18, no. 11, pp. 6719–6724, 2018, ISSN: 1530-6984.

[39] G. J. Verbiest, J. N. Kirchhof, J. Sonntag, M. Goldsche, T. Khodkov, and C. Stampfer, "Detecting ultrasound vibrations with graphene resonators," *Nano Letters*, vol. 18, no. 8, pp. 5132–5137, 2018, ISSN: 1530-6984.

[40] D. H. Zanette, "Energy exchange between coupled mechanical oscillators: Linear regimes," *Journal of Physics Communications*, vol. 2, no. 9, p. 095 015, 2018, ISSN: 2399-6528.

[41] C. Di Giorgio, E. Blundo, G. Pettinari, M. Felici, F. Bobba, and A. Polimeni, "Mechanical, elastic, and adhesive properties of two-dimensional materials: From straining techniques to state-of-the-art local probe measurements," *Advanced Materials Interfaces*, vol. 9, no. 13, p. 2 102 220, 2022, ISSN: 2196-7350.

[42] T. Mashoff *et al.*, "Bistability and oscillatory motion of natural nanomembranes appearing within monolayer graphene on silicon dioxide," *Nano Letters*, vol. 10, no. 2, pp. 461–465, 2010, ISSN: 1530-6984.

[43] H. H. Perez-Garza, E. W. Kievit, G. F. Schneider, and U. Staufer, "Highly strained graphene samples of varying thickness and comparison of their behaviour," *Nanotechnology*, vol. 25, no. 46, p. 465 708, 2014, Perez-Garza, Hector Hugo Kievit, Eric Walter Schneider, Gregory F Staufer, Urs eng Research Support, Non-U.S. Gov't England 2014/11/02 Nanotechnology. 2014 Nov 21;25(46):465708. doi: 10.1088/0957-4484/25/46/465708. Epub 2014 Oct 31., ISSN: 1361-6528 (Electronic) 0957-4484 (Linking).

[44] Y. Xie, J. Lee, Y. Wang, and P. X.-L. Feng, "Nanoelectromechanical systems: Straining and tuning atomic layer nanoelectromechanical resonators via comb-drive mems actuators (adv. mater. technol. 2/2021)," *Advanced Materials Technologies*, vol. 6, no. 2, p. 2 170 008, 2021, ISSN: 2365-709X.

[45] M. Goldsche *et al.*, "Fabrication of comb-drive actuators for straining nanostructured suspended graphene," *Nanotechnology*, vol. 29, no. 37, p. 375 301, 2018, ISSN: 0957-4484.

[46] M. Goldsche *et al.*, "Low-temperature compatible electrostatic comb-drive actuators with integrated graphene," in *The 9th IEEE International Conference on Nano/Micro Engineered and Molecular Systems (NEMS)*, IEEE.

[47] J. S. Bunch *et al.*, "Impermeable atomic membranes from graphene sheets," *Nano Lett*, vol. 8, no. 8, pp. 2458–62, 2008, Bunch, J Scott Verbridge, Scott S Alden, Jonathan S van der Zande, Arend M Parpia, Jeevak M Craighead, Harold G McEuen, Paul L eng Research Support, Non-U.S. Gov't Research Support, U.S. Gov't, Non-P.H.S. 2008/07/18 Nano Lett. 2008 Aug;8(8):2458-62. doi: 10.1021/nl801457b. Epub 2008 Jul 17., ISSN: 1530-6984 (Print) 1530-6984 (Linking).

[48] J. Sonntag *et al.*, "Engineering tunable strain fields in suspended graphene by microelectromechanical systems," in *2019 20th International Conference on Solid-State Sensors, Actuators and Microsystems Eurosensors XXXIII (TRANSDUCERS EUROSENSORS XXXIII)*, IEEE.

[49] N. Bouman, "Tuning of graphene dynamics by mechanical strain," Thesis, 2023.

[50] F. Guan, P. Kumaravadivel, D. V. Averin, and X. Du, "Tuning strain in flexible graphene nanoelectromechanical resonators," *Applied Physics Letters*, vol. 107, no. 19, p. 193 102, 2015, ISSN: 0003-6951.

[51] J. S. Bunch *et al.*, "Electromechanical resonators from graphene sheets," *Science*, vol. 315, no. 5811, pp. 490–493, 2007, doi: 10.1126/science.1136836.

[52] D. Garcia-Sanchez, A. M. Van Der Zande, A. S. Paulo, B. Lassagne, P. L. Mceuen, and A. Bachtold, "Imaging mechanical vibrations in suspended graphene sheets," *Nano Letters*, vol. 8, no. 5, pp. 1399–1403, 2008, ISSN: 1530-6984.

[53] Y. Xu *et al.*, "Radio frequency electrical transduction of graphene mechanical resonators," *Applied Physics Letters*, vol. 97, no. 24, p. 243 111, 2010, ISSN: 0003-6951.

[54] C. Chen *et al.*, "Performance of monolayer graphene nanomechanical resonators with electrical readout," *Nature Nanotechnology*, vol. 4, no. 12, pp. 861–867, 2009, ISSN: 1748-3387.

[55] A. Eichler, J. Moser, J. Chaste, M. Zdrojek, I. Wilson-Rae, and A. Bachtold, "Nonlinear damping in mechanical resonators made from carbon nanotubes and graphene," *Nature Nanotechnology*, vol. 6, no. 6, pp. 339–342, 2011, ISSN: 1748-3387.

[56] X. Song, M. Oksanen, M. A. Sillanpää, H. G. Craighead, J. M. Parpia, and P. J. Hakonen, "Stamp transferred suspended graphene mechanical resonators for radio frequency electrical readout," *Nano Letters*, vol. 12, no. 1, pp. 198–202, 2012, ISSN: 1530-6984.

[57] V. Singh, S. J. Bosman, B. H. Schneider, Y. M. Blanter, A. Castellanos-Gomez, and G. A. Steele, "Optomechanical coupling between a multilayer graphene mechanical resonator and a superconducting microwave cavity," *Nature Nanotechnology*, vol. 9, no. 10, pp. 820–824, 2014, ISSN: 1748-3387.

[58] P. Weber, J. Güttinger, I. Tsioutsios, D. E. Chang, and A. Bachtold, "Coupling graphene mechanical resonators to superconducting microwave cavities," *Nano Letters*, vol. 14, no. 5, pp. 2854–2860, 2014, ISSN: 1530-6984.

[59] A. M. V. D. Zande *et al.*, "Large-scale arrays of single-layer graphene resonators," *Nano Letters*, vol. 10, no. 12, pp. 4869–4873, 2010, ISSN: 1530-6984.

[60] C. Chen *et al.*, "Graphene mechanical oscillators with tunable frequency," *Nature Nanotechnology*, vol. 8, no. 12, pp. 923–927, 2013, ISSN: 1748-3387.

[61] S. Lee *et al.*, "Electrically integrated su-8 clamped graphene drum resonators for strain engineering," *Applied Physics Letters*, vol. 102, no. 15, p. 153 101, 2013, ISSN: 0003-6951.

[62] J. Güttinger *et al.*, "Energy-dependent path of dissipation in nanomechanical resonators," *Nature Nanotechnology*, vol. 12, no. 7, pp. 631–636, 2017, OA status: green$_p ublished$, ISSN: 1748-3387.

[63] M. M. Parmar, P. R. Y. Gangavarapu, and A. K. Naik, "Dynamic range tuning of graphene nanoresonators," *Applied Physics Letters*, vol. 107, no. 11, p. 113 108, 2015, ISSN: 0003-6951.

[64] Y. Ying, Z.-Z. Zhang, J. Moser, Z.-J. Su, X.-X. Song, and G.-P. Guo, "Sliding nanomechanical resonators," *Nature Communications*, vol. 13, no. 1, 2022, ISSN: 2041-1723.

[65] X. Song, M. Oksanen, J. Li, P. J. Hakonen, and M. A. Sillanpää, "Graphene optomechanics realized at microwave frequencies," *Physical Review Letters*, vol. 113, no. 2, 2014, ISSN: 0031-9007.

[66] S. S. Verbridge, D. F. Shapiro, H. G. Craighead, and J. M. Parpia, "Macroscopic tuning of nanomechanics: substrate bending for reversible control of frequency and quality factor of nanostring resonators," *Nano Letters*, vol. 7, no. 6, pp. 1728–1735, 2007, ISSN: 1530-6984.

[67] A. Keşkekler, H. Arjmandi-Tash, P. G. Steeneken, and F. Alijani, "Symmetry-breaking-induced frequency combs in graphene resonators," *Nano Letters*, vol. 22, no. 15, pp. 6048–6054, 2022, ISSN: 1530-6984.

[68] S. Shivaraman *et al.*, "Free-standing epitaxial graphene," *Nano Letters*, vol. 9, no. 9, pp. 3100–3105, 2009, ISSN: 1530-6984.

[69] R. A. Barton *et al.*, "High, size-dependent quality factor in an array of graphene mechanical resonators," *Nano Letters*, vol. 11, no. 3, pp. 1232–1236, 2011, ISSN: 1530-6984.

[70] B. Alemán *et al.*, "Polymer-free, low tension graphene mechanical resonators," *physica status solidi (RRL) - Rapid Research Letters*, vol. 7, no. 12, pp. 1064–1066, 2013, ISSN: 1862-6254.

[71] A. Chandrashekar, "Optothermally excited parametric resonance in monolayer graphene nanodrum resonators," Thesis, 2017.

[72] R. J. Dolleman, S. Houri, A. Chandrashekar, F. Alijani, H. S. J. Van Der Zant, and P. G. Steeneken, "Opto-thermally excited multimode parametric resonance in graphene membranes," *Scientific Reports*, vol. 8, no. 1, 2018, ISSN: 2045-2322.

[73] S. Houri, S. J. Cartamil-Bueno, M. Poot, P. G. Steeneken, H. S. J. Van Der Zant, and W. J. Venstra, "Direct and parametric synchronization of a graphene self-oscillator," *Applied Physics Letters*, vol. 110, no. 7, p. 073 103, 2017, ISSN: 0003-6951.

[74] A. Keşkekler, O. Shoshani, M. Lee, H. S. J. Van Der Zant, P. G. Steeneken, and F. Alijani, "Tuning nonlinear damping in graphene nanoresonators by parametric–direct internal resonance," *Nature Communications*, vol. 12, no. 1, 2021, ISSN: 2041-1723.

[75] M. Takamura, K. Furukawa, H. Okamoto, S. Tanabe, H. Yamaguchi, and H. Hibino, "Epitaxial trilayer graphene mechanical resonators obtained by electrochemical etching combined with hydrogen intercalation," *Japanese Journal of Applied Physics*, vol. 52, no. 4S, 04CH01, 2013, ISSN: 0021-4922.

[76] H. H. Pérez Garza, E. W. Kievit, G. F. Schneider, and U. Staufer, "Controlled, reversible, and nondestructive generation of uniaxial extreme strains (>10%) in graphene," *Nano Letters*, vol. 14, no. 7, pp. 4107–4113, 2014, ISSN: 1530-6984.

[77] K. Yue, W. Gao, R. Huang, and K. M. Liechti, "Analytical methods for the mechanics of graphene bubbles," *Journal of Applied Physics*, vol. 112, no. 8, p. 083 512, 2012, ISSN: 0021-8979.

[78] F. Ye, J. Lee, and P. X.-L. Feng, "Electrothermally tunable graphene resonators operating at very high temperature up to 1200 k," *Nano Letters*, vol. 18, no. 3, pp. 1678–1685, 2018, ISSN: 1530-6984.

[79] J. M. L. Miller *et al.*, "Effective quality factor tuning mechanisms in micromechanical resonators," *Applied Physics Reviews*, vol. 5, no. 4, p. 041 307, 2018, OA status: $\text{gold}_{other}$, ISSN: 1931-9401.

[80] M. Amabili, *Nonlinear Mechanics of Shells and Plates in Composite, Soft and Biological Materials*. Cambridge University Press, 2018.

[81] M.-H. Bao, "Chapter 2 - basic mechanics of beam and diaphragm structures," in *Micro Mechanical Transducers*, ser. Handbook of Sensors and Actuators, M.-H. Bao, Ed., vol. 8, Elsevier Science B.V., 2000, pp. 23–88.

[82] C. Backes *et al.*, "Production and processing of graphene and related materials," *2D Materials*, vol. 7, p. 022 001, 2020.

[83] M. Lee *et al.*, "Sealing graphene nanodrums," *Nano Lett*, vol. 19, no. 8, pp. 5313–5318, 2019, Lee, Martin Davidovikj, Dejan Sajadi, Banafsheh Siskins, Makars Alijani, Farbod van der Zant, Herre S J Steeneken, Peter G eng 2019/07/25 Nano Lett. 2019 Aug 14;19(8):5313-5318. doi: 10.1021/acs.nanolett.9b01770. Epub 2019 Jul 29., ISSN: 1530-6992 (Electronic) 1530-6984 (Print) 1530-6984 (Linking).

[84] M. Géradin and D. Rixen, *Mechanical vibrations: theory and application to structural dynamics*, 3rd. Wiley, 2015.

[85] A. H. Nayfeh and D. T. Mook, *Nonlinear oscillations* (Wiley classics library), 2nd. New York: Wiley, 1995, [Main author] xiv, 704 p. ill. 23 cm Includes bibliographical references and index, ISBN: 0471121428.

[86] D. Davidovikj, F. Alijani, S. J. Cartamil-Bueno, H. S. J. Van Der Zant, M. Amabili, and P. G. Steeneken, "Nonlinear dynamic characterization of two-dimensional materials," *Nature Communications*, vol. 8, no. 1, 2017, ISSN: 2041-1723.

[87] M. Narayanan, S. Narayanan, and C. Padmanabhan, "Parametric identification of a nonlinear system using multi-harmonic excitation," *Advances in Vibration Engineering*, vol. 7, 2008.

[88] N. Inomata, K. Saito, and T. Ono, "Q factor enhancement of si resonator by nonlinear damping," *Microsystem Technologies*, vol. 23, no. 5, pp. 1201–1205, 2017, ISSN: 0946-7076.

[89] R. Lifshitz and M. C. Cross, *Nonlinear Dynamics of Nanosystems*. Wiley-VCH, 2010.

[90] I. W. Frank, D. M. Tanenbaum, A. M. Van Der Zande, and P. L. Mceuen, "Mechanical properties of suspended graphene sheets," *Journal of Vacuum Science Technology B: Microelectronics and Nanometer Structures*, vol. 25, no. 6, p. 2558, 2007, ISSN: 1071-1023.

[91] A. C. Ferrari and D. M. Basko, "Raman spectroscopy as a versatile tool for studying the properties of graphene," *Nature Nanotechnology*, vol. 8, no. 4, pp. 235–246, 2013, ISSN: 1748-3387.

[92] M. Poot and H. S. J. Van Der Zant, "Nanomechanical properties of few-layer graphene membranes," *Applied Physics Letters*, vol. 92, no. 6, p. 063 111, 2008, OA status: green$_{p}ublished$, ISSN: 0003-6951.

[93] R. J. Nicholl *et al.*, "The effect of intrinsic crumpling on the mechanics of free-standing graphene," *Nature Communications*, vol. 6, no. 1, p. 8789, 2015, OA status: green$_{p}ublished$, ISSN: 2041-1723.

[94] B. Sajadi, F. Alijani, D. Davidovikj, J. ( Goosen, P. G. Steeneken, and F. Van Keulen, "Experimental characterization of graphene by electrostatic resonance frequency tuning," *Journal of Applied Physics*, vol. 122, no. 23, p. 234 302, 2017, OA status: green$_{p}ublished$, ISSN: 0021-8979.

[95] R. J. T. Nicholl, N. V. Lavrik, I. Vlassiouk, B. R. Srijanto, and K. I. Bolotin, "Hidden area and mechanical nonlinearities in freestanding graphene," *Physical Review Letters*, vol. 118, no. 26, 2017, ISSN: 0031-9007.

[96] FEMTOTOOLS, *Ft-s microforce sensing probe*, Web Page, 2023. [Online]. Available: `https://www.femtotools.com/products/ft-nmt04/accessories/ft-s-microforce-sensing-probe`.

[97] Y. Sun and B. J. Nelson, "Mems capacitive force sensors for cellular and flight biomechanics," *Biomedical Materials*, vol. 2, no. 1, S16–S22, 2007, ISSN: 1748-6041.

[98] I. E. Rosłoń, A. Japaridze, P. G. Steeneken, C. Dekker, and F. Alijani, "Probing nanomotion of single bacteria with graphene drums," *Nature Nanotechnology*, vol. 17, no. 6, pp. 637–642, 2022, ISSN: 1748-3387.

[99] A. J. Engler, S. Sen, H. L. Sweeney, and D. E. Discher, "Matrix elasticity directs stem cell lineage specification," *Cell*, vol. 126, no. 4, pp. 677–689, 2006, OA status: bronze, ISSN: 0092-8674.

[100] M. J. Paszek *et al.*, "Tensional homeostasis and the malignant phenotype," *Cancer Cell*, vol. 8, no. 3, pp. 241–254, 2005, OA status: bronze, ISSN: 1535-6108.

[101] B. Kav, T. R. Weikl, and E. Schneck, "Measuring pico-newton forces with lipid anchors as force sensors in molecular dynamics simulations," *The Journal of Physical Chemistry B*, vol. 127, no. 18, pp. 4081–4089, 2023, ISSN: 1520-6106.

[102] M. Annamalai, S. Mathew, M. Jamali, D. Zhan, and M. Palaniapan, "Elastic and nonlinear response of nanomechanical graphene devices," *Journal of Micromechanics and Microengineering*, vol. 22, no. 10, p. 105 024, 2012, ISSN: 0960-1317.

[103] F. Traversi *et al.*, "Elastic properties of graphene suspended on a polymer substrate by e-beam exposure," *New Journal of Physics*, vol. 12, no. 2, p. 023 034, 2010, ISSN: 1367-2630.

[104] S. S. Verbridge, J. M. Parpia, R. B. Reichenbach, L. M. Bellan, and H. G. Craighead, "High quality factor resonance at room temperature with nanostrings under high tensile stress," *Journal of Applied Physics*, vol. 99, p. 124 304, 2006.

[105] S. Bertolazzi, J. Brivio, and A. Kis, "Stretching and breaking of ultrathin mos<sub>2</sub>," *ACS Nano*, vol. 5, no. 12, pp. 9703–9709, 2011, ISSN: 1936-0851.

[106] R. C. Cooper, C. Lee, C. A. Marianetti, X. Wei, J. Hone, and J. W. Kysar, "Nonlinear elastic behavior of two-dimensional molybdenum disulfide," *Physical Review B*, vol. 87, no. 3, 2013, ISSN: 1098-0121.

[107] E. S. Z. Mah, "Charge-induced actuation of two-dimensional (2d) niobium based transition-metal dichalcogenides: A first-principles study," Thesis, 2022.

[108] M. Eagleson, H.-D. Jakubke, and H. Jeschkeit, "Concise encyclopedia chemistry," *(No Title)*, 1994.

[109] I. Kaplan-Ashiri, S. Cohen, K. Gartsman, R. Rosentsveig, G. Seifert, and R. Tenne, "Mechanical behavior of individual ws<sub>2</sub> nanotubes," *Journal of Materials Research*, vol. 19, no. 2, pp. 454–459, 2004, ISSN: 0884-2914.

[110] Y. Liao, Z. Li, and W. Xia, "Size-dependent structural behaviors of crumpled graphene sheets," *Carbon*, vol. 174, pp. 148–157, 2021, ISSN: 0008-6223.

[111] M. Šiškins *et al.*, "Magnetic and electronic phase transitions probed by nanomechanical resonators," *Nature Communications*, vol. 11, no. 1, 2020, ISSN: 2041-1723.

[112] S. J. Cartamil-Bueno, M. Cavalieri, R. Wang, S. Houri, S. Hofmann, and H. S. J. Van Der Zant, "Mechanical characterization and cleaning of cvd single-layer h-bn resonators," *npj 2D Materials and Applications*, vol. 1, no. 1, 2017, OA status: gold$_{a}oaj$, ISSN: 2397-7132.

[113] H. Liu, G. Baglioni, C. B. Constant, H. S. J. v. d. Zant, P. G. Steeneken, and G. J. Verbiest, "Enhanced photothermal response near the buckling bifurcation in 2d nanomechanical resonators," 2023, 69.9 and 93.1 GPa.

[114] S. Bouwstra and B. Geijselaers, "On the resonance frequencies of microbridges," in *TRANSDUCERS '91: 1991 International Conference on Solid-State Sensors and Actuators. Digest of Technical Papers*, IEEE.

[115] C. Kim and S. Dickinson, "The flexural vibration of slightly curved slender beams subject to axial end displacement," *Journal of Sound Vibration*, vol. 104, no. 1, pp. 170–175, 1986, ISSN: 0022-460X.

[116] S. Schmid, *Fundamentals of Nanomechanical Resonators*. 2016.

[117] J. H. Kim, J. H. Jeong, N. Kim, R. Joshi, and G.-H. Lee, "Mechanical properties of two-dimensional materials and their applications," *Journal of Physics D: Applied Physics*, vol. 52, no. 8, p. 083 001, 2019, ISSN: 0022-3727.

[118] D. Shin, A. Cupertino, M. H. J. de Jong, P. G. Steeneken, M. A. Bessa, and R. A. Norte, "Spiderweb nanomechanical resonators via bayesian optimization: Inspired by nature and guided by machine learning," *Advanced Materials*, vol. 34, no. 3, p. 2 106 248, 2022, ISSN: 0935-9648.

[119] M. Xu *et al.*, "High-strength amorphous silicon carbide for nanomechanics," *Advanced Materials*, 2023, ISSN: 0935-9648.

[120] N. Lindahl *et al.*, "Determination of the bending rigidity of graphene via electrostatic actuation of buckled membranes," *Nano Letters*, vol. 12, no. 7, pp. 3526–3531, 2012, ISSN: 1530-6984.

# Appendix A

# Supporting information for dissipation dilution paper

- S1: Fabrication of the device
- S2: MEMS stiffness characterization
- S3: Dissipation dilution model
- S4: Resonance frequency vs. voltage for devices D2 and D4

# Supporting Information

## Tuning dissipation dilution in 2D material resonators by MEMS-induced tension

Michiel P.F. Wopereis, Niels Bouman, Satadal Dutta, Peter G. Steeneken, Farbod Alijani, and Gerard J. Verbiest*

*Department of Precision and Microsystems Engineering, Delft University of Technology, Mekelweg 2, 2628 CD Delft, The Netherlands*

# S1. Fabrication of the device

We fabricate the devices in several steps. First, the MEMS are manufactured by the commercially available XMB10 process. This is followed by the transfer of the membranes on the MEMS using a custom-made PDMS stamp with PPC film. Then, the devices are mounted on a PCB carrier and wire-bonded. Additional short-circuit bonds are added on the edge of the PCB carrier to prevent electrostatic charging. The next step involves the removal of the PPC film from the chip using annealing. Finally, the membranes are clamped using EBID, and the short-circuit bonds are removed. This section describes each step in more detail.

## 1.1 Preperation

The membranes are strained in situ using MEMS devices. These devices are manufactured by the commercially available XMB10 process,[1,2] which involves Deep Reactive Ion Etching (DRIE) to create a bottom cavity wafer with a gap of 50 µm and a membrane wafer of 15 µm. These wafers are then fusion-bonded with a 0.6 µm $SiO_2$ in between the wafers to form the MEMS device (see Fig. 1).

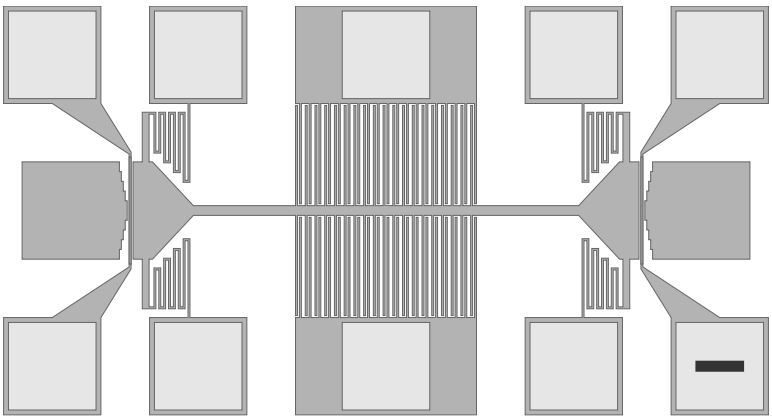

Figure 1: MEMS device layout. Scale bar: 50 µm

Next, we produce a PPC film by dissolving PPC pellets ($[CH(CH_3)CH_2OCO_2]_n$) in anisole ($C_7H_8O$) with a 15/85 ratio. This dissolution process is achieved using a magnetic stirrer at 50 degrees Celsius for 2 hours. Subsequently, microscope

cover slides are cleaned with isopropanol, and a droplet of the PPC solution is carefully placed at the center of each cover slide. To ensure even coating, a spin coater is used to uniformly spread a thin layer of the PPC solution over the entire surface of the cover slide (see Figures 2(a)-(d)). The slides are left to air-dry for seven days to complete the PPC film preparation, allowing complete evaporation of the anisole solvent. Finally, a custom dome-shaped PDMS stamp is produced for precise pick-and-place of the 2D material membranes. A mixture of 87% PDMS resin and 13% curing agent is mixed and dispensed as a droplet onto a microscope slide to make the stamp. The slide is then inverted and placed into a vacuum chamber for one hour to remove microscopic air bubbles. Afterward, the stamp is left to air-dry for 24 hours, forming a small dome on the surface. The final step is to cover the PDMS stamp with the PPC film, illustrated in Figure 2.

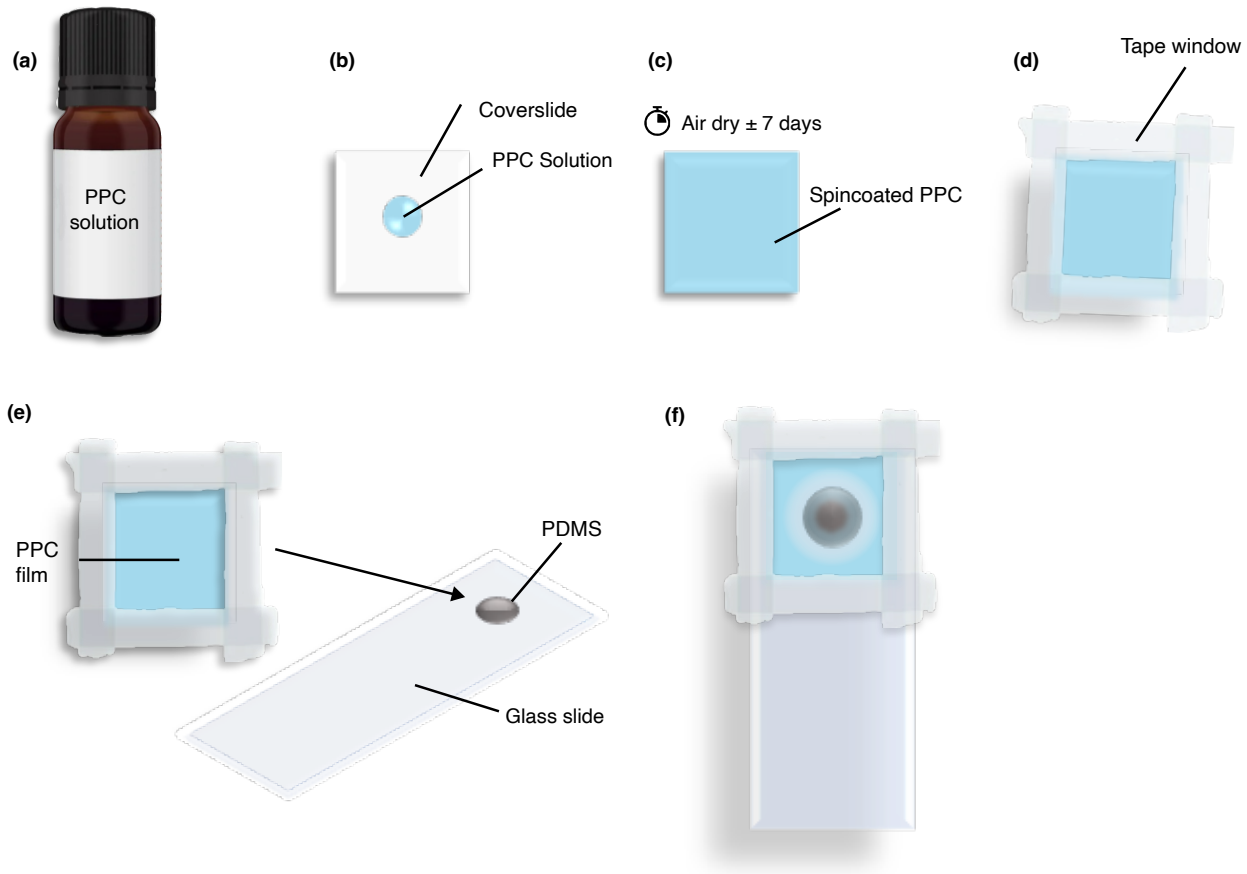


Figure 2: Preparation of the stamp for the transfer procedure. a) Solution of 15/85 mass ratio PPC granulate to anisole solvent b) Droplet of the PPC solution on a microscope cover slide c) Even distribution of the PPC solution over the cover slide after spin-coating d) Tape window attached to the PPC layer of the cover slide e) Transferring the PPC film to the dome-shaped stamp f) PDMS-dome shaped stamp covered with a PPC film ready for stamping.

## 1.2 Transfer of 2D Materials on MEMS

Transferring 2D materials onto the suspended shuttle of the MEMS poses significant challenges. Conventional transfer methods, including viscoelastic stamping techniques,[3] have proven unsuitable for this complex task. To address this limitation, we present a novel transfer method utilizing a sacrificial PPC layer, later removed through an annealing process. In our approach, rectangular-shaped flakes were selected through traditional exfoliation methods[4] and placed onto a rectangular square of polydimethylsiloxane $CH_3nSi(CH_3)_3$ (PDMS)

(see Figure 3). PDMS was chosen based on its transparency and adhesive properties.

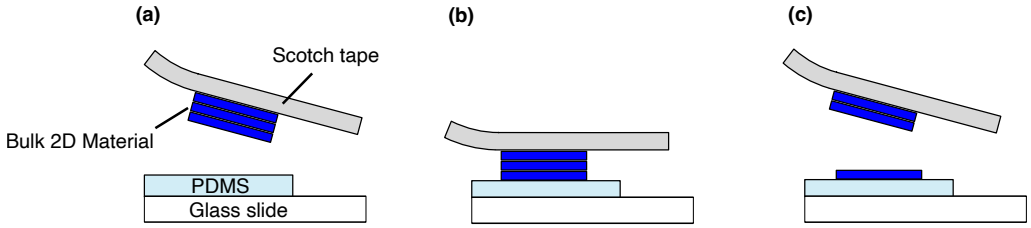


Figure 3: Schematic representation of the mechanical exfoliation of 2D materials on a PDMS substrate.

Next, we used a dome-shaped stamp, which was prepared in the first stage to transfer the membranes. This stamp was carefully positioned above the desired flake on the PDMS substrate (see Figure 5). By gently bringing the stamp with the PPC layer in contact with the 2D material, we exploited the higher adhesion of PPC in contrast with the PDMS substrate, which caused the flake to adhere to the stamp with the PPC layer (see Figure 5(b)-(c)). This approach is similar to the technique introduced by Kinoshita.[5]

Next, the dome-shaped stamp with the 2D material was carefully positioned above the desired location on the MEMS and brought into contact. The MEMS device was then heated to $105°C$, maintaining contact for approximately 5 minutes until the PPC layer started to melt (see Figures 5(d)-(e)). Afterward, the stamp was gradually removed, leaving the sacrificial PPC layer adhered to the MEMS device with the 2D material beneath it. The device was cooled to room temperature, completing the transfer procedure (see Figure 5f). An example of a die with MEMS after the membrane transfer can be found in Figure 4b.

The presented method offers several distinct advantages. Notably, it allows for precise pick and place of flakes within 350 $\mu m$ diameter, enabling accurate and controlled placement of multiple flakes onto a single chip (Figure 4b). Furthermore, the sacrificial PPC layer effectively accommodates transfer onto suspended and delicate MEMS components. Moreover, this transfer method is entirely dry, eliminating the need for wet chemistry commonly used with fragile parts.[6–8] This is especially beneficial for parts susceptible to surface tension forces, such as the comb drive.

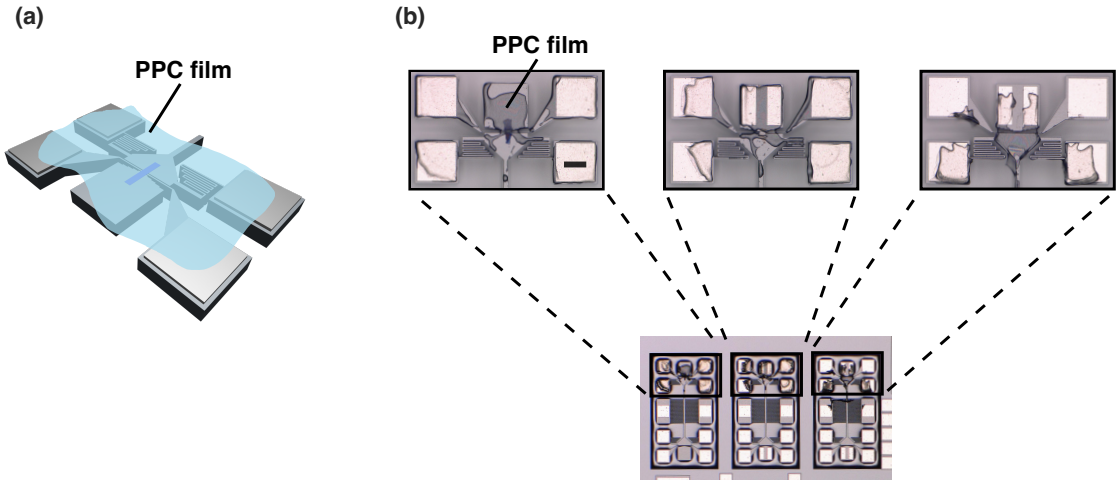


Figure 4: Device after transfer of 2D materials using a sacrificial PPC layer. a) Illustration of the device with the 2D material membrane beneath the PPC film b) Devices after transfer of three membranes onto a single die. Scale bar: 10 µm

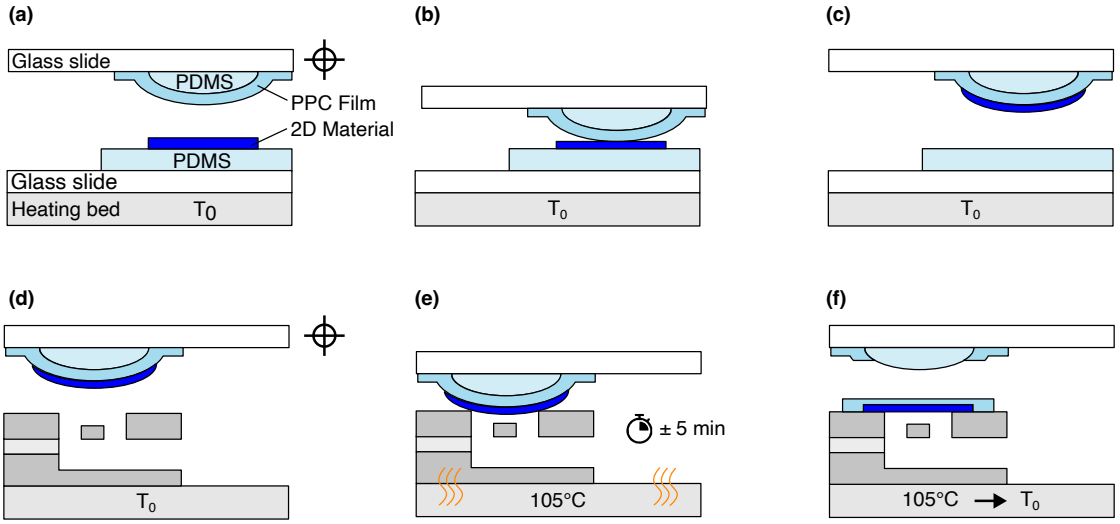


Figure 5: Procedure for transferring a 2D membrane to a substrate using a sacrificial PPC layer. a) Positioning the stamp above the membrane of interest b) Lower the stamp such that the membrane adheres to the PPC film of the stamp c) The membrane is removed from the PDMS d) Position the stamp above the cavity e) Making contact with the MEMS for about 5 minutes at 105°$C$ until the PPC layer starts to melt onto the MEMS f) Removing the stamp from the MEMS and cooling it down to room temperature.

## 1.3 Carrier Bonding Procedure

The silicon die containing the MEMS is secured onto a chip carrier using a combination of silver paste and a droplet of super glue applied on one side of the chip. This gluing ensures

a secure die attachment to the PCB carrier, essential for the wire bonding (see Figure 6c). Subsequently, wire bonding is performed to establish electrical connections between the MEMS and the carrier chip. A TPT HB05 wire bonder is used for this purpose, using a 25µm golden wire. For the initial ball bond, we select US, Time, and Force, 100, 200, and 10, respectively. For the second wedge bond, we select US, Time, and Force, 125, 200, and 15, respectively. Also, the stage is heated to 120 °C before bonding. During the bonding process, the PPC film plays a crucial role in effectively holding the 2D material in place, preventing the membrane from slipping (see Figure 6(a)-(b)). As a precautionary measure, both sides of the comb drive fingers are short-circuited to prevent charges from accumulating over the comb drive, which could cause unwanted movements during fabrication. The short connection is created with two extra wire bonds to the edge of the PCB carrier (see detail view in Figure 6c).

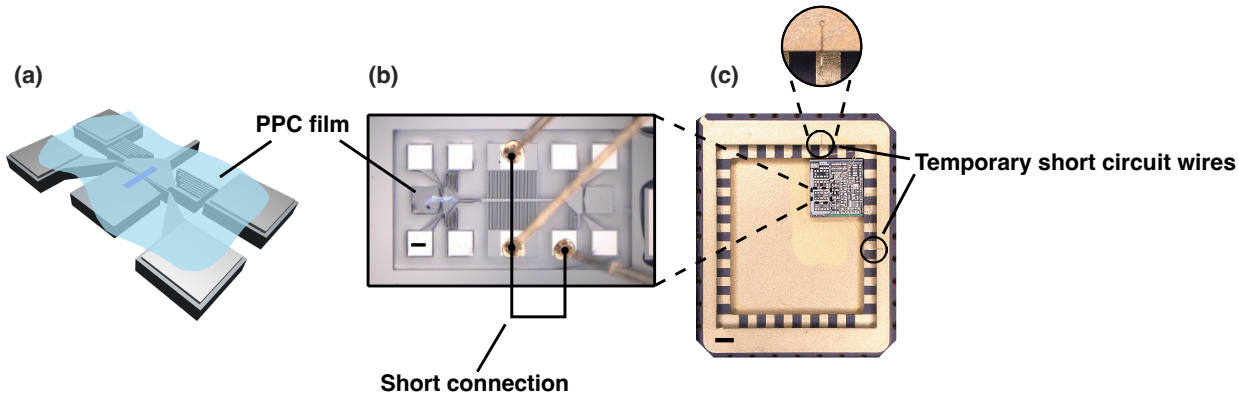


Figure 6: Device connected to a PCB carrier after wire bonding a) Illustration of the device with PPC film preventing the membrane from slippage during wire bonding b) Detailed view of wire-bonded MEMS. Scale bar: 50 µm c) Silicon die containing MEMS wire bonded on a PCB carrier, including a detailed view of the short connection wires. Scale bar: 1000 µm

## 1.4 Annealing

In the mechanical transfer step, the 2D material is placed onto the cavity of the MEMS using a sacrificial PPC film. The annealing step ensures that the PPC residue is removed from the MEMS. During annealing, the chip mounted on the PCB carrier is inserted into a

high vacuum oven operating at a pressure below $10^{-5}$ mbar. The annealing is conducted at 300°$C$ for 3 hours to ensure that all polymer contamination from the transfer is removed.[9,10] Notably, this annealing temperature exceeds the highest reported thermal decomposition temperature of PPC of 278°$C$,[11] effectively removing any residual PPC while being significantly below the thermal thresholds of other materials on the chip. To prevent unwanted reactions, the vacuum oven is thoroughly flushed with Argon before the annealing process. This creates an oxygen-free environment, preventing potential interaction between PPC and oxygen molecules during annealing.[12,13] Figures 7(a)-(c) show the removal of the PPC film after annealing.

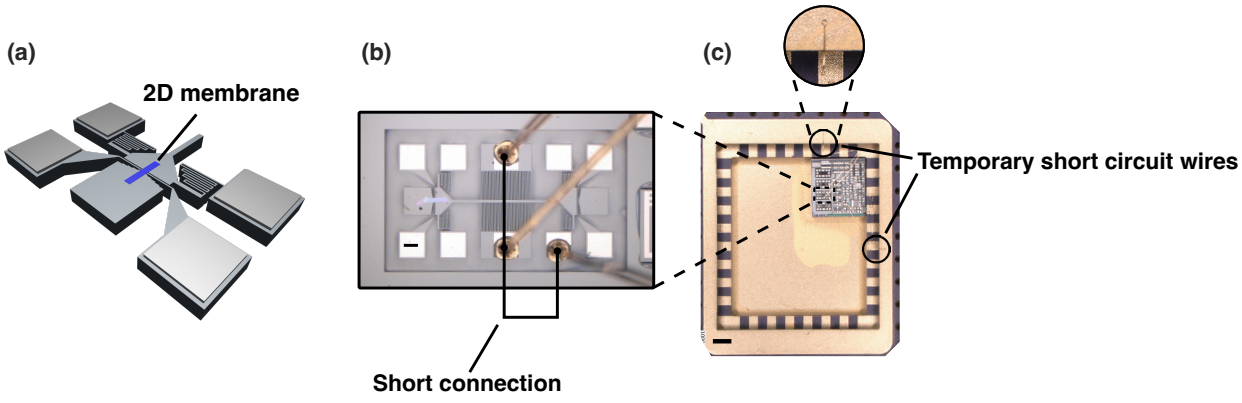


Figure 7: Device after the annealing process. a) Illustration of the device after annealing (the sacrificial PPC layer is evaporated) b) The wire-bonded MEMS after annealing. Scale bar: 10 µm c) The silicon die including the MEMS attached to the PCB carrier after annealing for 3 hours at 300°$C$. Scale bar: 1000 µm

## 1.5 Electron beam induced deposition (EBID)

To prevent slippage of the 2D material when subjected to tensile forces surpassing the Van der Waals adhesion forces during the experiment, a protective layer of approximately 130nm thick platinum is carefully deposited on both ends of the 2D material. This deposition is conducted through electron beam-induced deposition (EBID) to ensure precise control over the added layer. For this purpose, the FEI SEM Helios G4 CX system with a gas injection system (GIS) is used, operating at 10kV and 11nA. We deposited the platinum layer with an

offset from the suspended area to avoid contaminating the membranes during EBID. Refer to Figure 8 for an illustration. Applying this platinum protective layer provides a secure and reliable anchoring mechanism. The deposited platinum layer is a robust measure to firmly hold the 2D material, effectively preventing any undesirable slippage during the experiment. This essential precaution ensures the repeatability and accuracy of the experimental results, allowing for confident analysis of the 2D material under controlled conditions. In Figure 8b and Figures (c)-(d), the device is shown before and after EBID, respectively.

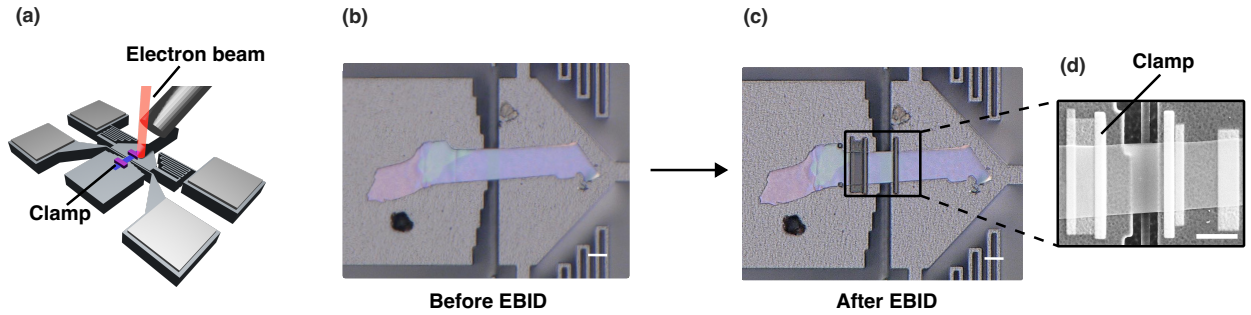


Figure 8: Electron beam induced deposition (EBID) procedure for clamping the membrane. a) Illustration of EBID b) Optical image of device D5 before EBID. Scale bar: 10 µm. c) Optical image of the device after EBID. Scale bar: 10 µm. d) SEM detailed view of the platinum clamps holding the membrane of device D5 in place. Scale bar: 10 µm.

## 1.6 Removing short circuit wires

Prior to testing, the short connection added to prevent charges from accumulating over the comb drive during electron beam exposure needs to be removed (Figures 7(b)-(c)). These additional bonds placed on the PCB carrier's edge are carefully removed under a microscope using a thin tungsten needle and tweezers.

# S2. MEMS stiffness characterization

### 2.1 Back-of-the-envelope calculation

To accurately determine the in-plane displacement of the shuttle, it is essential to know the system's stiffness. Four non-uniform serpentine flexures support the shuttle of the comb drive. The serpentine flexure has the following dimensions: one beam of $L_1 = 79\mu m$, one beam of $L_2 = 68\mu m$, two beams of $L_3 = 58\mu m$, two beams of $L_4 = 48\mu m$ and two beams of $L_5 = 38\mu m$ (see Figure 9b). Each beam has a width (w) of $2\mu m$ and a height (h) of $15\mu m$. The Young's modulus (E) of the silicon flexure is 169GPa.[14]

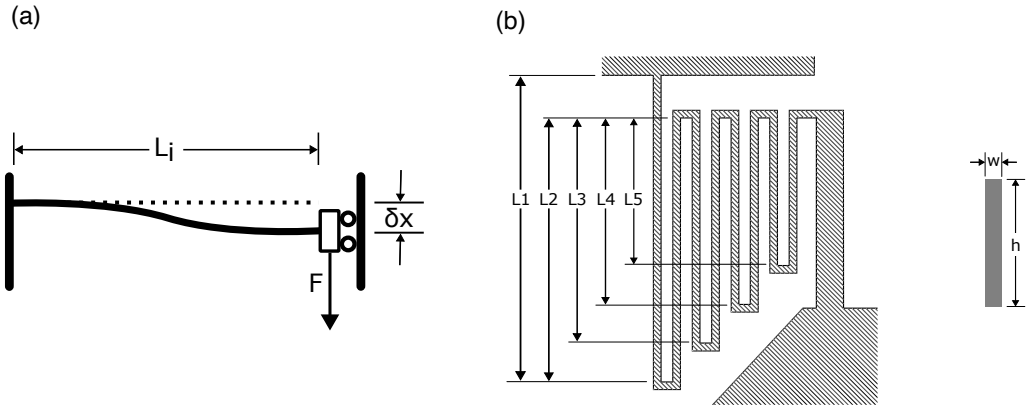


Figure 9: (a) Schematic representation of a single bent beam (b) Dimensions of non-uniform serpentine flexure

The stiffness of a single non-uniform serpentine flexure can be approximated by separating the flexure in a series of beams and calculating the stiffness of each beam individually, see Figure 9 and Equation 1.

$$\begin{aligned} \delta x_i &= \frac{F L_i^3}{12E \cdot I} \\ I &= \frac{hw^3}{12} \\ k_i &= \frac{F}{\delta x_i} \\ k_i &= Eh\frac{w^3}{L_i^3} \end{aligned} \tag{1}$$

Then, the stiffness of the flexure can be estimated by summating the individual beam stiffnesses as a series of springs ($k_1$ to $k_5$). This neglects the contribution of the connecting side

beams, which is assumed to be low. Following Equation 2, $k_s$ is calculated to be 13.3 N/m. Since the system consists of four flexures in parallel. The stiffness of the comb drive is four times the stiffness of a single flexure; thus, $k_{\text{cd}} = 53.1N/m$.

$$k_s \approx \left(\frac{2}{k_1} + \frac{2}{k_2} + \frac{2}{k_3} + \frac{1}{k_4} + \frac{1}{k_5}\right)^{-1}$$
$$k_{\text{cd}} = 4k_s \tag{2}$$

### 2.2 Computational study of comb drive stiffness

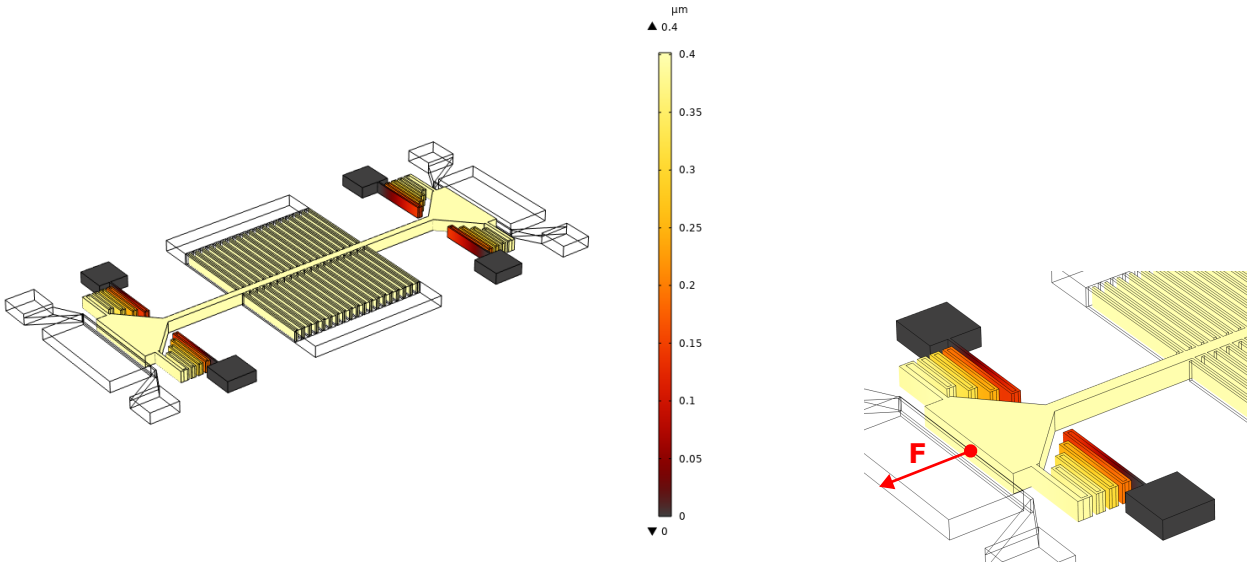


(a) (b)

Figure 10: Comsol Multiphysics study (a) Shuttle displacement with an applied load of $F = 20\mu N$ (b) Direction of the applied load on the shuttle

A computational study was conducted using COMSOL Multiphysics. Within this analysis, a force of 20 $\mu N$ (F) was exerted at the endpoint of the shuttle, directed along the axis of the narrowest gap of the comb drive, see Figure 10b. This force induced a displacement of 0.4 $\mu m$ ($\Delta x$) in the shuttle's position (see Figure 10a). By employing the relation $k_{\text{cd}} = F/\Delta x$, the inherent stiffness of the system can be determined, yielding $k_{\text{cd}} = 50N/m$. Notably, the determined stiffness value is marginally lower than the estimate from initial back-of-the-envelope calculations. This difference arises from including the whole flexure geometry in

the numerical simulation, including the interconnecting beams. This factor contributes to a minor reduction in the overall stiffness of the device.

### 2.3 Determining comb drive stiffness experimentally based on pull-in voltage

When voltage is applied over a capacitance, the electrostatic force will work to reduce the gap between opposing plates. At small voltages, the electrostatic force is counterbalanced with the spring force; however, when the voltages are increased, the plates will eventually pull in. Since this specific pull-in voltage is determined by the stiffness of the springs of the comb drive, it is an effective way to experimentally determine the stiffness of the comb drive based on the pull-in voltage for an empty device. The force acting on the movable shuttle can be derived by Equation 3.

$$F_{\text{sys}} = F_{cd} - k_{\text{cd}}x = \frac{A\epsilon_0}{2}\left(\frac{1}{(d_1 - x)^2} - \frac{1}{(d_2 + x)^2}\right)V^2 - k_{\text{cd}}x \tag{3}$$

When the system is in equilibrium, the electrostatic and spring forces cancel each other. The shuttle is stationary in this case and $F_{\text{sys}} = 0$. This leads to equation 4. This equation can be used to calculate the shuttle position x as a function of voltage. Above the pull-in voltage ($V_{PI}$), Equation 4 has no solutions. The pull-in point can be obtained by examining the stiffness of the system, which can be obtained by Equation 5.

$$\frac{A\epsilon_0}{2}\left(\frac{1}{(d_1 - x)^2} - \frac{1}{(d_2 + x)^2}\right)V^2 = k_{\text{cd}}x \tag{4}$$

$$\frac{\partial F_{\text{sys}}}{\partial x} = A\epsilon_0\left(\frac{1}{(d_1 - x)^3} - \frac{1}{(d_2 + x)^3}\right)V^2 - k_{\text{cd}} \tag{5}$$

When there is no voltage applied to the system, Equation 5 is $\frac{\partial F_{\text{sys}}}{\partial x} = -k_{\text{cd}}$; however, when V is increased, the stiffness will become less negative. At the pull-in point, $\frac{\partial F_{\text{sys}}}{\partial x} = 0$; hence, this point can be used to calculate the pull-in voltage for a certain stiffness $k_{\text{cd}}$. The stiffness around the equilibrium point can be obtained by first solving Equation 4 for $V^2$, and then

plugging in this solution into Equation 5. Eventually, when setting $\frac{\partial F_{\text{sys}}}{\partial x} = 0$, the equation can be solved for the shuttle displacement x, hereby obtaining the position where pull-in occurs $x = x_{\text{PI}}$:

$$x_{\text{PI}} = \frac{\alpha^2 + 3\,\alpha\,d_1 - 3\,\alpha\,d_2 + (d_1 - d_2)^2}{8\,\alpha} \tag{6}$$

with:

$$\alpha = \left(4\sqrt{\left({d_1}^2 - {d_2}^2\right)^2\left(5\,{d_1}^2 + 6\,d_1\,d_2 + 5\,{d_2}^2\right)} + 5\,d_1\,{d_2}^2 - 5\,{d_1}^2\,d_2 - 9\,{d_1}^3 + 9\,{d_2}^3\right)^{1/3}$$

Finally, knowing the unstable point $x_L$ purely based on the spacing of the comb fingers, one can determine either the pull-in point for a given $k_{\text{cd}}$ with Equation 7 or the stiffness of the comb drive with equation 8.

$$k_{\text{cd}} = \frac{A\epsilon_0}{2x}\left(\frac{1}{(d_1 - x_{\text{PI}})^2} - \frac{1}{(d_2 + x_{\text{PI}})^2}\right)V_{\text{PI}}^2 \tag{7}$$

$$V_{\text{PI}} = \sqrt{\frac{A\epsilon_0}{2xk_{\text{cd}}}\left(\frac{1}{(d_1 - x_{\text{PI}})^2} - \frac{1}{(d_2 + x_{\text{PI}})^2}\right)} \tag{8}$$

**Results** The pull-in test has been conducted for devices C8M1 and C8M4; both devices have a completely torn flake, so there is no stiffness contribution to the membrane. For the proceeding calculation of the devices that are not experimentally tested on stiffness, the average of devices C8M1 and C8M4 will be used (see Table 1), which is 38.42 N/m. The pull-in voltage is approximately 13.5 ± 0.5 V.

Table 1: Experimental stiffness characterization

| Device | Voltage | Stiffness |
|---|---|---|
| C8M1 | $13.89 \pm 0.04$ V | $41.07 \pm 0.23$ $\text{Nm}^{-1}$ |
| C8M4 | $12.96 \pm 0.06$ V | $35.76 \pm 0.33$ $\text{Nm}^{-1}$ |

# S3. Dissipation dilution model

Membranes can build up much potential energy when the vibrational deflection has to work against the high lateral tensile stress,[15] leading to dissipation dilution. The tensile stress of the membranes is incrementally increased using a comb drive actuator. By definition, the quality factor of a membrane subjected to tensile stress can be described by:[16,17]

$$Q = 2\pi \frac{W_{\text{tension}} + W_{\text{elongation}} + W_{\text{bending}}}{\Delta W_{\text{elongation}} + \Delta W_{\text{bending}}} \tag{9}$$

Where $W_{\text{tension}}$ is the stored elastic energy required to deflect the membrane against the tensile force, $W_{\text{elongation}}$ and $W_{\text{bending}}$ is the stored energy due to elongation and bending, respectively. Finally, $\Delta W_{\text{elongation}}$ and $\Delta W_{\text{bending}}$ are the lost energy due to elongation and bending. When the stored tensile energy dominates the mechanical behavior for highly stressed membranes, the elongation and bending energies become negligible ($W_{\text{tensile}} \gg W_{\text{elongation}} + W_{\text{bending}}$). Moreover, when assumed that the intrinsic damping is equal for both the elongation and bending, such that $Q_{\text{elongation}} = 2\pi \frac{W_{\text{clongation}}}{\Delta W_{\text{elongation}}} = Q_{\text{bending}} = 2\pi \frac{W_{\text{bending}}}{\Delta W_{\text{bending}}}$, we can derive the expression for a highly stressed membrane as $Q \approx \alpha_{\text{dd}} \cdot Q_{\text{intrinsic}}$, where $\alpha_{dd}$ is the dilution factor, namely:

$$\alpha_{dd} = \left[ \frac{W_{\text{bending}}}{W_{\text{tensile}}} + \frac{W_{\text{elongation}}}{W_{\text{tensile}}} \right]^{-1}. \tag{10}$$

When the membranes are strained, the stored tensile energy $W_{\text{tensile}}$ in the resonator increases while the energy stored in bending and elongation remains identical.[15] Therefore, the damping dilution factor becomes larger with increased strain. This increase in the stored tensile energy 'dilutes' the intrinsic losses $Q_{int}$, resulting in a higher $Q$.

For unstrained membranes, the resonance frequency depends on the thickness of the flake. For very thin membranes ($\approx$ 1 to 5 layers), the resonance frequency is dominated by the initial pre-tension in the membrane $f_{\text{mem}}$.[18] In contrast, relatively thick membranes ($>\approx$ 15 layers) follow the expected dynamics for plates $f_{\text{plate}}$, which depend mainly on the geometry

of the membranes.[18] In the cross-over regime, between pre-tension dominated and bending rigidity dominated, the fundamental resonance frequency of a membrane subjected to strain can be estimated by $f_0 = \sqrt{f_{\text{mem}}^2 + f_{\text{plate}}^2}$,[18,19] and the quality factor by due to dissipation dilution by:[20]

$$Q_D \approx \left( \frac{|f_{\text{mem}}|^2}{|f_{\text{plate}}|^2} + 1 \right) \frac{E_1}{E_2}, \tag{11}$$

Where $E_1$ and $E_2$ represent the dynamic modulus at a certain frequency by $E = E_1 + iE_2$,[15,17,21] with $E_1$ being the storage modulus and $E_2$ being the loss modulus. Assuming that $E_1$ and $E_2$ do not change much with frequency, we can approximate $E_1/E_2 \approx Q_{\text{int}}$. Since the membranes are relatively thick and dominated by the bending rigidity, and $f_{\text{plate}}$ does not change with strain, we can assume that $f_0$ equals $f_{\text{plate}}$ when the membranes are unstrained ($V_{\text{cd}} = 0\,V$). Therefore, $f_{\text{plate}} = f_0(0\text{ V})$. The dynamics can be described by $f_0 = \sqrt{f_{\text{mem}}^2 + f_{\text{plate}}^2}$. This simplifies Equation 11 to:

$$Q_D \approx \left( \frac{f_0}{f_{\text{plate}}} \right)^2 Q_{\text{int}} \tag{12}$$

It can be seen that when $f_0$ increases due to straining the membrane ($f_0 \propto V^2$), the increase in $f_0$ dilutes the intrisic dissipation losses and therefore enhances Q.

# S4. Device measurements

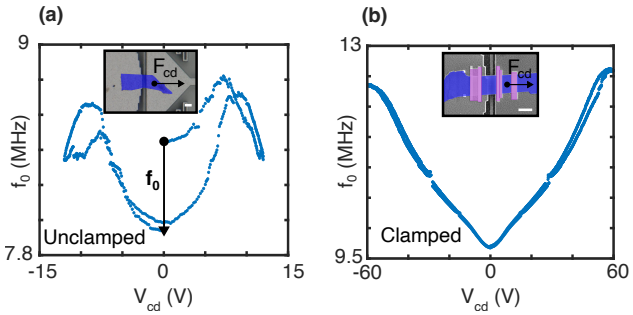


Figure 11: Comparison of the resonance frequency ($f_0$) versus the comb drive voltage ($V_{\mathrm{cd}}$). $F_{\mathrm{cd}}$ indicates the pulling direction of the suspended shuttle by the comb drive actuator. Scale bars: 10 micrometers. a) Unclamped device D2, $V_{\mathrm{max}}$ = 12 V, false-colored optical image (blue: 2D membrane) b) Device D4 clamped with a platinum layer using EBID,$V_{\mathrm{max}}$ = 60 V (blue), false-colored SEM image (blue: 2D membrane, pink: platinum clamps)

# References

(1) Zou, X.; Ahmed, S.; Jaber, N.; Fariborzi, H. A Compact High-Sensitivity Temperature Sensor using an Encapsulated Clamped-Clamped Mems Beam Resonator. 2021 21st International Conference on Solid-State Sensors, Actuators and Microsystems (Transducers).

(2) Streit, P.; Forke, R.; Voigt, S.; Schwarz, U.; Ziegenhardt, R.; Weidlich, S.; Billep, D.; Gaitzsch, M.; Kuhn, H. Vibration sensors with a high bandwidth and low SNR, enhanced with post processing gap reduction. 2022 23rd International Conference on Thermal, Mechanical and Multi-Physics Simulation and Experiments in Microelectronics and Microsystems (EuroSimE).

(3) Castellanos-Gomez, A.; Buscema, M.; Molenaar, R.; Singh, V.; Janssen, L.; Van Der Zant, H. S. J.; Steele, G. A. Deterministic transfer of two-dimensional materials by all-dry viscoelastic stamping. *2D Materials* **2014**, *1*, 011002.

(4) Novoselov, K. S.; Jiang, D.; Schedin, F.; Booth, T. J.; Khotkevich, V. V.; Moro-

zov, S. V.; Geim, A. K. Two-dimensional atomic crystals. *Proceedings of the National Academy of Sciences* **2005**, *102*, 10451–10453.

(5) Kinoshita, K.; Moriya, R.; Onodera, M.; Wakafuji, Y.; Masubuchi, S.; Watanabe, K.; Taniguchi, T.; Machida, T. Dry release transfer of graphene and few-layer h-BN by utilizing thermoplasticity of polypropylene carbonate. *npj 2D Materials and Applications* **2019**, *3*.

(6) Xie, Y.; Lee, J.; Wang, Y.; Feng, P. X. Nanoelectromechanical Systems: Straining and Tuning Atomic Layer Nanoelectromechanical Resonators via Comb-Drive MEMS Actuators (Adv. Mater. Technol. 2/2021). *Advanced Materials Technologies* **2021**, *6*, 2170008.

(7) Verbiest, G. J.; Goldsche, M.; Sonntag, J.; Khodkov, T.; von den Driesch, N.; Buca, D.; Stampfer, C. Tunable coupling of two mechanical resonators by a graphene membrane. *2D Materials* **2021**, *8*, 035039.

(8) Sonntag, J.; Goldsche, M.; Khodkov, T.; Verbiest, G.; Reichardt, S.; Den Driesch, N. V.; Buca, D.; Stampfer, C. Engineering Tunable Strain Fields in Suspended Graphene by Microelectromechanical Systems. 2019 20th International Conference on Solid-State Sensors, Actuators and Microsystems & Eurosensors XXXIII (TRANSDUCERS & EUROSENSORS XXXIII).

(9) Cartamil-Bueno, S. J.; Cavalieri, M.; Wang, R.; Houri, S.; Hofmann, S.; Van Der Zant, H. S. J. Mechanical characterization and cleaning of CVD single-layer h-BN resonators. *npj 2D Materials and Applications* **2017**, *1*.

(10) Dolleman, R. J.; Hsu, M.; Vollebregt, S.; Sader, J. E.; Van Der Zant, H. S. J.; Steeneken, P. G.; Ghatkesar, M. K. Mass measurement of graphene using quartz crystal microbalances. *Applied Physics Letters* **2019**, *115*, 053102.

(11) Luinstra, G. A.; Borchardt, E. *Synthetic Biodegradable Polymers*; Springer Berlin Heidelberg, 2011; pp 29–48.

(12) Kumar, K.; Kim, Y.-S.; Yang, E.-H. The influence of thermal annealing to remove polymeric residue on the electronic doping and morphological characteristics of graphene. *Carbon* **2013**, *65*, 35–45.

(13) Lin, Y.-C.; Lu, C.-C.; Yeh, C.-H.; Jin, C.; Suenaga, K.; Chiu, P.-W. Graphene Annealing: How Clean Can It Be? *Nano Letters* **2012**, *12*, 414–419.

(14) Hopcroft, M. A.; Nix, W. D.; Kenny, T. W. What is the Young's Modulus of Silicon? *Journal of Microelectromechanical Systems* **2010**, *19*, 229–238.

(15) Schmid, S. *Fundamentals of Nanomechanical Resonators*; 2016.

(16) Schmid, S.; Jensen, K. D.; Nielsen, K. H.; Boisen, A. Damping mechanisms in high-Q micro and nanomechanical string resonators. *Physical Review B* **2011**, *84*.

(17) Schmid, S.; Hierold, C. Damping mechanisms of single-clamped and prestressed double-clamped resonant polymer microbeams. *Journal of Applied Physics* **2008**, *104*.

(18) Castellanos-Gomez, A.; Singh, V.; van der Zant, H. S. J.; Steele, G. A. Mechanics of freely-suspended ultrathin layered materials. *Annalen der Physik* **2015**, *527*, 27–44.

(19) Castellanos-Gomez, A.; Van Leeuwen, R.; Buscema, M.; Van Der Zant, H. S. J.; Steele, G. A.; Venstra, W. J. Single-Layer MoS2 Mechanical Resonators. *Advanced Materials* **2013**, *25*, 6719–6723.

(20) Steeneken, P. G.; Dolleman, R. J.; Davidovikj, D.; Alijani, F.; van der Zant, H. S. J. Dynamics of 2D material membranes. *2D Materials* **2021**, *8*.

(21) Unterreithmeier, Q. P.; Faust, T.; Kotthaus, J. P. Damping of Nanomechanical Resonators. *Physical Review Letters* **2010**, *105*.

# Appendix B

# Electrostatic force exerted by the comb drive actuator

A MEMS actuator is used for straining the membranes. This actuator consists of a comb drive with asymmetrically spaced teeth; one set is movable, and the other is stationary. Due to the difference in spacing, the electrostatic forces work in opposite directions. The shuttle will ultimately move toward the smallest gap ($d_1$). The force induced by the comb drive can be approximated using parallel plate theory as follows:

$$F_{\text{cd}} = -\frac{\partial U}{\partial d} \tag{B.1}$$

$$U = \frac{1}{2}CV^2 = \frac{1}{2}\frac{A\epsilon_0}{d}V^2 \tag{B.2}$$

$$F_{\text{cd},1} = \frac{\partial U_1}{\partial d} = -\frac{\partial}{\partial\,(d_1 - x)}\frac{A\epsilon_0}{2\,(d_1 - x)}V^2 = \frac{A\epsilon_0}{2\,(d_1 - x)^2}V^2 \tag{B.3}$$

$$F_{\text{cd},2} = \frac{\partial U_2}{\partial d} = -\frac{\partial}{\partial\,(d_2 + x)}\frac{A\epsilon_0}{2\,(d_2 + x)}V^2 = \frac{A\epsilon_0}{2\,(d_2 + x)^2}V^2 \tag{B.4}$$

$$F_{\text{cd}}\,\hat{\boldsymbol{i}} = F_{\text{cd},1} - F_{\text{cd},2}\,\hat{\boldsymbol{i}} = \frac{A\epsilon_0}{2}\left(\frac{1}{(d_1 - x)^2} - \frac{1}{(d_2 + x)^2}\right)V^2\,\hat{\boldsymbol{i}} \tag{B.5}$$

Where $A$ is the overlapping area between the comb drive fingers ($A$=1.5×10$^{-9}$m$^2$), $\epsilon_0$ is the vacuum permittivity ($\epsilon_0 = 8.854\times10^{-12}Fm^{-1}$), $d_1$ is the distance of the smallest gap ($d_1$ = 2 µm), $d_2$ is the distance of the biggest gap ($d_1$ = 4 µm) and $x$ is the absolute movement in the direction of the smallest gap. Equation (B.5) can be used to calculate the force exerted by the comb drive. It can be noticed that the force between $d_1$ ($F_{\text{cd},1}$) gets greater when the shuttle moves, in contrast to the force between $d_2$ ($F_{\text{cd},2}$) that gets smaller.

# Appendix C

# Critical pre-deformation for buckled membranes

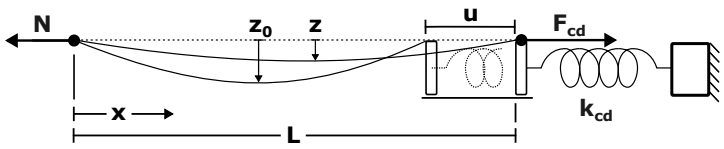


**Figure C.1:** Schematic illustration of the buckling model

In Fig. 3.2(d), an initial decrease in $f_0$ was observed with applied comb drive force. This can only hold if $\partial k_{\text{eff}}/\partial N < 0$. This expression can be evaluated by substituting $u$ from Eq. (3.9) and $z$ from Eq. (3.8). Such that:

$$k_{\text{eff}} = 2EI\frac{\pi^4}{L^3} + EA\epsilon_0\frac{\pi^2}{2L} + EA\left(\frac{\pi z_0}{2}\right)^2\frac{\pi^2}{2L^3} + N\frac{\pi^2}{2L} + 7\frac{\pi^4 EAz_0^2}{16L^3}\left(\frac{1}{1+N/N_b}\right)^2, \tag{C.1}$$

Now taking the derivative $\partial k_{\text{eff}}/\partial N$, leads to:

$$\frac{\partial k_{\text{eff}}}{\partial N} = \frac{\pi^2}{2L} - \frac{14\pi^4 EAz_0^2}{16N_bL^3(1+N/N_b)^3}, \tag{C.2}$$

The expression becomes negative if $N$ is 0 and $z_0$ is above a critical value ($z > z_c$). The critical value is calculated by setting $\partial k_{\text{eff}}/\partial N = 0$. The determined critical value is:

$$z_c = \sqrt{\frac{4N_bL^2}{7\pi^2 EA}}, \tag{C.3}$$

Knowing that $N_b = 4\pi^2 EI/L^2$, $I = Wt^3/12$ and $A = Wt$ Eq. (C.3) can be simplified to:

$$z_c = \sqrt{4/21}t \tag{C.4}$$

To conclude, in case $z_0 > \sqrt{4/21}t$, an initial decrease in $f_0$ is expected. For completeness, a schematic representation of the model can be seen in Figure C.1.